# Microwave Near-Field Imaging and Material Characterization

by

Seyed Hossein Mirjahanmardi

A thesis
presented to the University of Waterloo
in fulfillment of the
thesis requirement for the degree of
Doctor of Philosophy
in
Electrical and Computer Engineering

Waterloo, Ontario, Canada, 2020

**Examining Committee Membership**

The following served on the Examining Committee for this thesis. The decision of the Examining Committee is by majority vote.

| | |
|---|---|
| External Examiner: | Thomas Vaughan<br>Professor, Columbia University |
| Supervisor(s): | Omar M. Ramahi<br>Professor, University of Waterloo |
| Internal Member: | Zhou Wang<br>Professor, University of Waterloo |
| Internal Member: | Raafat Mansour<br>Professor, University of Waterloo |
| Internal-External Member: | Hamidreza Tizhoosh<br>Professor, University of Waterloo |

I hereby declare that I am the sole author of this thesis. This is a true copy of the thesis, including any required final revisions, as accepted by my examiners.

I understand that my thesis may be made electronically available to the public.

**Abstract**

In recent years, microwave imaging has attracted many researchers from various fields such as medical imaging, remote sensing, and industrial ones because of its high degree of penetration, non-ionizing and safe nature, and the low-cost of devices needed to generate images at low frequencies. This modality has great potential for producing unique and informative images because the response of materials, including human tissues, to electromagnetic excitation differs as the material's electrical characteristics change. Although microwave imaging has potentially distinctive features as an imaging modality, main challenges still exist. The penetration level of waves and their operation frequency have an inverse relation, meaning that to sufficiently penetrate the objects and identify small changes, such as anomalies in human bodies or an object, low-frequency waves are needed as excitation. However, decreasing the frequency degrades image resolution, a barrier in microwave imaging research. Other challenges are the need for simulations models, high computational resources, and significant processing time to retrieve the image of the object under test (OUT) beyond the diffraction limit.

The high-resolution imaging algorithms reported in the literature are based on simulation-measurement combination. These algorithms are iterative and optimization-based, meaning that to reach an acceptable answer, numerous simulations need to be run. In addition, such iterative algorithms depend strongly on proper initialization to converge, which requires prior information that is not available unless MRI or CT images are taken and fed to these algorithms. This single initialization may not be enough if the OUT changes over time. For example, in the case of medical use, if a cancer treatment such as chemotherapy is ongoing, the tissues and therefore the OUT structure may change. In such cases, the first initialization no longer valid, resulting in the need for new MRI or CT images to be taken. But the need for such processes to create a microwave image, if medical use is concerned, violates the main goal of this modality: mass screening for early cancer detection.

The other challenge of a microwave image is its resolution, which strongly depends on the operation wavelength and in most cases is much larger than the desired anomaly to be imaged. Having a large wavelength increases the diffraction phenomenon that occurs in the OUT while waves propagate. Thus, the wave energy packet spreads through the

medium. The inverse algorithms reported in the literature, that take the diffraction phenomenon into account, are inherently ill-posed, meaning that a unique solution cannot be obtained unless some prior information is used. These algorithms are simulation-oriented, and consequently, are time-consuming, model-based, and do not produce reliable answers.

The noticeable advantages of generating images at low frequencies have convinced us that microwave imaging modality has a strong role to play, potentially in medical applications. To address the aforementioned challenges regarding the microwave imaging approaches reported in the literature, this research work proposes to use narrowband electrically small antennas in the near field along with the Radon transform and filter-back projection as the reconstruction algorithm. Designing proper electrically small antennas significantly reduces the diffraction occurring in objects under test. Therefore, waves no longer spread in the OUT, only minimum coupling occurs between its layers, and the waves instead propagate in straight lines. This ray-like behavior of waves allows us to apply one of the most powerful reconstruction algorithms used widely in clinical imaging, the filtered-back projection algorithm, based on Radon transform. This algorithm, which is the basis of computerized tomography, needs no simulation or initialization. Thus, no optimization is used; the result is reliable images. In addition, the probes designed for the tested prototypes operate at low frequencies, which results in high penetration, and the waves excite the internal parts of the OUT.

Major distinguishing features of the proposed system are the low-cost devices needed to generate images from the OUT, its safety, and the high penetration of waves capable of sensing in-depth anomalies. In addition, the reliable reconstruction algorithm that has been developed in this research work makes the proposed microwave imaging system unique. Unlike other high resolution microwave imaging algorithms developed, the algorithm proposed in this work is computationally low-cost and needs no prior knowledge or simulations. The preliminary images generated using the suggested system promise a future for microwave imaging modality. This system can potentially open new windows in the area of microwave imaging and improve medical imaging algorithms for mass and frequent screening.

**Acknowledgments**

All praises are due to Allah for giving me the ability to accomplish this dissertation, to remind me not to disappoint, to rely on him, to be patient, and to move forward. This research could not be done without his continuous providence.

I would like to have a special thank to my supervisor, Professor Omar M. Ramahi, for his supervision during this work and for his freedom in thinking attitude which always encouraged me to think differently and for all of his supports. It was him who encouraged me to take risks, to explore new research territories, and to question fundamental theories.

I am also grateful to my committee members, Professor Zhou Wang, Professor Raafat R. Mansour, Professor Hamidreza Tizhoosh, and Professor Thomas Vaughan for serving in my examination committee and for their valuable comments and feedback. I would like to have a special thank to Professor Tizhoosh for the very helpful discussion we had on medical imaging modalities.

An special thank goes to Professor Vaughan for his valuable comments and encouragements. I learned from him how much a scientist can be knowledgeable yet humble, respectful, and responsible to the world.

I greatly appreciate my colleagues during my Ph.D. studies at the University of Waterloo. Specifically, I would like to thank Ali Albishi, Melad Olaimat, Mohamed El Badawe, Faruk Erkman, Miguel Ruphuy, Dawood Alsaedi, and Vahid Nayyeri for the valuable discussions we had. My apologies to those whom I forgot to mention here. I would like to also thank Dr. Behrooz Semnani for his valuable comments. I am also thankful to the University of Waterloo for its valuable support, especially the writing center department and Mary Mchpherson.

I owe my deepest gratitude to my family for their support, patience, and for believing in me, my father, my mother, and my sister. I could not accomplish this stage, and all previous stages, if my father's continuous encouragements and my mother's efforts on familiarizing me with the science world at my childhood were not there.

My endless gratitude to my wife for her continuous patience, for her inspirations, and for the valuable technical discussions we had. Words are incapable of properly describing

how much I owe her for her supports.

Last but not least, I express my deepest appreciation to the University of Waterloo Quran's community for their very valuable support and help from the very beginning of my Ph.D. to the very end.

This research work was financially supported by the Natural Sciences and Engineering Research Council.

## Dedication

To my father, mother, and sister for their unconditional love and support,
To my beloved wife and my daughter

# Table of Contents

# List of Tables

# List of Figures

# Chapter 1

# Introduction

## 1.1 Research Motivation

Creating images of interior parts of objects under test plays an important role in a wide variety of fields such as civil engineering and remote sensing, material characterization, security scanning, and medical applications [1–3]. Microwave imaging is currently widely available for civil engineering [4], security scanning [1], medical imaging, and material characterization [5]. However, lack of a reliable high resolution and non-simulation based microwave imaging approach is not yet sufficiently developed, especially in medical applications [3, 6–8]. Thus, further development, especially in the area of image reconstruction algorithms, is still required to prepare microwave imaging for medical applications.

Early stage imaging in medical applications plays an important role in a persons chance of survival. The current modalities available in the market cannot be easily used for early cancer detection, which requires images at the first stages of a cancer development. Magnetic resonance imaging, (MRI), although it provides high-resolution images, is very expensive. X-ray mammography and computerized tomography (CT) are the most-used modalities for cancer detection; however, they jeopardize patient health as they are based on ionizing radiation. Ultrasound is among the safest imaging modalities as it uses low frequency waves. However, it suffers from lack of high spatial resolution. In addition,

ultrasound reliability significantly depends on operator expertise [6]. Therefore, these modalities are not suitable for frequent or mass screening.

CT scans and X-ray mammography rely on the absorption and transmission of X-rays through the OUT. Photons emitted by X-rays have enough energy to easily excite the electrons of atoms, thus ionizing them [9, 10]. In addition, X-ray radiation cannot easily distinguish between soft tissues. Reports show that CT and X-rays are not reliable when imaging soft tissues is concerned because of their high rates of false negatives (4-34%) and false positives (70%) [6, 7, 11]. MRI provides images with very high spatial resolution and is inherently non-ionizing. However, its strong sensitivity to internal body movements such as heart beat rate may result in false images. Reports show that MRI generates moderate amounts of false positives also has a long acquisition time. On top of these all, the high cost of MRI prevents the use of this modality as a frequent screening tool [9,11,12]. Optical coherence tomography is a safe imaging modality. However, since the frequency range falls in the optical band, the penetration is limited to the surface of OUTs. Therefore, deep screening is not possible and this modality is limited to skin screening [13].

An additional downside to the aforementioned imaging modalities is that they cannot be mobile. In contrast, medical microwave imaging has proven its remarkable advantages over other medical imaging modalities in the past decade [14–20]. Its non-ionizing, low-cost, and non-invasive nature, as well as its ease of use are among the advantages that can make frequent screening possible, especially in the early stages of cancer wherein a true diagnosis plays a key role in patient survival. Microwave systems radiate electromagnetic waves at safe low frequencies, and rely on the permittivity differences between the interior parts of an object under test (OUT). Studies have proved that a significance contrast, 1:10, exists between the permittivity of tumorous and that of healthy tissues [6].

## 1.2 Background and Previous Works

### 1.2.1 Microwave Imaging

Microwave imaging relies on the electrical properties contrast, such as permittivity, between different materials. Various microwave imaging techniques [2], using qualitative or quantitative approaches, attempted to distinguish between the permittivity values and/or locate an anomaly in an OUT. Microwave imaging for medical diagnosis has been under investigation for years; but has remained in research phase [3]. Quantitative methods such as microwave tomography aim at completely reconstructing an object's details, meaning that permittivity and conductivity maps are generated [2, 11, 18, 20]. Microwave tomography methods fall into two categories: approximation-based and non-approximation-based. Approximation-based methods basically rely on the low/medium amount of contrast between the permittivity properties of the OUT, because they are based on Born and Rytov approximations. Additionally, since they are inverse-scattering methods, they are inherently ill-posed, especially for practical cases [26]. The non-approximation methods depend strongly on simulation models and computation, and thus require exhaustive amounts of computational resources, and lead to other numerical challenges that have been discussed already. These methods offer higher resolution, more than the diffraction limit, in which simulation plays a significant role, particularly in solving forward scattering models. Forward problems are iteratively solved and the model updated to converge to the results obtained from measurements. Optimization algorithms are used to increase the chance of result convergency, to obtain the best possible image, a global answer. The OUT is typically immersed in a coupling medium with properties similar to those of the OUT to eliminate the strong scattering from the OUT-air boundary [18, 27].

Uniqueness, stability, and convergence are the main issues that need to be considered while utilizing these model-based approaches. Since these methods are inverse-scattering based, lack of enough measurement data poses serious ill-conditioning, which may result in non-unique images. One of the main challenges these methods face is to reconstruct objects with a high permittivity contrast [28, 29], in part because large phase variation may occur in such cases as the waves will have different velocities affected by permittivity

values, creating phase-wrapping challenges. A few techniques are reported to solve this challenge [28, 30].

Time domain techniques, such as radar-based ones, are considered to be qualitative approaches [31–33]. These methods count on the time delay as well as the intensity between a transmitted signal and a reflected one. Because of the contrast level between tumors and healthy tissues, reflected and transmitted signals can be processed to image the body. Confocal microwave imaging (CMI) is a time-domain [34] technique that aims at detecting and localizing tumor locations. This essentially backscatter technique, falls into the radar-based approaches category. CMI shows a robust and rapid reconstruction procedure, which fewer computation resources are required than microwave tomography does. Multiple antennas transmit and receive signals to and from the OUT, assuming that some prior information exists about the object under test. Various types of antennas, including bowtie ones [34], scan the OUT in a cylindrical or planar path. The signals received from the medium are then processed to locate any anomaly in the OUT. The signal processing approach in CMI removes the initial content in the acquired signal because it contains the strong reflection from the boarder of the OUT, focusing mainly on the later content received. If the whole system is immersed in an oily medium, the reflection from air-skin is reduced. Calibration plays an important role in all time-domain techniques, including CMI, because any miscalibration results in either masking out the tumor or false negative/false positive predictions. One of the challenges that CMI has is the permittivity constant assumption over a wide frequency band. If the medium under investigation is dispersive, the propagation speed cannot be predicted accurately, making image reconstruction challenging. Another challenge that microwave imaging faces is the heterogeneous nature of some objects, as it makes propagation velocity prediction very rough if not correct. Time reversal methods can be used to process the data and generate images using the aforementioned techniques [33].

The scanning procedure in microwave imaging can be accomplished using one or multiple transmitter(s)/receiver(s) that scan the entire medium or multiple antennas. The former is time-consuming, and the scanning may take hours to achieve a desired resolution. The latter requires many antennas to be placed around the object under test [35]. This approach reduces the time of scanning significantly, however, the coupling between anten-

nas would be a major challenge to consider. Recently, the use of Multi Input Multi Output (MIMO) antennas has been introduced for microwave imaging purposes [36]. MIMO can reduce the number of antennas needed significantly because the scanning system can transmit and receive information by the same set of antennas simultaneously. The MIMO array can also contain asymmetrical transmitters and receivers [36].

Holographic approaches use the amplitude and phase of reflected and transmitted signals [37, 38]. Using a reference plane and assuming that no OUT exists, it compares the transmitted/reflected results between cases with and without an OUT. The reported systems based on holography can be narrowband or wideband. Wide band approaches depend on the information obtained within a wideband, assuming that no dispersion occurs in the model which has the challenges mentioned earlier. Holographic approaches use Fourier optics-based reconstruction techniques to break down the acquired scattered signals into the plane wave harmonics in the frequency domain. The information then becomes interpolated and inversed back to the spatial domain to create an image of the OUT [39–41]. These methods stem from synthetic aperture radar (SAR), representing a fully-focused method, and have the spatial resolution that is defined as follows [39]:

$$\delta_x = \frac{\lambda_c}{4sin(\theta_b/2)} \tag{1.1}$$

where $\lambda_c$ is the wavelength at the center frequency and $\theta_b$ is the beam-width of the antenna.

The microwave microscopy, being developed in our group [42,43], is among the highest-resolution methods, $\lambda/50$ to $\lambda/100$, as it operates in the near field zone. This method generally aims at high-quality sensing of OUTs and provides only an impression from the object; therefore, does not tend to provide an image reconstruction algorithm. The microwave microscopy operates in a very narrowband frequency range that avoids dispersion. In addition, it prevents scattering, thus reducing high-computational cost. In addition, no prior information is required for imaging the OUTs.

Microwave imaging has recently incorporated other modality information such as MR and CT to increase the resolution of images by refining the OUT structural information [44]. In such microwave imaging methods, the forward scattering equations are solved numerically, making an initial estimation of the OUT, to calculate the total field. The

results are then compared with the measured data and continuously updated to decrease the difference between simulation results and measurements ones (Gauss-Newton iteration algorithms). Different regulation techniques such as the Tikhonov one are used to simplify and solve the scattering equations [45]. Therefore, having an appropriate guess of the OUT is critical in such methods. Additionally, the accuracy of such methods strongly relies on the precision of simulations, which have their own limitations especially for electrically small objects. To solve this problem the amount of numerical cells used to compute the fields should be increased significantly, which requires weeks of simulations with current computers.

One of the main challenges in microwave imaging is the effects of surface wave multipath signals in near-field microwave imaging, meaning that unwanted signals from feed lines, both transmitter and receiver affect the results and reconstruction algorithm negatively [46]. In such cases since the signals have the same frequency, filtering does not solve the problem and time-gating methods only work if the source of these multipath signals and their directions are clear, which may not be the case in practical medical imaging [46]. The reason is that dielectric properties affect the propagation velocity, receiving signals from wanted and unwanted paths at the same time, so distinguishing between them is very difficult.

Another barrier that exists in microwave imaging is the absence of a reliable reconstruction algorithm, such as classical projection tomography, which is the basis of computerized tomography imaging. A few attempts are done to apply this algorithm to microwave domain but has not been implemented practically [47] except in [29]. In the latter report the reconstruction algorithm is only capable of restoring objects with low-contrast permittivity values using time domain techniques.

In summary, a thorough review of the microwave medical imaging systems reported in the literature reveals that:

• The diffraction limit can be overcome if simulation models are used along with measurements. Simulation models are iteratively updated to converge to an image, giving final image.

• The imaging algorithms rely on prior information, either coming from an MRI or CT,

to provide high resolution images.

According to the literature the key challenges in developing microwave imaging systems, specifically for medical applications, are as follows:

• Simulation software is needed for creating images. This software models the OUT and acts as a forward solution, but the resulting model can not be completely accurate because it depends on an approximate OUT model. The model is iteratively updated, by comparing the data obtained from measurements, to generate the final image. Since OUTs might be heterogeneous, generating images needs significant computational resources. But even if the resources are provided, the time to reach a converged solution is very high. On top of these drawbacks, simulations do not lead to strong-fidelity. The answers obtained from simulations are questionable, especially in the case of electrically small simulations, when tumors are very small compared to the frequency of operation and extremely dense meshing is required. However, having such a dense meshing significantly increases simulation time. Thus, mass screening is nearly impossible in these cases.

• Simulations depend on optimization algorithms which have a high chance of falling into local minimums, as they are the best for cases in which a local minimum is desired. However, in medical imaging, for which a global answer with a high correctness rate is required, optimization algorithms are not reliable.

• Many algorithms reported in the literature require prior knowledge to create correct and reliable images. Such prior knowledge means that an MRI or a CT image needs to be taken in advance, undercutting the fundamental goal of microwave imaging, which is frequent and easy screening.

• Time domain algorithms operate on a wide range of frequencies, such as ultra wide band radar techniques. However, most OUTs are highly dispersive, so permittivity changes over the bandwidth. The time domain algorithms' non-dispersive assumption thus poses a serious challenge and final images generated are not reliable.

• The frequency-based algorithms reported to date, attempt to take multiple scattering and diffraction into account, i.e., diffraction tomography. However, the number of antennas that can be placed in the imaging system to collect data is limited, creating an ill-posed problem since not enough information is collected. In addition, no analytical solution is

available for such a complex medium, which takes all the antennas and their coupling into account. Therefore, as mentioned, simulations are necessary in solving such problems, yet results in unreliable images.

Deeply encouraged by the non-invasive nature of microwave-based imaging, and cognizant of the challenges of these previously reported imaging systems, this project introduces a novel imaging modality that has never been introduced before [48]. The proposed system has the advantages of microwave imaging, while providing a high-resolution fast imaging system. The proposed system eliminates the effect of multiple scattering, removing the need for simulation models, and more importantly, for prior knowledge. The proposed approach relies on near-field (evanescent) interaction with the object under test, which enhances the resolution. The ideas presented in this project provides a low-cost non-ionizing imaging technology.

### 1.2.2 Material Characterization

The second part of the thesis focuses on material characterization. The response of dielectric materials to electromagnetic waves depends on their complex dielectric constants. Electromagnetic material properties find applications in a wide range of technologies, including biomedical, remote sensing, agriculture, food quality, material quality control and printed circuit board ones [5, 49–56]. Several methods have been used to measure the complex permittivity of materials and can be divided into transmission-based techniques such as the free-space, and reflection-only-based techniques such as the open-ended coaxial and resonant cavity perturbation methods [5].

Transmission line methods are widely used for dielectric permittivity determination and include the waveguide method [57–61] and the coaxial cable techniques [62, 63]. In the waveguide approach, a sample is machined to fit inside the waveguide structure. As a result, air gaps can be produced inside the structure that can affect the overall accuracy of measurements [64]. The waveguide technique presents other challenges such as limiting the operation frequency range since higher-order modes can contain longitudinal field components that generate resonance peaks [64]. Unlike the waveguide approach, the coaxial cable approaches have wider operating frequency range. However, compared to the waveguide

approach, the sample preparation can be challenging since a smaller dielectric sample is typically needed, requiring high fabrication tolerance.

The free-space technique is nondestructive and covers a wide range of operating frequencies with relatively simple sample preparation [65–71]. The free-space method is contactless; however, a large sample is needed to minimize edge diffraction. Consequently, lenses may be required to focus the wave at the center of the dielectric slab, necessitating expensive technologies. The free-space technique uses the phase of the scattering parameters, posing the challenge of phase wrapping, and possibly yielding multiple solutions [64,65]. To overcome this challenge, several solutions have been proposed, such as the use of iterative solvers [72], extra measurements [65], and the Kramers-Kronig relationship [68]. Each of these proposed solutions, however, makes the process more complex and time-consuming.

Among the reflection-based techniques, the open-ended coaxial method is the most popular [73–75]. This method works for a wide range of frequency with easy sample preparation. However, the results may not be accurate enough for all applications because it relies on an approximate model of the field distributions at the open end of the coaxial line. [5, 25, 74, 75]. In addition, the method assumes that the material under test is semi-infinite, which typically requires a large sample. Moreover, the need for phase information and precise calibration makes this method expensive [76].

The resonant cavity perturbation techniques provide high accuracy because they are resonance-based and provide high-quality factor [64, 77–79]. Achieving this high quality factor requires that the frequency bandwidth be very narrow; therefore, the dielectric properties can be extracted for frequencies only in the vicinity of the resonant frequency [64]. This method's accuracy drops with high-loss materials since the resonance peak broadens as material loss increases.

The need for phase information in retrieving unique permittivity values plays a pivotal role in the techniques mentioned above. Removing the phase, yet maintaining high accuracy, has been a challenge. To the best of our knowledge, only a few amplitude-only methods are available [80–83]. However, the level of accuracy and the uniqueness of the solution depend on material loss, operation frequency, and the length of samples (and thus a sufficient power loss must occur in the sample). This power loss requirement itself poses

a need for prior information about the material under test [80, 83, 84]. The bandwidth used in [81] is relatively large, making the characterization of lossy materials challenging. Some of these methods remove the need for phase information; however, they require a vector network analyzer to measure reflections from the material [81, 83, 85]. Therefore, a characterization method that requires only the amplitude of the transmitted signal while providing high accuracy is still needed.

The second part of this thesis introduces a technique that requires only measurements of the transmitted real power. The method presented here does not require phase information, significantly reducing in the cost of the measurement setup, yet providing a high accuracy and a simple setup for liquid measurements. In addition, only transmission information is used. Practically, this approach implies using power meters or spectrum analyzers rather than vector network analyzers. The method is validated numerically and experimentally for testing low, medium, and high loss materials without the need for prior information.

## 1.3 Research Objectives

Microwave medical imaging, despite its distinct advantages over other modalities, has not yet found a path to medical clinics. As discussed, the main reason is the absence of a reliable image reconstruction procedure which provides high resolution, yet does not rely on simulations nor prior information. This thesis offers a new imaging system based on the microwave regime to solve the challenges existing in current imaging systems: reliable image reconstruction method, high resolution, no simulation-in-use. The system can be potentially used for short-range imaging such as medical imaging.

This research also introduces a new material characterization method that makes the complex permittivity measurement less expensive than those methods reported in the literature, without the need for a vector network analyzer and phase measurements. The accuracy of introduced method is very high, validated by multiple theoretical and practical cases ranging from low-loss to high-loss materials.

Therefore, the main objectives in this thesis are summarized as follows:

1. **Introduce** a novel concept to eliminate the diffraction phenomena and multiple scattering that occurs in objects under test, realizing ray-like behavior at low frequencies.

2. **Propose** an image reconstruction algorithm based on Radon transform and filtered back projections compatible with the designed antennas at microwave range. The introduced full imaging system has a high resolution that can create near field images without the need for simulations and optimizations, which decrease imaging time significantly at low-computational cost.

3. **Offer** a novel approach to measure the permittivity of materials accurately without the need for phase information, decreasing the measurement costs significantly.

4. **Propose** an approach to measure the permittivity of multi-layered materials using transmitted power only.

## 1.4 Dissertation Outline

**Chapter 2** presents a novel concept based on electrically small antennas that eliminates multiple scattering and diffraction phenomena. This chapter shows a series of simulations that prove the ray-like behavior of electrically small antennas and their effects on diffraction and multiple scattering. Various experimental setups are also shown and tested, creating images of the object under test. Comparisons with other excitation sources are made to show the importance of excitation source selection on the image reconstruction approach.

**Chapter 3** introduces a novel approach to measure the complex permittivity of materials based on transmitted power. Simulations and experiments, conducted to show the high accuracy level of the proposed method without the need for phase information, result in removing the essential requirement of a vector network analyzer. Various liquids are tested both with our proposed setup and a well-known permittivity measurement system. The permittivity characterization method was expanded to measure the permittivity of multi-layered media with only power measurement. Different optimization algorithms are used to increase the speed of reconstruction algorithms.

**Chapter 4** offers conclusions and future steps that can potentially make the microwave imaging clinically available.

# Chapter 2

# Microwave Near-field Imaging

*If at first an idea does not sound absurd, then there is no hope for it.*

*"Albert Einstein"*

## 2.1 Introduction

Microwave imaging aims at generating a map of electrical properties, quantitatively or qualitatively, from the object under test. The frequency of excitation signals can be in the range of a few MHz to a few hundreds GHz. Microwave imaging has been widely used in different areas such as remote sensing, security scanning, and material science. However, microwave medical imaging is not still clinically available.

This chapter proposes a microwave imaging system, tested theoretically and practically, which creates images of the interior parts of an object under test. The excitation approach, scanning procedure, and the reconstruction method are all explained in detail. The objective is not just to have an impression of an OUT, as with X-ray images, but to have full images such as with computerized tomography (CT).

The proposed method is a strong candidate for medical applications, because of the size of the objects it can test, as well as the resolution, reliability and fast acquisition

time needed in medical imaging. Microwave imaging, as an imaging modality, can play a pivotal role in the early detection of cancer, with distinctive advantages over the available modalities such as magnetic resonance imaging (MRI), CT, and ultrasound. MRI, although it provides high-resolution images, needs an expensive setup and cumbersome procedure. CT scans, although not expensive compared to MRIs, use X-Rays, which results in ionizing the molecules of body. Ultrasound, on the other hand, cannot provide high-resolution images and is operation-dependent modality. These problems–significant cost, high health-risk, and immovable systems–of current modalities have placed barriers on acquiring enough images (i.e., in series over time) in cases where cancer might exist and frequent screening is required. Microwave Imaging, however, can solve these challenges. The high penetration of microwaves and low-cost of devices needed to generate images at these frequencies are the main features making this modality very attractive. Despite these advantages, microwave imaging faces a few challenge such as low-resolution images, multipath fading, a need for simulation models, prior information, and high computational resources. The microwave imaging approaches reported in the literature suffer from these challenges.

To address these challenges, we propose a novel approach to exciting objects under test, using electrically small radiation sources in the near field, so that diffraction phenomena are eliminated significantly. We apply the Radon transform and filtered-back projection technique, which is well-known in CT reconstruction algorithm, to image the OUT. Our simulation studies and experiment prove that the use of small-antennas can remove the effect of diffraction that occurs in the propagation medium. We prove that the waves propagate in straight lines, allowing us to excite the OUT slice by slice. Using the Radon Transform and filtered-back projection, as the image reconstruction algorithm, the need for simulation software is removed. Therefore, there is no need for high-computational resources, making the frequent screening easier than ever.

Our electrically small antennas are designed to deliver their maximum power at low frequencies, and are very narrowband and sensitive to small changes. Thus, they can detect small details in the human body. An antenna pair, i.e., an identical transmitter and receiver, is placed in a scanning system with the OUT located in between. The antenna pair scans the OUT on two parallel lines, referred to as parallel beam excitation. At each scan the power transmitted through the OUT is collected by the receiver, generating a

transmitted power profile versus the antennas location, referred to as the Radon transform. The antennas then rotate to scan the OUT at angles from 0 to $180^o$. The Fourier-slice theorem is then applied to the obtained transmitted profile to reconstruct the ultimate image. We have shown that the image obtained through this approach achieves a high resolution, mere fractions of a wavelength.

## 2.2 Classical Microwave Imaging

The classical microwave imaging involves the problem of inverse scattering, meaning that the excitation fields and the scattered ones are known but the object under test is not known. Such problem is usually ill-posed because the answer to the problem either may not exist or not unique. The ill-posedness problem can sometime be solved by applying regularization techniques but the obtained solution will be an approximate answer. Fig. 2.1 shows an object under test excited by incident waves. The inverse problem objective is to reconstruct any information about the $f(x, y)$ function, such as electrical properties distribution, $\epsilon(x, y)$ or $\sigma(x, y)$.

As an example of classical inverse scattering, we elaborate the formulation required to reconstruct a general linear isotropic medium. Starting with Maxwell equations we have:

$$\nabla \times E = -j\omega B(r) \tag{2.1}$$

$$\nabla \times H = j\omega D(r) + J(r) \tag{2.2}$$

$$\nabla \cdot D = \rho(r) \tag{2.3}$$

$$\nabla \cdot B = 0 \tag{2.4}$$

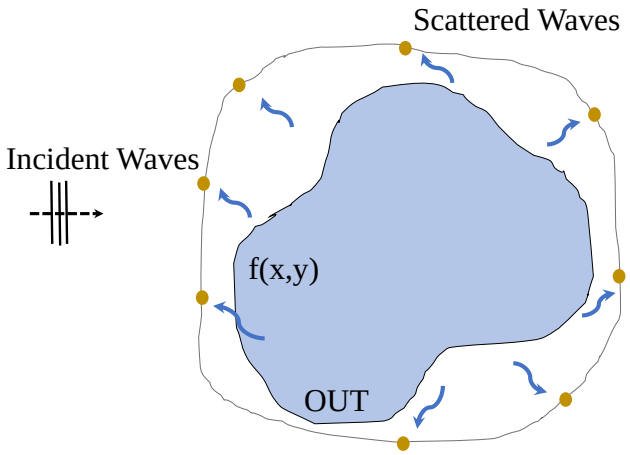


Figure 2.1: An object under test (OUT) interrogated by incident waves.

Taking the integration from (2.1) and (2.2) and using the Stoke theorem results in the following expressions

$$\oint_C E(r).dl = -j\omega \int_S B(r).\hat{n}ds \tag{2.5}$$

$$\oint_C H(r).dl = j\omega \int_S D(r).\hat{n}ds + \int_S J(r).\hat{n}ds \tag{2.6}$$

E and H are total electric fields which are constituted of incident fields and scattered fields:

$$E(r) = E_i(r) + E_s(r) \tag{2.7}$$

$$H(r) = H_i(r) + H_s(r) \tag{2.8}$$

where $E_i$, $E_s$ are incident, and scattered electric fields and $H_i$, $H_s$ are incident, and scattered magnetic fields, respectively.

If we substitute $B = \mu H$ and $D = \epsilon E$ in (2.5) and (2.6) one can obtain:

$$\oint_C E(r).dl = -j\omega \int_S \mu H(r).\hat{n}ds \tag{2.9}$$

$$\oint_C H(r).dl = j\omega \int_S \epsilon(r)E(r).\hat{n}ds + \int_S J(r).\hat{n}ds \tag{2.10}$$

If the OUT does not exist, (2.9) and (2.10) are modified as follows:

$$\oint_C E_i(r).dl = -j\omega \int_S \mu_b H_i(r).\hat{n}ds \tag{2.11}$$

$$\oint_C H_i(r).dl = j\omega \int_S \epsilon_b(r)E_i(r).\hat{n}ds + \int_S J(r).\hat{n}ds \tag{2.12}$$

Subtracting (2.11) and (2.12) from (2.9) and (2.10), respectively, results in scattered field equations:

$$\oint_C E_s(r).dl = -j\omega \int_S \left[\mu(r)H(r) - \mu_b(\, H - H_s(r)\,)\right].\hat{n}ds \tag{2.13}$$

$$\oint_C H_s(r).dl = j\omega \int_S \left[\epsilon(r)E(r) - \epsilon_b(\, E - E_s(r)\,)\right].\hat{n}ds \tag{2.14}$$

where

$$M_{eq} = j\omega(\mu_r - \mu_b)E(r) \tag{2.15}$$

$$J_{eq} = j\omega(\epsilon_r - \epsilon_b)E(r) \tag{2.16}$$

where $M_{eq}$ and $J_{eq}$ are equivalent magnetic and electric currents. Therefore, the objects can be removed because these equivalent currents results in creating the same E and H in free space as compared to when the object exists.

The other representation of (2.13) and (2.14), considering the green function of the medium, are as follows:

$$E_s(r) = j\omega\mu_b \int_V J_{eq}(r').\hat{G}(r/r')dr' + \int_V \nabla \times M_{eq}(r').\hat{G}(r/r')dr' \tag{2.17}$$

$$H_s(r) = j\omega\epsilon_b \int_V M_{eq}(r').\hat{G}(r/r')dr' - \int_V \nabla \times J_{eq}(r').\hat{G}(r/r')dr' \tag{2.18}$$

If the OUT is non-magnetic, $M_{eq} = 0$; therefore, (2.17) and (2.18) can be simplified to the following expression:

$$E(r) = E_i + j\omega\mu_b \int_V J_{eq}(r').\hat{G}(r/r')dr' \tag{2.19}$$

$$H(r) = H_i - \int_V \nabla \times J_{eq}(r').\hat{G}(r/r')dr' \tag{2.20}$$

Equations (2.19) and (2.20) can be considered for both forward scattering and inverse scattering problems. In the forward scattering one, the excitation fields as well as the entire structure is known so the only unknown will be the total electric field, E. In the inverse scattering problem, the total electric field is obtained by measurements outside the OUT but the material properties are unknown.

For practical scenarios such as medical applications no analytical solution exists, therefore, (2.19) and (2.20) are solved numerically. In forward scattering problems (2.19) is first solved to obtain the electric field inside the OUT. Then, the obtained electric field is used to solve the electric fields for outside the OUT. In inverse scattering problems (2.19) is considered two times. The first time (2.19) is solved for equivalent currents that generate the same electric fields as those are practically measured. The obtained equivalent current is then used to calculate the electric field inside the object under test which results in finding the properties of the OUT. Therefore, numerical simulations and modeling play important roles in inverse scattering, and thus of microwave imaging. If the environment modeling is done inaccurately, false images will be acquired [86].

## 2.3 Radon Transform and Filtered Back Projection

The reconstruction imaging method plays a pivotal role in creating OUT images. This thesis uses the Radon transform and filter back projection as the reconstruction method, which assumes that the OUT is interrogated by rays traveling in straight lines. This assumption is valid when the excitation frequency is very high, as in X-rays. In low frequencies, such an assumption is problematic because the wavelength is large and the diffraction phenomenon is significant. Therefore, the waves do not show ray-propagation behavior. This thesis, however, proposes the use of electrically small antennas, which reduces the effect of diffraction and the coupling between propagation paths. Consequently, the waves interact with the adjacent paths minimally, instead contributing primarily to the slice located between the transmitter and receiver. Hence, the main information collected by the receiver comes from the slice between the transmitter and receiver. This chapter shows a series of simulations and experiments that prove the ray-like behavior of electrically small antennas in the near field.

The use of electrically small antennas allows us to effectively utilize the Radon transform as the forward imaging process at low frequencies. The Radon transform, which was first introduced by Johann Radon in 1917, is the projection of an n-dimensional function onto an (n-1)-dimensional one. This transform represents the forward process of creating an image using filtered back projection. Filtered back projection is then used as the reconstruction method.

In this research, a two-dimensional function, $f(x, y)$, which is desired to be reconstructed is projected onto a one-dimensional profile, $g(\rho, \theta)$, where $\rho$ is the distance from the Y axis, and $\theta_l$ is the angle from the x axis. To explain the Radon transform in detail, consider $f(x, y)$ as a function that describes a two-dimensional cut of the original three-dimensional object, Fig. 2.2. The Radon transform operation, $\mathscr{R}\{.\}$, projects $f(x, y)$ to $g(\rho, \theta)$ along arbitrary lines $xcos\theta + ysin\theta = \rho$. Each single value of the g function corresponds to a line integral of $f(x, y)$. For example, $g(\rho = \rho_k, \theta = \theta_l)$ in Fig. 2.2 is a point that returns the projected value of $f(x, y)$ corresponding to the red line trace. In general,

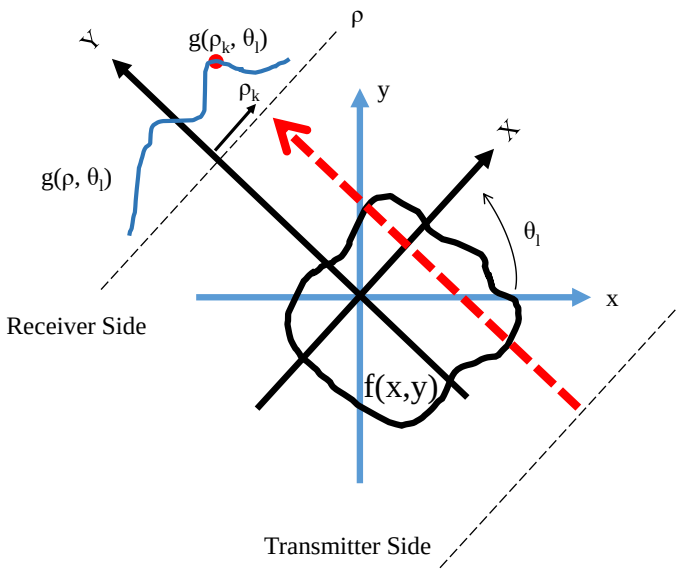


Figure 2.2: A 2-D slice of an OUT, f(x,y), and its projection along $\rho$ at an angle $\theta_l$.

the g function at an arbitrary angle $\theta$ along the $\rho$ line is calculated as follows

$$g(\rho,\theta) = \mathscr{R}\{f(x,y)\} = \int_{-\infty}^{\infty}\int_{-\infty}^{\infty} f(x,y)\delta(xcos\theta + ysin\theta - \rho)dxdy \tag{2.21}$$

where $\delta$ is the impulse function; $g(\rho,\theta)$ is obtained through parallel ray beam projections because (2.21) calculates the integral of $f(x,y)$ along the lines parallel to the Y axis and perpendicular to the $\rho$ line. In the real world, this parallel line represents the trace that the signal passes through.

In practice, we use the discrete form of (2.21) given by

$$g(\rho,\theta) = \sum_{x=0}^{M-1}\sum_{y=0}^{N-1} f(x,y)\delta(xcos\theta + ysin\theta - \rho)dxdy \tag{2.22}$$

where all the variables are discrete. The g function at each angle represents the information collected at the receiver side where the transmitter scans the $f(x,y)$ function along the $\rho$ line. Forming the g function is known as the forward process.

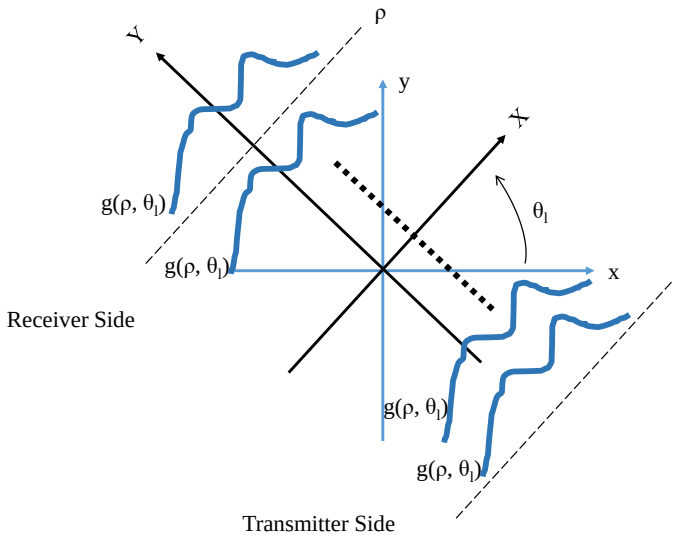


Figure 2.3: Back-projected $g(\rho, \theta)$ from the receiver to the transmitter.

The inverse process involves the back-projection of $g(\rho, \theta_l)$ at the same $\theta$ angle. At each angle, the $g(\rho, \theta)$ values are smeared out (copied) from the receiver side back to the transmitter side, Fig. 2.3. This process, referred to as back-projection, creates an image at the $\theta_l$ angle. Repeating the same process at all $\theta$s creates an approximate image of $f(x, y)$. The image is referred to as a laminogram, which is blurry and indistinct.

### 2.3.1 Backprojection of a Signal

An essential part of image reconstruction is the signal backprojection, which copies the projected profile obtained with the Radon transform, from the receiver side back to transmitter side. The mathematical representation of backprojection transform, $\mathscr{B}\{g(\rho, \theta)\}$, is as follows

$$\mathscr{B}\{g(\rho, \theta)\} = \int_0^{\pi} g(\rho cos(\theta - \phi), \phi) d\phi \tag{2.23}$$

Fig. 2.4 shows the process of back projection for two projections at angles 0 and $\pi/2$, [87]. The projection profiles are back projected toward the OUT at the original

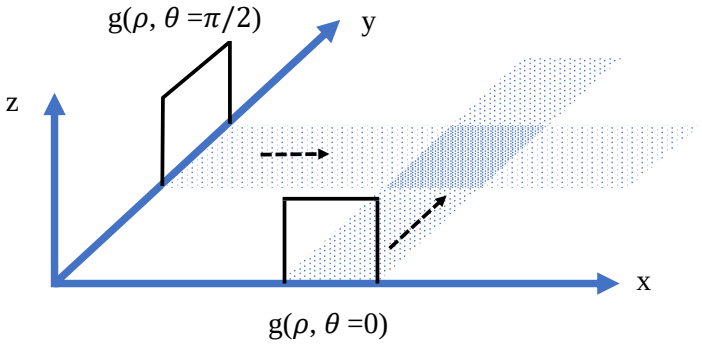


Figure 2.4: Backprojection of two projections acquired based on the Radon transform at two angles. Arrows show the direction of backprojection.

angles they were obtained at.

A simple conventional example can explain the Radon transform and the backprojection clearly. Fig. 2.5 shows a simple example of the Radon transform projections at different angles. The orange box is considered as the object under test, and the blue boxes are the projections at the receiver side.

Once the projections are obtained, the blue boxes in Fig. 2.5, the backprojection algorithm is applied to reconstruct the OUT, the orange box. Fig. 2.6(a) shows the algorithm procedure used to sum up the projection profiles when they are back projected toward the OUT/transmitter. If common terms are removed from the projections' sum, the result will be the OUT multiplied by a factor of 3, Fig. 2.6(b). Therefore, an approximation of the original OUT is created. The profile obtained in Fig. 2.6(b) is based on the sum of unfiltered projections, a laminogram.

The main problem with laminogram images is blurriness. When the backprojections are added up without any filtering, the low frequency samples dominate the high frequency ones, resulting in a blurry image with faded details. Fig. 2.7 shows this phenomenon in the frequency domain, the u-v plane. It is observed that the high frequency samples are sparse; therefore, they do not add up, unlike the low frequency ones. Thus, smooth parts of an image can be clearly seen in a laminogram while the sharp parts cannot. An exact

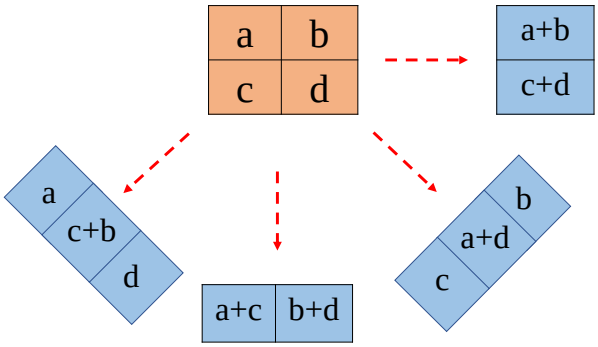


Figure 2.5: An example of the radon transform projection at different angles. The orange box represents the OUT and the blue boxes represent the projections at different angels.

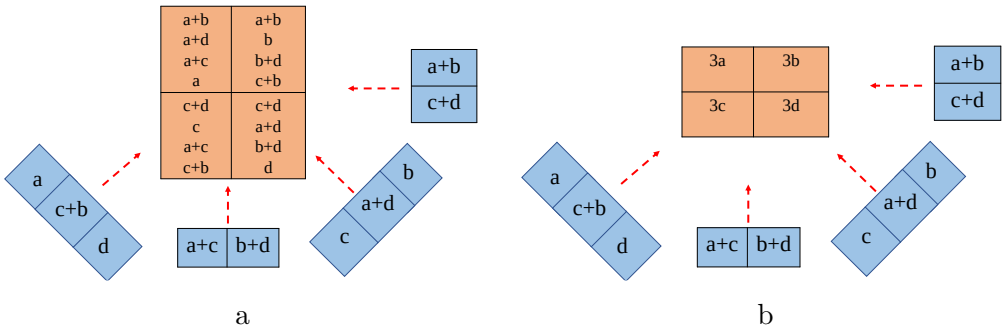


Figure 2.6: Backprojection of projection profiles toward the OUT at the same angles: a. when all projections are summed up, b. when the common terms in are removed.

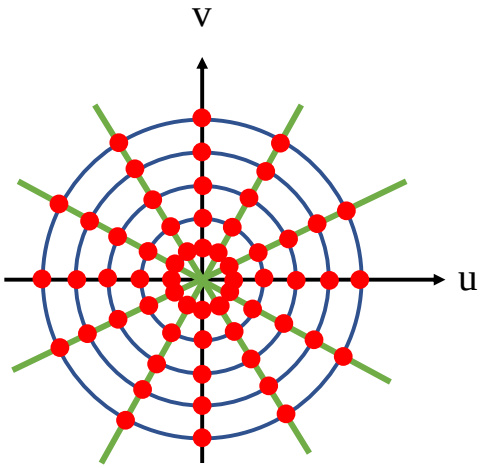


Figure 2.7: Frequency harmonics of the projections for different angles in the frequency domain.

image of the OUT can be achieved by applying the Fourier-slice theorem.

### 2.3.2 The Fourier-Slice Theorem

The image reconstruction in this research is based on the Radon transform and the Fourier-slice theorem, which states that the Fourier transform of each $g(\rho, \theta)$ projection with a period of T, $\mathscr{F}\{g\} = G(f)$, equals one slice of a two-dimensional spatial Fourier transform of the original function $f(x, y)$, $\mathscr{F}\{f(x, y)\} = F(u, v)$, Fig. 2.8. The following equation

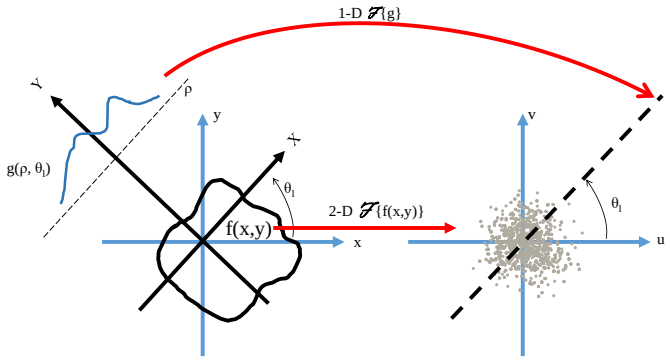


Figure 2.8: Fourier transform of g from the x-y to u-v planes along the $\theta_l$ angle.

proves the Fourier-slice theorem:

$$\begin{aligned} G(f,\theta) &= \int_{-\infty}^{\infty}\left[\int_{-\infty}^{\infty}\int_{-\infty}^{\infty} f(x,y)\delta(xcos\theta + ysin\theta - \rho)dxdy\right] e^{-j2\pi f\rho}d\rho \\ &= \int_{-\infty}^{\infty}\int_{-\infty}^{\infty} f(x,y)\left[\int_{-\infty}^{\infty}\delta(xcos\theta + ysin\theta - \rho)e^{-j2\pi f\rho}d\rho\right]dxdy \\ &= \int_{-\infty}^{\infty}\int_{-\infty}^{\infty} f(x,y)e^{-j2\pi f(xcos\theta+ysin\theta)}dxdy \\ &= \int_{-\infty}^{\infty}\int_{-\infty}^{\infty} f(x,y)e^{-j2\pi(ux+vy)}dxdy\Big|_{u=fcos\theta,v=fsin\theta} \end{aligned} \tag{2.24}$$

where $u = fcos\theta$ and $v = fsin\theta$.

Therefore:

$$G(f,\theta) = [F(u,v)]_{u=fcos\theta,v=fsin\theta} = F(fcos\theta, fsin\theta) \tag{2.25}$$

Equation (2.25) shows the connection between the projections based on the Radon transform and the original function to be reconstructed, $f(x,y)$. It is important to note that the Fourier transform of each projection with respect to $\rho$ at each angle $\theta_l$ is equal to the Fourier transform of $f(x,y)$ along the line with the same angle as that the projection is acquired at, Fig. 2.8.

To reconstruct $f(x,y)$, a two dimensional inverse Fourier transform of (2.24) needs to be taken

$$f(x,y) = \int_{-\infty}^{\infty}\int_{-\infty}^{\infty} F(u,v)e^{j2\pi(ux+vy)}dudv \tag{2.26}$$

substituting $u = fcos\theta$ and $v = sin\theta$ in (2.26) and using the Jacobian transformation as follows

$$\begin{aligned} dudv &= \det \begin{vmatrix} \frac{\partial u}{\partial f} & \frac{\partial u}{\partial \theta} \\ \frac{\partial v}{\partial f} & \frac{\partial v}{\partial \theta} \end{vmatrix} df d\theta \\ &= f dudv \end{aligned}$$

we have:

$$f(x,y) = \int_{0}^{2\pi}\int_{0}^{\infty} F(fcos\theta, fsin\theta)e^{j2\pi f(xcos\theta+ysin\theta)} f df d\theta \tag{2.27}$$

Substituting (2.25) in (2.27) results in

$$f(x,y) = \int_{0}^{2\pi}\int_{0}^{\infty} G(f,\theta)e^{j2\pi f(xcos\theta+ysin\theta)} f df df \tag{2.28}$$

Using the Fourier transform features (2.28) can be further simplified to the following relation

$$f(x,y) = \int_{0}^{\pi}\left[\int_{-\infty}^{\infty} |f|\, G(f,\theta)e^{j2\pi f\rho} df\right]_{\rho=xcos\theta+ysin\theta} \tag{2.29}$$

where

$$G(f,\theta) = \int_{-\infty}^{\infty} g(\rho,\theta)e^{-j2\pi f\rho} d\rho$$

$G(f,\theta)$ is the Fourier transform of $g(\rho,\theta)$ with respect to $\rho$.

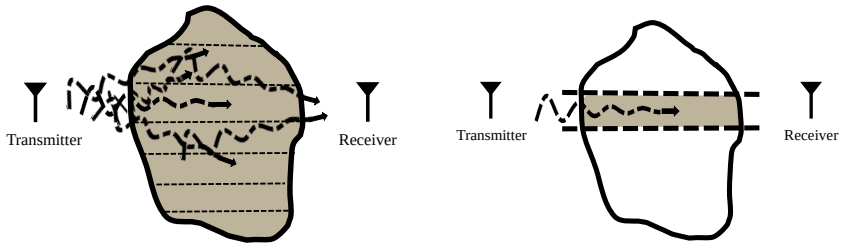


a b

Figure 2.9: Wave behavior when entering a body under test: a. when coupling to the adjacent layers occurs, b. when there is no or little coupling to the adjacent layers.

Equation (2.29) contains the whole procedure for reconstructing $f(x, y)$ function when the Fourier-slice theorem is used along with parallel-beam projections. Equation (2.29) states that summing up the inverse Fourier transform of all projections returns the entire $f(x, y)$ function, resulting a precise image generation.

Because of the existence of a ramp filter, $|f|$, in (2.29)) the integrand magnitude becomes very large when the bounds approach infinity. Therefore, integral evaluation becomes impossible, and the inverse Fourier transform is undefined. To solve this issue, the integrand needs to be multiplied by a low pass window in order to bring the high values down to zero. More details can be found later in this chapter and in [87–89].

### 2.3.3 Electrically Small Antennas and Ray Propagation

As discussed above, (2.29) can be used efficiently if the waves travel in straight lines, meaning that no coupling occurs to the adjacent layers, which is the case for X-rays as they propagate mainly in straight paths. In other words, the $g(\rho, \theta)$ profile should be obtained from ray-illumination. However, the operation frequency in the microwave band is much lower than that of X-rays, resulting in stronger diffraction. As an example, Fig. 2.9a shows a case wherein waves significantly interact with the adjacent layers of the body under test. The wave is bent from its straight path, so diffraction occurs. In this case, (2.29) does not return the proper image. However, this thesis will show that if the antennas used are

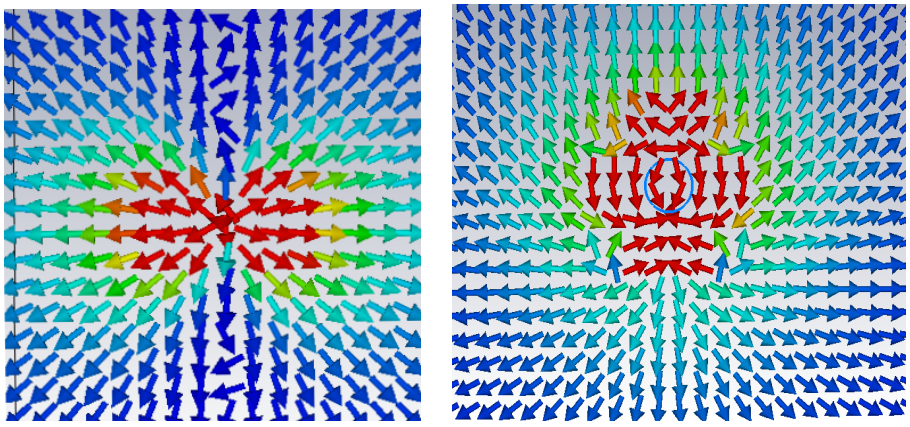

a b

Figure 2.10: Power flow for electrically small antennas, a. an electrically small dipole b. an electrically small loop

electrically very small, the coupling to other layers decreases significantly, and thus the waves act similar to X-rays, Fig. 2.9b, and less diffraction occurs. Hence, the layer located between the transmitter and receiver affects the information collected at the receiver much more than other layers do.

To show the ray-like behavior of electrically small radiation sources, a series of simulations has been done, some of which are presented here. To start, the power flow of an electrically small dipole is simulated and shown in Fig. 2.10a. It is observed that the power leaves the dipole and flows in straight paths, showing the ray like behavior of such small antenna. The same observation is made when an electrically small loop antenna is simulated, Fig. 2.10b.

Fig. 2.11a shows a slab made up of five different dielectrics with the thickness of s, height of h, and length of l. One antenna, as the transmitter, is placed at the middle left side of the slab at a distance of $d_T$, Fig. 2.11b. Five probes, as receiver antennas, are placed at the middle right of the slab. The transmitters and receivers are located on the z=0 plane. All receivers are the same distance $d_R$, from the slab, and, h, from each other, with the first receiver located at 4.5 h. The transmitter, a Hertzian dipole, excites the slab with a voltage value of 1 polarized in the y direction. The receiving probes record

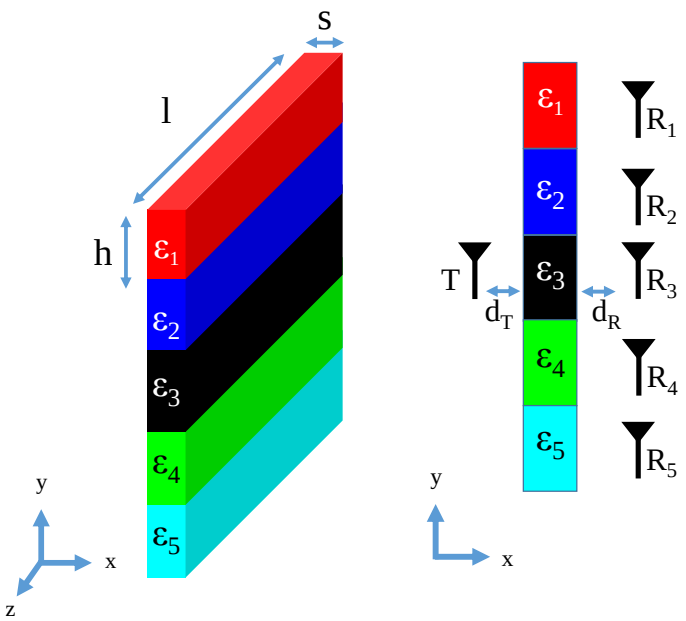


a b

Figure 2.11: A slab of dielectric with the thickness of s and length of l made up of five different permittivities each with the height of h: a. Three dimensional model b. Front view, where one transmitter is placed at the left and five receivers are placed at the right.

the electric field magnitude within the range of 100 MHz to 500 MHz. The dielectric permittivity values of the layers are set to $\epsilon_1 = 10, \epsilon_2 = 3, \epsilon_3 = 8, \epsilon_4 = 5$ and $\epsilon_5 = 2$. The simulations are run twice to compare the effect of electrically small and large antennas on the coupling. In the first simulation, the transmitter length is set to $\lambda/100$ and in the second one, to $\lambda/5$, where $\lambda$ is the wavelength center. The slab dimensions remain the same, $s = \lambda/50$, $h = \lambda/25$, $d_T = d_R = \lambda/200$, and $l = \lambda$.

Fig. 2.12a and b show the results of these experiments when the transmitter lengths are $\lambda/100$ and $\lambda/5$, respectively. In Fig. 2.12a and b, $R_3$, which is exactly in front of the transmitter, receives the maximum electric and magnetic fields compared to other receivers, meaning that the third layer contains dominant wave information. In contrast, Fig. 2.12c and d show that $R_3$ no longer receives the dominant fields, meaning that coupling

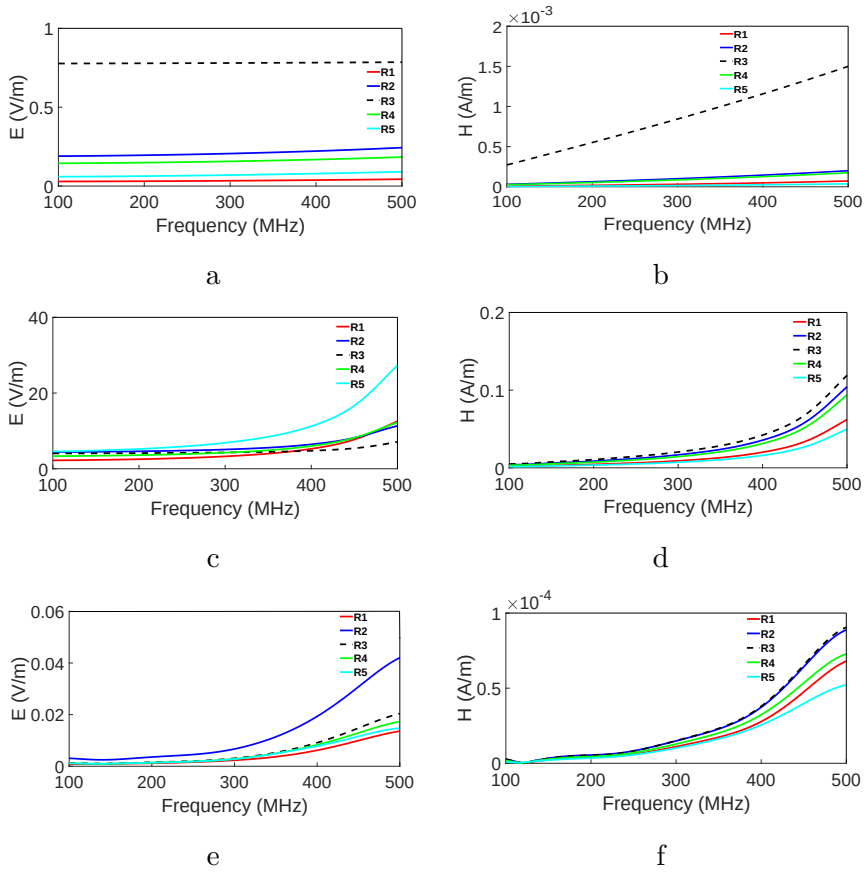


Figure 2.12: Measured fields by the five receivers shown in Fig. 2.11 as a function of frequency. a Electric fields and b. magnetic fields when the transmitter length is set to $\lambda/100$ and slab thickness to $s = \lambda/50$, c. Electric fields and d. Magnetic fields when the transmitter length is set to $\lambda/5$ and slab thickness to $s = \lambda/50$, e. Electric fields and f. Magnetic fields when the transmitter length is $\lambda/100$ but the slab thickness changes to $s = \lambda/5$.

occurs and the waves energy packets are divided between all the layers. Therefore, if the transmitter length is electrically very small, the straight path between the transmitter and $R_3$ contributes as the most influential layer. If not, the effects of other layers become more significant. Due to the strong diffraction, (2.29) cannot be used effectively. In the next experiment, the transmitter length is set to $\lambda/100$, and this time, the thicknesses of the slab layers, s, are changed to $\lambda/5$. Fig. 2.12 e and f show the results of this simulation. In this case, also, $R_3$ no longer receives the maximum electric field. Comparing Fig. 2.12a and b with Fig. 2.12 e and f shows that if the layers are not electrically small as well, strong coupling between them occurs, violating the ray-like behavior of the waves. Fig. 2.13 shows the real power collected by the receivers, confirming the same conclusions. It is important to note that since the ray-like behavior is observed for both electric and magnetic fields; power, which is the cross product of E and H, shows a more significant difference between the collected power by $R_3$ and other receivers. Therefore, we use power information to reconstruct images.

To show how fields are distributed in the slab when an electrically small antenna excites the structure, the electric fields, magnetic fields, and power are plotted in Fig. 2.14. It is observed that the third layer contributes the most to the fields, and therefore power. Hence, $R_3$ receives the maximum of electric fields, magnetic fields, and power. If the slab thickness is set to $\lambda/5$, Fig. 2.15 shows that $R_3$ no longer receives the maximum power.

The coupling between layers, as discussed in the introduction, significantly affects the highest resolution that can be achieved. The next experiments are dedicated to investigating the effect of sources such as plane waves and infinite lines on resolution, comparing it to that an electrically small antenna can provide.

The slab shown in Fig. 2.11 is designed this time such that $h = \lambda/10$, $s = \lambda/100$, and $l = \lambda$. The center frequency is 300 MHz, and the permittivity constants for segments are $\epsilon_1 = 1, \epsilon_2 = 15, \epsilon_3 = 15, \epsilon_4 = 5$ and $\epsilon_5 = 20$. This experiment contains three simulations: first, an electrically small dipole with a length of $\lambda/100$ is placed at the left side of the slab polarized in the positive z-direction with the current amplitude of 1 A. A probe is also placed at the right side of the slab at the same y coordinate as the transmitter, so both transmitter and receiver are exactly opposite each other to run a parallel scan. They are both located at the distance of $d_T = d_R = \lambda/500$ from the slab. Both transmitter and

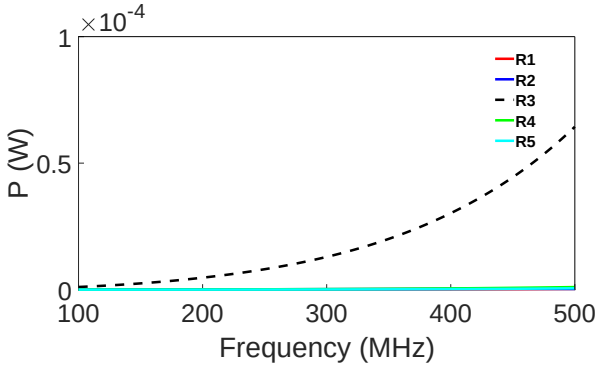


a

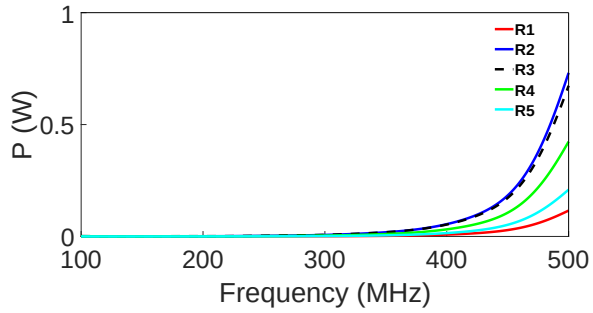


b

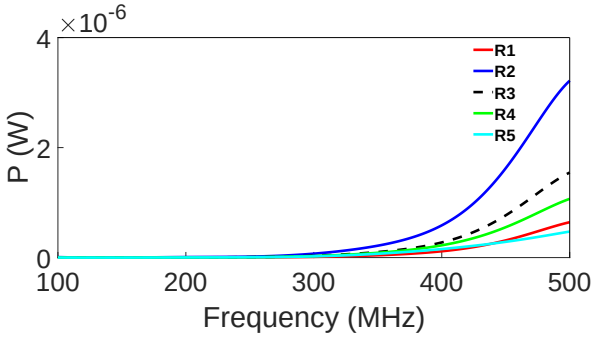


c

Figure 2.13: Collected real power measured by the five receivers shown in Fig. 2.11 as a function of frequency. a. When the transmitter length is set to $\lambda/100$ and slab thickness to $s = \lambda/50$, b. When the transmitter length is set to $\lambda/5$ and slab thickness to $s = \lambda/50$, c. When the transmitter length is $\lambda/100$ but the slab thickness changes to $s = \lambda/5$.

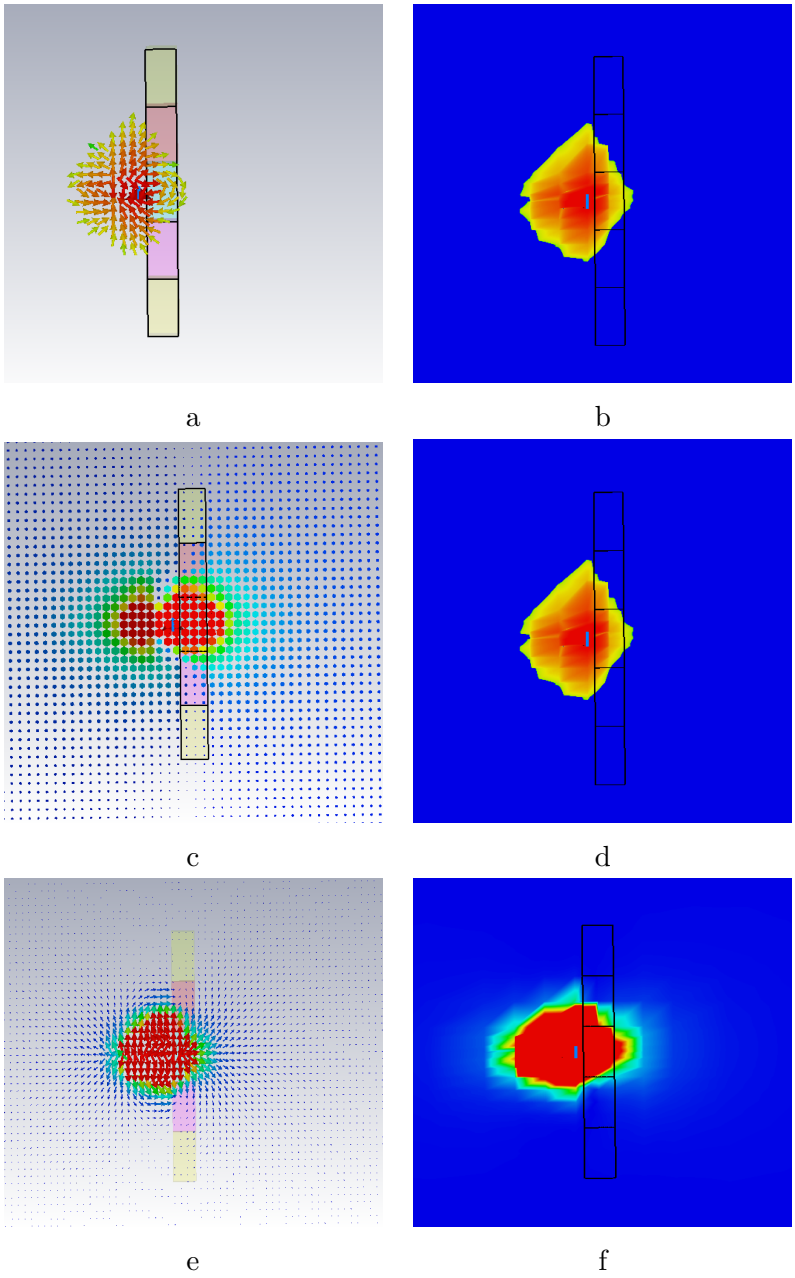


Figure 2.14: Arrow and contour plot for electric and magnetic fields, and power distribution when the structure shown in Fig. 2.11 with a slab thickness of $s = \lambda/50$ is excited by a transmitter with a length of $\lambda/100$. a and b. Electric fields distribution, c and d. Magnetic fields distribution, e and f. Power distribution.

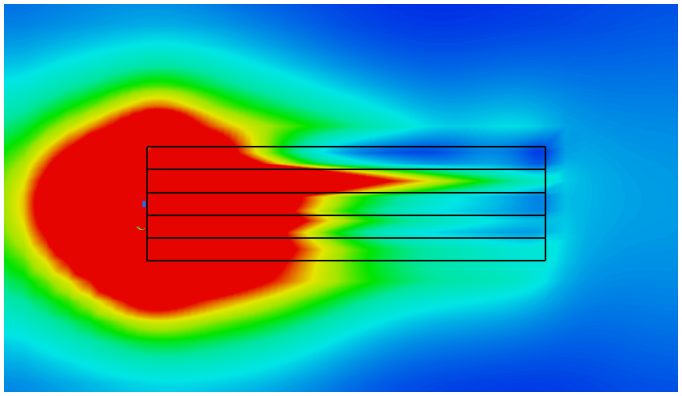

Figure 2.15: Power distribution for the slab shown in Fig. 2.11 when When the transmitter length is set to $\lambda/100$ and slab thickness to $s = \lambda/5$.

receiver are moved at the same time along the y-axis from -$\lambda/2$ to +$\lambda/2$, and the electric field is captured and recorded by the receiver. The electric field profile as a function of Y is plotted in Fig. 2.16a. If the resolution is defined as the accuracy level in detecting the permittivity value changes, Fig. 2.16a shows that the use of electrically small antenna creates very high resolution, less than $\lambda/50$.

In the next simulation, the same slab with all its parameters as well as the receiver remain unchanged. The slab is then excited by an infinite current line instead of by the electrically small dipole. The current line is placed on the left side of the slab along the z-axis with the same (x,y) location as that of the electrically small dipole. The current runs through the wire in the positive z-direction with an amplitude of 1 A. The line scans the slab along the y-axis from -$\lambda/2$ to +$\lambda/2$, and the electric field is recorded by the receiver at the other side, Fig. 2.16b. The resolution obtained in this case is significantly lower than that achieved by the electrically small antenna excitation.

In the next simulation, the current line is replaced by a plane wave with the electric field incident polarized in the positive z-direction. All other parameters remain unchanged. The receiver is then scanned from -$\lambda/2$ to +$\lambda/2$, and the electric field is recorded at each position. Fig. 2.16c shows the result where the resolution achieved is higher than that of the infinite line but lower than that of the electrically small antenna. Therefore, the use of the electrically small antenna results in the highest resolution here. Fig. 2.16a-c also

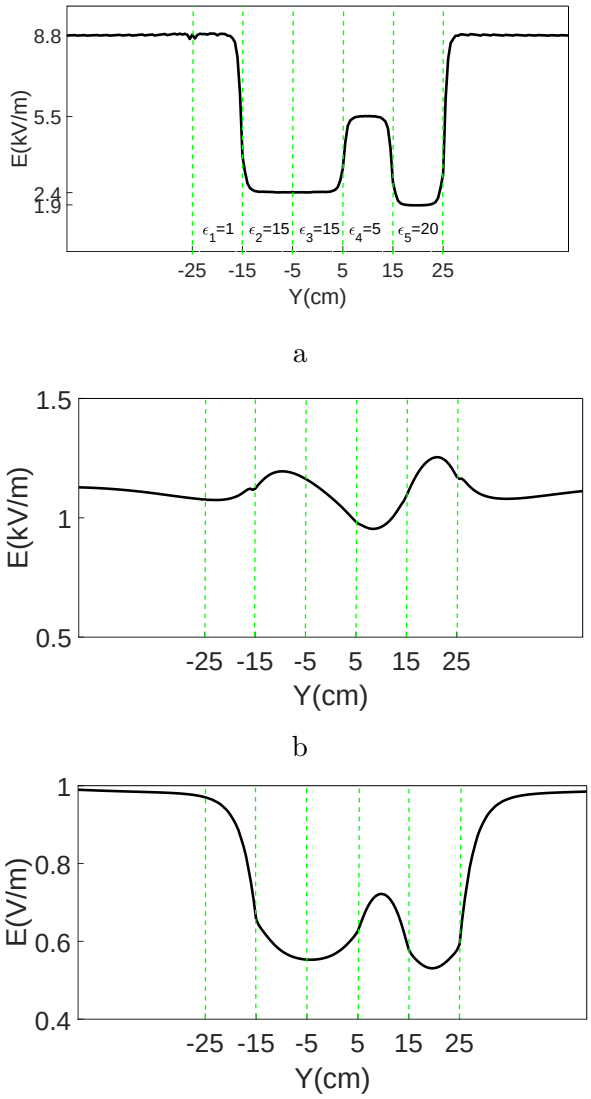


Figure 2.16: Electric field profile recorded by the receiver as a function of y-location. a. When an electrically small antenna with a length of $\lambda/100$ is used; b. Infinite line excitation; c. plane wave excitation.

reveals the consistency in the electric field magnitude level captured by the receiver and affected by the permittivity values. Fig. 2.16a, which has the highest resolution, shows that the value of the electric field consistently changes as the permittivity changes. For example, when the permittivity is 1, the electric field magnitude is 8.8 kV both in $Y \leq -25$ cm and $Y \geq +25$ cm.

The last series of simulations investigates how resolution is affected by the receiver location, $d_R$, with respect to the OUT. In this experiment, the slab's dimensions and its dielectric profile remain unchanged, but $d_R$, the receiver location, is set in series to $\lambda/50, \lambda/10, \lambda/5$ and $2\lambda$. Fig. 2.17a-d shows the electric field profile as a function of location where an electrically small antenna with a length of $\lambda/100$ and $d_T = \lambda/100$ scans the slab. It is observed that increasing the receiver distance degrades the resolution but the change in dielectric is still detectable at $2\lambda$ from the OUT. Fig. 2.17e-h shows the same scenario but with a plane wave excitation instead of the electrically small antenna. It is clearly seen that after a fraction of a wavelength, $\lambda/5$, the resolution is completely gone, and at $2\lambda$, no information from the near field is observed. Comparing Fig. 2.17d and h sheds light on this phenomena; if an electrically small antenna is used, the near field information will last for a longer distance than that of a plane wave excitation. It can be seen that for the plane wave when $d_R = \lambda/5$, almost all the near field information has faded in Fig. 2.17f.

In conclusion, because of the ray-like behavior of electrically small antennas and their capability in creating high resolution profiles, imaging is possible at low frequencies with a high resolution by using (2.29).

### 2.3.4 Reconstruction Procedure

Equation (2.29) requires the projection profile of the object under test, $g(\rho, \theta)$. In the CT, $g(\rho, \theta)$, is the absorption or attenuation of the signal passing through the body [10]. Each line integral in (2.21) expresses the absorption or attenuation along the straight line that the wave travels, Fig 2.18. In this thesis $g(\rho, \theta)$ is defined as the received power, S21.

Fig. 2.18 shows an electrically small transmitting antenna while scanning the OUT along the $\rho$ line at an arbitrary angle $\theta_l$. Another antenna collects the received power, S21,

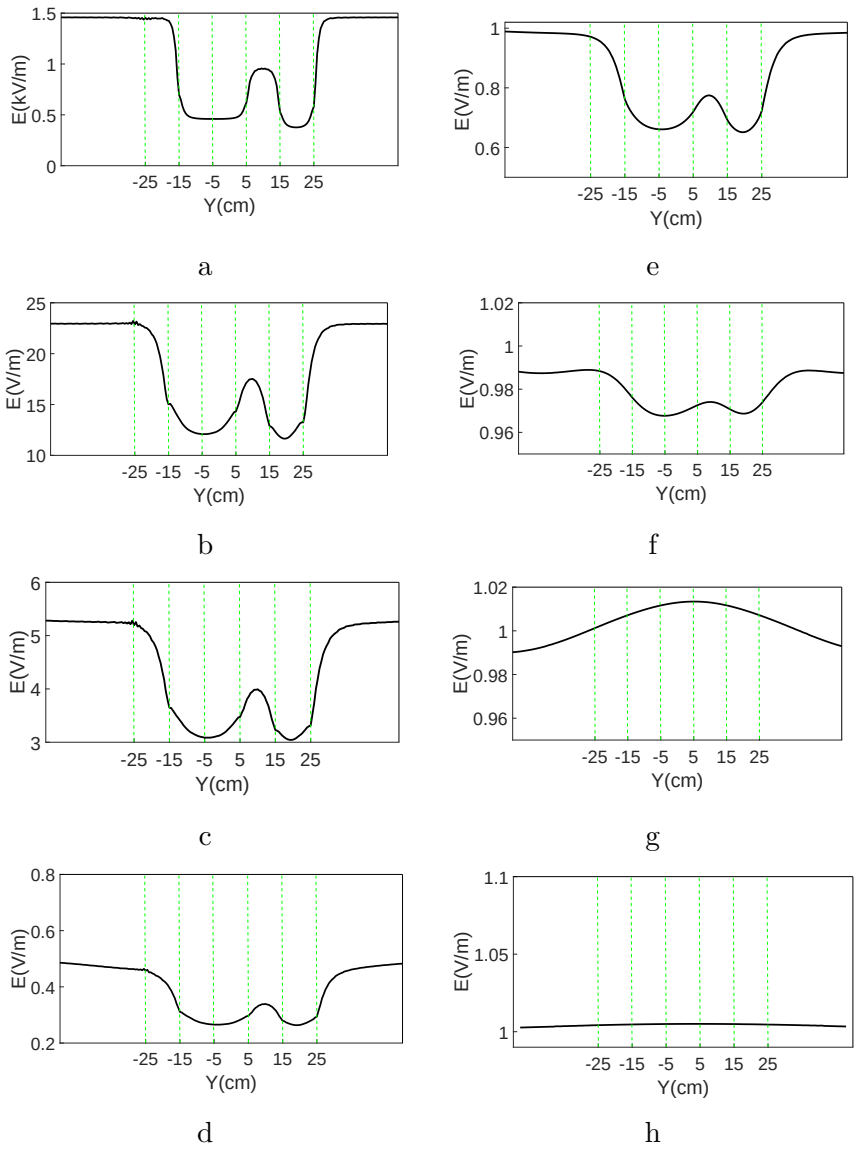


Figure 2.17: Electric field profile as a function of location for various $d_R$s. An electrically small antenna is used, and the receiver locations are a. $d_R = \lambda/50$, b. $d_R = \lambda/10$, c. $d_R = \lambda/5$, d. $d_R = 2\lambda$, and plane wave excitation is applied when e. $d_R = \lambda/50$, f. $d_R = \lambda/10$, g. $d_R = \lambda/5$, and h. $d_R = 2\lambda$.

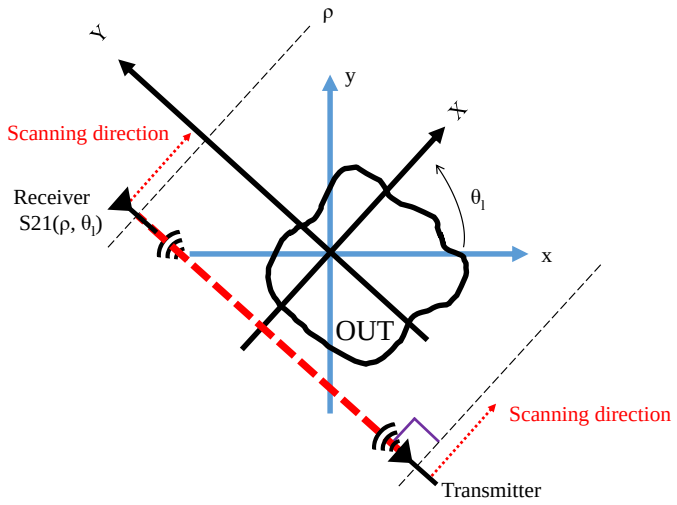


Figure 2.18: A pair of electrically small transmitter-receivers scanning the OUT at an arbitrary angle $\theta_l$ along the $\rho$ line.

simultaneously on the other side of the OUT. Therefore, $g(\rho, \theta_l)$ is referred to as the received power along $\rho$ at angle $\theta_l$. Both transmitter and receiver have the same characteristics. The scanning is done in a parallel-beam approach, meaning that the lines of integrals in (2.21) are perpendicular to the scanning direction, Fig. 2.18.

Equation (2.29) involves the Fourier transform of $g(\rho, \theta)$, but g is a finite function because the scanning space is finite, therefore, inherently not periodic. If the antennas scan the OUT from -L/2 to L/2 in the $\rho$ direction, g is also limited to between -L/2 to L/2. Therefore, g has a length of L in the $\rho$ direction, where L is usually related to the maximum size of the OUT. So larger objects require larger scanning space. To solve the periodicity of g, this function must be copied repeatedly with a period of T. If T=L, then the ultimate image resolution will not be high because the periodic g has less similarity to the original g function. To increase the resolution, the g function needs to be padded on both its sides, meaning that the end values of g on each side are copied for an arbitrary length. This process makes the g function more similar to the practical case, where outside of the scanning space, the received signal is at minimum. Padding makes the frequency domain smoother, thereby enhancing the resolution [10]. The pad length on each side in

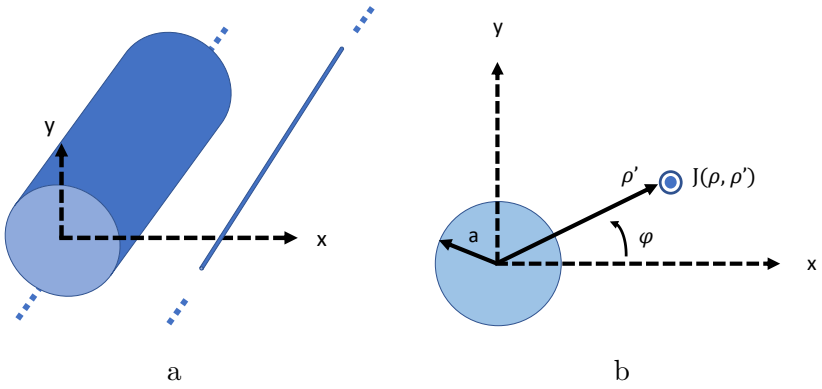


Figure 2.19: An infinite cylinder in the presence of an infinite line.

this thesis is set to be equal to the signal length; therefore, the padded g has a length of 3L=T.

The fast Fourier transform (FFT) of the padded signal is then taken and the result is multiplied by $|f|$ and a hamming window. This hamming window acts as a low-pass filter to cut down the higher integrand values in (2.29) when the bounds approach infinity. Next, an inverse Fourier transform (IFFT) is taken from the filtered signal, and the result is back-projected from the receiver side to the transmitter one, Fig 2.3. The whole process needs to be repeated for all angles from 0 to $\pi$, with an angle step $\Delta\theta$. In the end, all the back-projections are summed up, creating the image.

## 2.4 Theoretical Results for Cylindrical Objects

This section focuses on analytical calculation for cylindrical objects, as OUTs, in the presence of infinite current lines, Fig. 2.19. The Radon transform and filtered-back projection are applied to reconstruct the objects' images.

The cylinder has a radius of "a" with a permittivity of $\epsilon_r$. The propagation constant inside the cylinder is $k_1$ and outside of that, which is free-space, is $k_0$. An infinite current line, parallel to z-axis, is located at $\rho = \rho'$ with a value of $J = \delta(\rho - \rho')\hat{z}$.

Based on the Lorentz condition and the structure's symmetry, the only electric field component exists is $E_z$, and the only magnetic field is $H_\phi$, which are obtained as follows:

$$E_z = \begin{cases} \sum_{n=-\infty}^{\infty} A_n J_n(k_1\rho) e^{jn(\phi-\phi')} & \rho \le a \\ \sum_{n=-\infty}^{\infty} \left[ B_n J_n(k_0\rho) + C_n H_n^{(2)}(k_0\rho) \right] e^{jn(\phi-\phi')} & a < \rho < \rho' \\ \sum_{n=-\infty}^{\infty} D_n H_n^{(2)}(k_0\rho) e^{jn(\phi-\phi')} & \rho \ge \rho' \end{cases} \tag{2.30}$$

$$H_\phi = \frac{1}{j\omega\mu} \frac{\partial E_z}{\partial \rho} \tag{2.31}$$

$$H_\phi = \frac{1}{j\omega\mu} \begin{cases} \sum_{n=-\infty}^{\infty} A_n k_1 J_n'(k_1\rho) e^{jn(\phi-\phi')} & \rho \le a \\ \sum_{n=-\infty}^{\infty} \left[ B_n k_0 J_n'(k_0\rho) + C_n k_0 H_n^{(2)'}(k_0\rho) \right] e^{jn(\phi-\phi')} & a < \rho < \rho' \\ \sum_{n=-\infty}^{\infty} D_n k_0 H_n^{(2)'}(k_0\rho) e^{jn(\phi-\phi')} & \rho \ge \rho' \end{cases} \tag{2.32}$$

where J and H are Bessel and Hanckle functions. The distance from the origin is $\rho$, and the angle with respect to the x-axis is $\phi$. The coefficients, $A_n, B_n, C_n$, and $D_n$ are all unknown and need to be calculated.

Boundary conditions must be applied to solve the unknown coefficients:

at $\rho = a$:

$E_z(\rho = a^-) = E_z(\rho = a^+)$,

$$A_n J_n(k_1 a) e^{jn(\phi-\phi')} = \left[ B_n J_n(k_0 a) + C_n H_n^{(2)}(k_0 a) \right] e^{jn(\phi-\phi')}$$

therefore:

$$A_n J_n(k_1 a) = B_n J_n(k_0 a) + C_n H_n^{(2)}(k_0 a) \tag{2.33}$$

$H_\phi(\rho = a^-) = H_\phi(\rho = a^+)$,

$$A_n k_1 J_n'(k_1 a) e^{jn(\phi-\phi')} = \left[ B_n k_0 J_n'(k_0 a) + C_n k_0 H_n^{(2)'}(k_0 a) \right] e^{jn(\phi-\phi')}$$

thus:

$$A_n k_1 J_n'(k_1 a) = B_n k_0 J_n'(k_0 a) + C_n k_0 H_n^{(2)'}(k_0 a) \tag{2.34}$$

and at $\rho = \rho'$:

$E_z(\rho = \rho'^-) = E_z(\rho = \rho'^+)$,

$$\left[B_n J_n(k_0\rho') + C_n H_n^{(2)}(k_0\rho')\right] e^{jn(\phi-\phi')} = D_n H_n(^2)(k_0\rho') e^{jn(\phi-\phi')}$$

therefore:

$$B_n J_n(k_0\rho') + C_n H_n^{(2)}(k_0\rho') = D_n H_n^{(2)}(k_0\rho') \tag{2.35}$$

$H_\phi(\rho = \rho'^+) - H_\phi(\rho = \rho'^-) = j\omega\mu J_{zs}$, where:

$$J_{zv} = \delta(\rho - \rho') = \frac{1}{\rho'}\delta(\phi - \phi')\delta(\rho - \rho') \tag{2.36}$$

To obtain the surface current at $\rho = \rho'$, an integration with respect to $\rho$ is taken:

$$J_{zs} = \frac{1}{\rho'}\delta(\phi - \phi') \tag{2.37}$$

where

$$\delta(\phi - \phi') = \frac{1}{2\pi}\sum_{n=-\infty}^{\infty} e^{jn(\phi-\phi')} \tag{2.38}$$

$$D_n k_0 H_n^{(2)'}(k_0\rho') e^{jn(\phi-\phi')} - \left[B_n k_0 J_n'(k_0\rho') + C_n k_0 H_n^{(2)'}(k_0\rho')\right] e^{jn(\phi-\phi')} = \delta_{zs}(\rho - \rho')$$

thus

$$D_n k_0 H_n^{(2)'}(k_0\rho') - B_n k_0 J_n'(k_0\rho') - C_n k_0 H_n^{(2)'}(k_0\rho') = \frac{j\omega\mu}{2\pi\rho'} \tag{2.39}$$

With these four equations (2.33)-(2.39), the four unknown coefficients can be obtained. The equations are solved using matrix inversion, $X = A^{-1}B$, where A is the matrix's

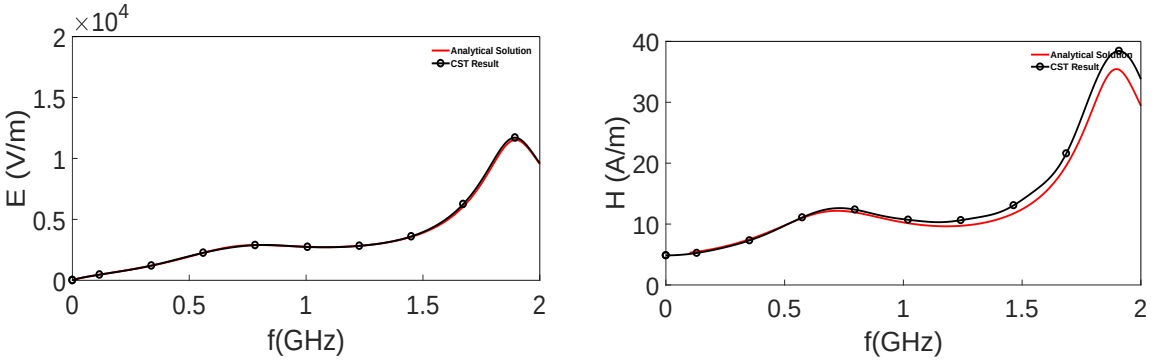


a b

Figure 2.20: Electric fields and magnetic fields comparison over frequency between the analytical solutions provided here and CST simulations for a dielectrical cylinder with a radius of 1.5 cm and permittivity of 15: a. E-field, b.H-field

known coefficients, X is the vector of unknown coefficients, and B is the vector of source values.

$$\begin{bmatrix} J_n(k_1a) & -J_n(k_0a) & -H_n^{(2)}(k_0a) & 0 \\ k_1J_n'(k_1a) & -k_0J_n'(k_0a) & -k_0H_n^{(2)'}(k_0a) & 0 \\ 0 & J_n(k_0\rho') & H_n^{(2)}(k_0\rho') & -H_n^{(2)}(k_0\rho') \\ 0 & -k_0J_n'(k_0\rho') & -k_0H_n^{(2)'}(k_0\rho') & k_0H_n^{(2)'}(k_0\rho') \end{bmatrix} \begin{bmatrix} A_n \\ B_n \\ C_n \\ D_n \end{bmatrix} = \begin{bmatrix} 0 \\ 0 \\ 0 \\ \frac{j\omega}{2\pi\rho'} \end{bmatrix}$$

To verify the solution provided here, a CST simulation is implemented. A dielectrical cylinder, Fig. 2.19, with a radius of 1.5 cm and permittivity of 15 is excited with an infinite line of current with a value of 1 A/m.

It is seen from Fig. 2.20 that analytical solutions for both electric field and magnetic fields are in close agreement with CST results. The cylinder is then scanned in the X direction and the collected power density on the receiver side is calculated from the following equation:

$$P = \frac{1}{2} Re\left[E \times H^*\right] \tag{2.40}$$

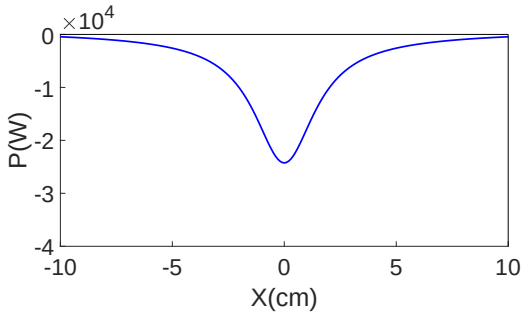


Figure 2.21: Received power versus X direction.

Fig. 2.21 shows the real power density for the cylinder when the infinite line scans the object in the X direction. Since the structure has a symmetry with $\phi$, the scanning results for all direction are the same. The filtered back-projection is then applied to reconstruct the cylinder image.

Fig. 2.22 shows the reconstructed image using the real power calculated analytically in Fig. 2.21 for various angle steps. (a) shows the results when only 2 projections with an angle-step $90^o$ are used; (b) shows the image when 4 projection are used with an angle-step $45^o$; (c) 19 projections are used with an angle-step $10^o$ (c) 179 projections are used with an angle-step $1^o$. It is seen that decreasing the difference between each step enhances the image resolution.

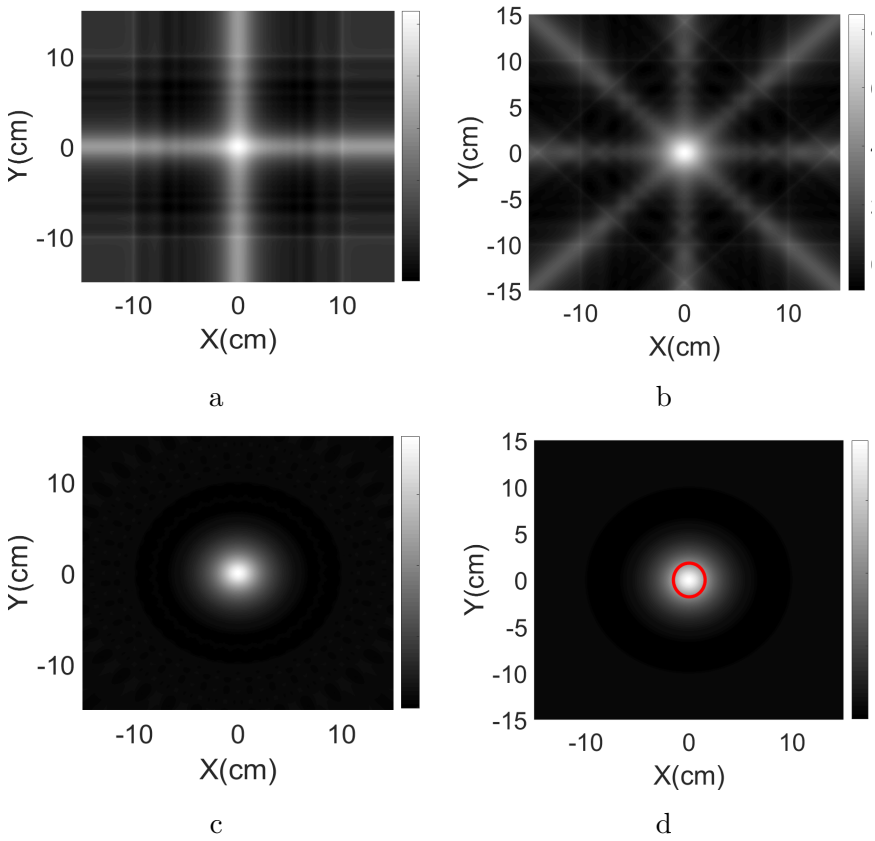


Figure 2.22: Reconstructed image for a dielectrical cylinder using the power-profile obtained in Fig. 2.21 when various steps in angle are taken: a. $90^o$ angle step b. $45^o$ angle step c. $10^o$ angle-step d. $1^o$ angle step.

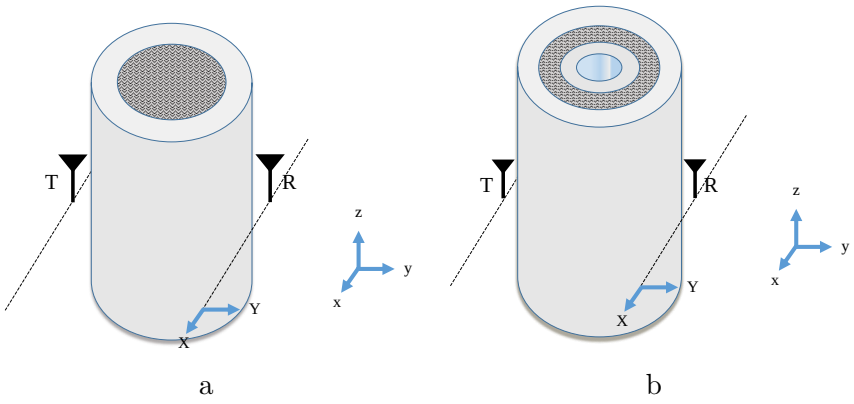


Figure 2.23: Two cylindrical objects filled with sand-water placed between a transmitter and receiver a. two-layer cylinder b. four-layer cylinder.

## 2.5 Experimental Results

In order to verify that the concept presented in this research practically, two symmetrical objects, both non-homogeneous, are studied, Fig. 2.23. The objects' symmetry with respect to $\theta$ allows us to reduce the number of measurements required at this stage. Therefore, the OUTs are only scanned from one angle, as the results will be similar to those from other angles.

Fig. 2.23a shows a Plexiglas cylindrical shell placed between a transmitter-receiver antenna pair. The shell has a height of 30 cm, an outer diameter of 3.8 cm, and a wall thickness of 3 mm, and is filled with a mixture of 80% sand and 20% water. The Plexiglas has a dielectric constant of almost 2.3. Both transmitter and receiver antennas have the same z locations, centered at the middle length of the cylinder at z=15cm. The antennas scan the cylinder from -5 cm to 5 cm along the X-axis on two parallel lines, with a sampling step of 1 mm. Each line is 1mm away the cylinder. Although (2.29) requires the antennas to move and scan the OUT, the same results can be obtained with the antennas fixed and the OUT moving and rotating, which eliminates the noise of antenna and cable movements.

The antennas are two electrically small dipoles with the strip width of 3 mm, a gap of 1 mm, and arm lengths of 2 cm, Fig 2.24a. Two inductors, Ls and Lp, make up

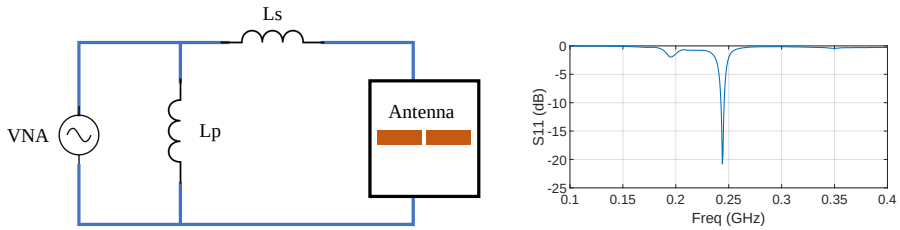


a b

Figure 2.24: The dipole antenna and its reflection response a. A strip dipole connected to a matching network and vector network analyzer. b. Measured reflection response of the dipole antenna with its matching circuit.

the antennas' matching network, needed to deliver and receive their maximum power at 244MHz. $Ls = 0.58\ \mu H$ and $Lp = 1.18\ nH$. Fig 2.24b shows the S11 of these identical dipoles and the matching network. Since lumped elements are used to match the antenna the reflection response is very narrow band with only 2% bandwidth. The substrates that hold the dipoles are made of 4 mm thick Plexiglas. Both transmitter and receiver are connected through two 50 Ω coaxial cables to an E5071C Agilent vector network analyzer. Fig. 2.25 shows the scanning setup, including the transmitter, receiver, OUT, positioner, vector network analyzer, and two 50 Ω cables.

As discussed, the function needed to reconstruct the image of this cylinder is S21; therefore, at each scan, the receiver collects the relative transmitted power. Fig. 2.26 shows the S21 profile as a function of the cylinder's location. It is observed that where no object exists between the transmitter and receiver, the received power is constant as expected. S21 starts dropping at -2.5 cm and increasing at 0. This 2.5 cm range is very close to the cylinder radius, 2.2 cm, confirming that the transmitter-receiver pair can capture electrically small variations.

The obtained S21 function is then used as the g function for reconstructing the image. If the OUT is rotated, the same results are obtained because of the object's symmetry, meaning that the same profile is obtained at other angles. Therefore, the same S21 profile is considered for other angles. The sampling step chosen in the $\theta$ direction is $\Delta\theta = 1^o$. The

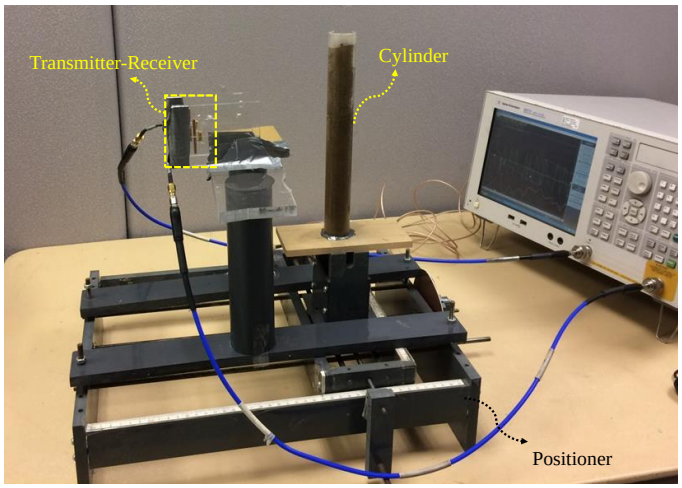


Figure 2.25: The measurement setup for the OUT shown in Fig. 2.23a. The entire setup includes the transmitter and receiver, OUT, 50 Ω cables, positioner, and vector network analyzer.

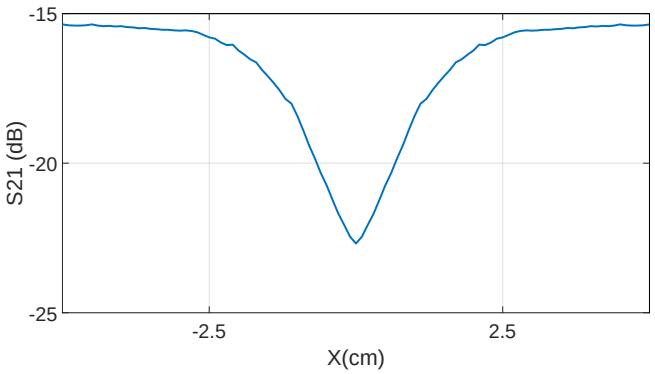


Figure 2.26: The power profile, S21, collected by the receiver as a function of location when the cylinder shown in Fig. 2.23a is scanned between the transmitter and receiver.

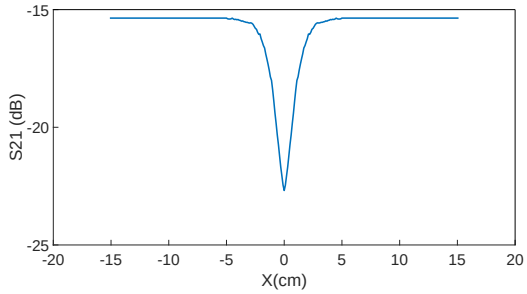


Figure 2.27: The padded signal of the original projection profile shown in Fig. 2.26.

obtained signals are then padded with a length of T from each side; therefore, the resulting padded is 3T long, Fig. 2.27, meaning that the periodicity length has been increased three times, which enhances the ultimate image resolution.

If the padded signal without any filtering is back projected to create an image, a laminogram is created. Fig. 2.28's laminogram is very blurry, and the details are lost, as expected. To increase the resolution, the padded signal is multiplied by a hamming window and ramp filter, Fig. 2.29, to enhance the high frequency components.

An FFT is taken from the padded signal, then multiplied by the filter to degrade the lower frequency harmonics instead amplifying the higher ones. The result is then inverted back to the space domain using IFFT. Fig. 2.30 shows the filtered signal with the changes amplified.

A sinogram image for Fig. 2.23a is shown in Fig. 2.31. A sinogram is made up of the projection profiles obtained at different angles. Although it is hard to interpret such images, it is very useful to observe the projection profiles at different angles separately. In Fig. 2.31 the projection profiles for all angles are the same since the object is symmetrical.

Therefore, if the procedure explained in the previous section is followed, the image for the OUT is reconstructed with the use of (2.29). Fig. 2.32 shows the image. Two variations are expected in this range: one from air to Plexiglas, and one from Plexiglas to sand-water. In Fig. 2.32, only one variation is significantly observed, and the other one, at around 2.3 cm, is very small because the Plexiglas dielectric is very close to air's dielectric.

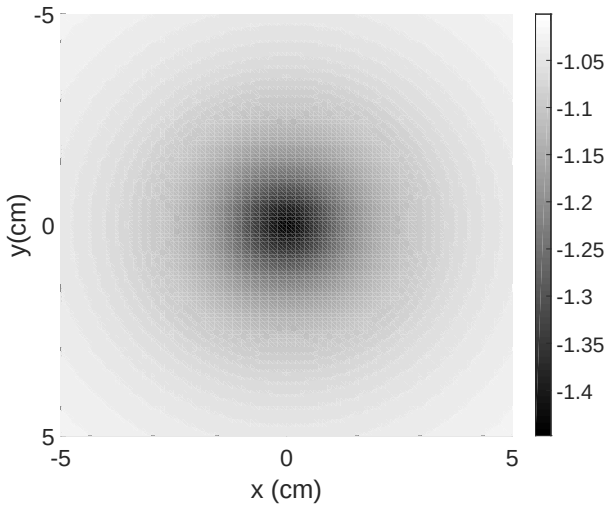


Figure 2.28: Laminogram of the cylinder shown in Fig. 2.23a. No filtering is applied here.

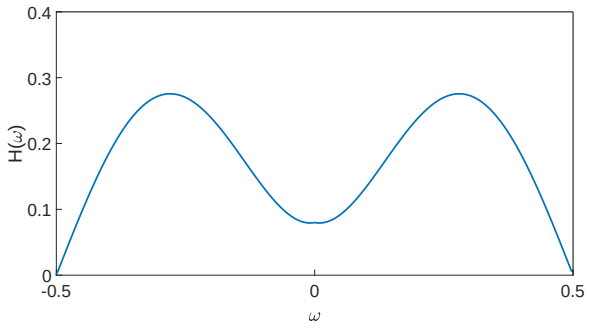


Figure 2.29: Filtering window: a Hamming window multiplied by a ramp filter.

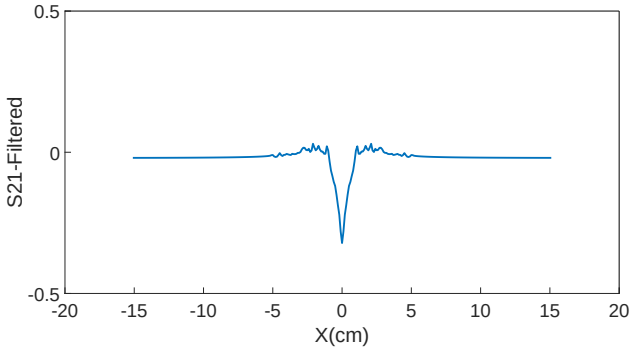


Figure 2.30: Filtered profile of the projection signal padded shown in Fig. 2.27

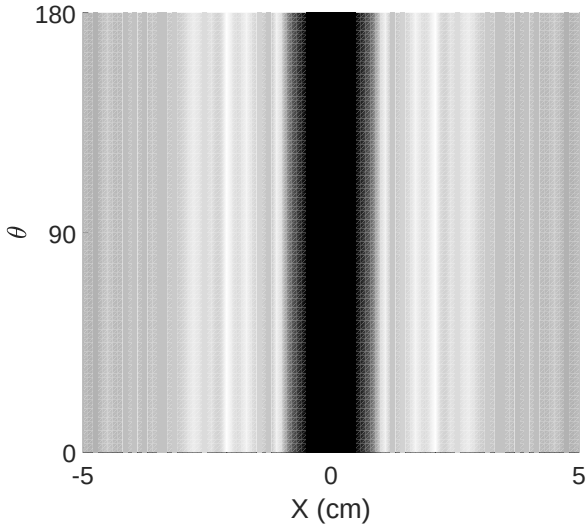


Figure 2.31: Sinogram of the cylinder shown in Fig. 2.23a with filtered data.

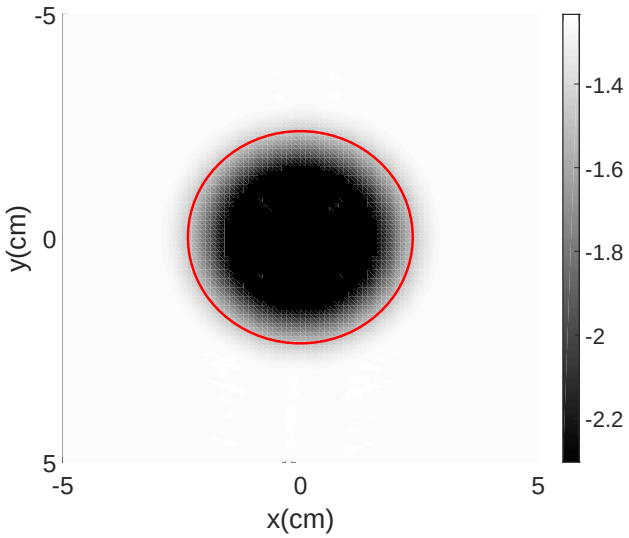


Figure 2.32: Reconstructed image of one slice of the OUT shown in Fig. 2.23a. using filtered projections

Fig. 2.23b shows a four-layer object made up of two Plexiglas cylindrical shells 30 cm in height. The outer shell has an outer radius of 3.2 cm and an inner one of 2.8 cm. The inner shell has an outer radius of 1.9 cm and an inner one of 1.7 cm. The space between these two shells is filled with a mixture of 80% sand and 20% water and the space inside the inner shell is filled with air.

The antennas and the positioner remained unchanged, except for the antenna positions in the X-Y domain, which are adjusted to be 1 mm away from the cylinder. The entire measurement setup and scanning range are similar to that shown in Fig. 2.25, except for the cylinder, which is replaced by the one shown in Fig. 2.23b. The structure is scanned from -5 to 5, and the S21 values are recorded by the receiver, Fig. 2.33. It can be seen that the collected power starts decreasing at around -2.2 cm. The decrease in the power continues up to -0.5 cm at which point the power increases to 0 cm. Two more changes are seen around -2.1 cm and -1.9 cm.

Fig. 2.34 shows the reconstructed image obtained using the profile shown in Fig. 2.33. As seen in Fig. 2.34, there are a few circular layers, but only two of them, highlighted with

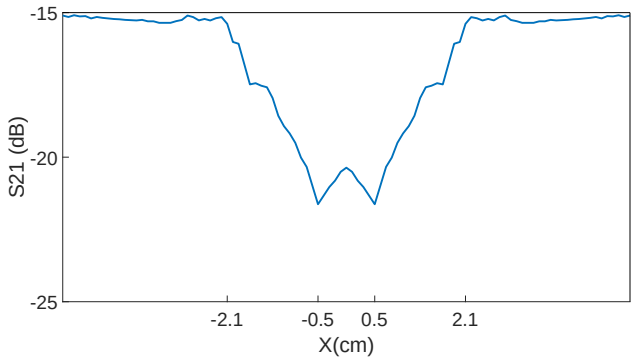


Figure 2.33: The power profile, S21, collected by the receiver as a function of location when the cylinder shown in Fig. 2.23b is scanned between the transmitter and receiver.

red circles, show the major changes. One of these changes represents the transition from the Plexiglas to sand-water and the other one from sand-water to Plexiglas. These major changes happen at around the radius of the shells. Thus, the antennas can capture the electrically small change, less than $\lambda/50$, that happens inside the cylinder.

## 2.6 The Feasibility of Asymmetrical Objects Imaging

The structures tested in this research work were non-homogeneous but symmetrical with respect to the z-axis. The reconstruction algorithm and procedure in this work showed that even electrically small changes can be captured with high-resolution without the need for incorporating any simulation's results or prior information. The images were purely obtained from the measurement data, no optimization algorithm were involved to create the images. Such a reconstruction approach makes microwave imaging to be more practical, less time consuming, and more reliable as it relies purely on analytical approach to create images similar to those utilized in CT.

More complex structures are non-symmetrical and non-homogeneous ones which need to be investigated. An example of such structure can be 2.23a where the cylinder is not centered at the origin 2.35. In such cases a few points need to be emphasized and considered:

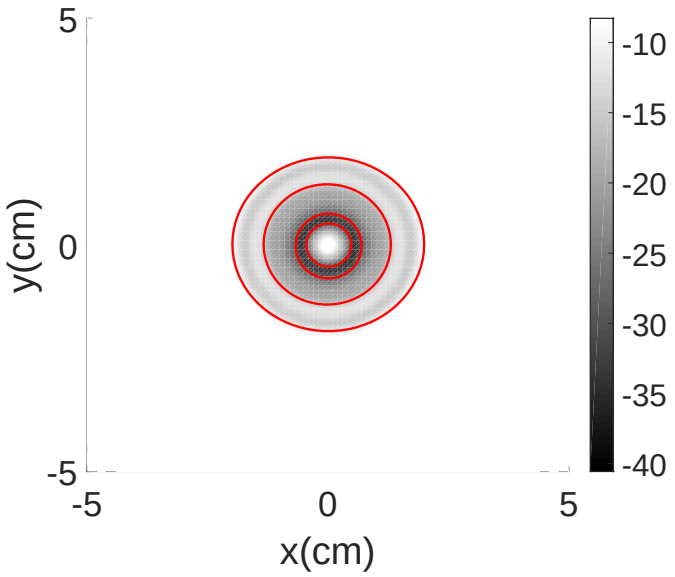


Figure 2.34: Reconstructed image of one slice of the OUT shown in Fig. 2.23b.

1. The whole scanning medium, including the hypothetical red circle shown in 2.35 on which the antennas rotate, need to be electrically small such that the waves packets do not spread and the concept of ray-like behavior still applies.

2. The scanning is better to be done for 360 angle, not only 180, because of the discretization and sampling issue. Although theoretically 180 angle is sufficient; however, not only the structure including the antenna is fully symmetrical, but also the medium has been discretized thus not continuous.

3. The transmitter position is very important as we need the waves packets interact with the object under test before they spread. For example, the result in 2.35a show higher resolution comparing to the one shown in 2.35b. The reason is that, if the hypothetical red circle is not electrically very small then the waves packets spread before reaching the OUT and the receiver.

4. Noise in the system needs to be taken care of very carefully, as the number of measurements might be very large and any noise may generate artifacts.

5. The cables connected to the transmitter and receiver must be isolated such that not

only they do not radiate but also they do not disturb the geometry of the whole structure.

6. Increasing the whole scanning environment require the antennas to become electrically smaller.

## 2.7 Conclusion

This chapter presented a novel high-resolution image reconstruction method based on the Radon transform and near-field excitation. Both experimental and simulation results prove that electrically-small antennas can detect quite small changes with a sharp resolution. Simulation studies showed that the high image resolution is due to the reduction in the coupling between layers, which causes the waves to interact mainly with the layer placed directly between the transmitter and receiver. This phenomenon resembles the ray illuminations in computerized tomography. Therefore, Radon transform can be used to effectively reconstruct the object in this case. The findings in this paper proves that if the transmitter and receivers are electrically small, and placed in close proximity to the object under test, the image resolution of the image can be enhanced to less than $\lambda/50$.

The technique presented in this paper is computationally inexpensive and uses only the amplitude information of the transmitted waves from the OUT to reconstruct the image. The results of this, using electrically small antennas and Radon transform, suggest a promising future in high resolution imaging, especially for medical applications.

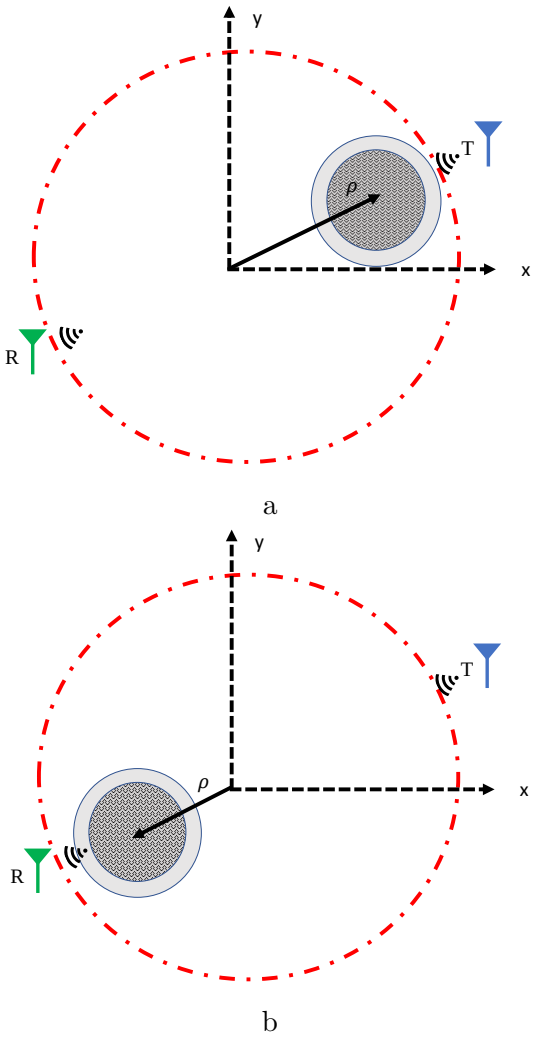


Figure 2.35: Top view of an asymmetrical structure when a non-homogeneous cylinder is located at a distance of $\rho$ from the origin

# Chapter 3

# Material Characterization

## 3.1 Introduction

This chapter presents a permittivity characterization method based on the transmitted power measurement in the microwave regime. The introduced method can retrieve the dielectric properties of materials utilizing multi-objective functions enforced at multiple frequencies without the need for phase information which requires expensive measurement setup. Therefore, a signal generator and a power-meter are enough to retrieve the permittivity of materials. To validate the method numerically, two structures including free space and a coaxial line are used. For experimental verification, a coaxial line is designed and fabricated to retrieve the dielectric properties of several high loss liquids. The method will be expanded to multi-layer permittivity reconstruction using optimization and heuristic algorithms.

## 3.2 Theoretical Foundation of The Method

This section explains the theoretical foundation of the permittivity reconstruction method. Fig. 3.1 shows an infinite dielectric slab with a thickness d excited by a plane wave with the propagation vector in the z-direction. To find the wave solution, the space is divided

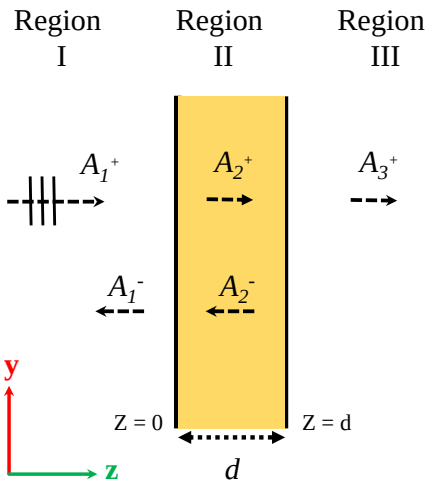


Figure 3.1: An infinite slab with finite thickness d in the presence of a plane wave incidence with the amplitude of $A_1^+$. Regions I and III are the free space whereas region II is filled with a dielectric with $\epsilon_r$ permittivity.

into three regions: regions I and III are free space, and region II is an infinite dielectric slab with complex permittivity of $\epsilon_r = \epsilon_r - j\epsilon_r''$. The objective is to determine the complex permittivity of medium II using the power in region III. The incident field is linearly polarized in the x-direction and has an electric field amplitude of $A_1^+$. Due to the incident field, multiple reflections and transmissions occur. Therefore, the electric and magnetic fields in each medium are as follows:

$$\mathbf{E_1} = (A_1^+ e^{-j\beta_0 z} + A_1^- e^{j\beta_0 z})\hat{a_x} \tag{3.1}$$

$$\mathbf{H_1} = (\frac{A_1^+}{\eta_0} e^{-j\beta_0 z} - \frac{A_1^-}{\eta_0} e^{j\beta_0 z})\hat{a_y} \tag{3.2}$$

$$\mathbf{E_2} = (A_2^+ e^{-j\gamma z} + A_2^- e^{j\gamma z})\hat{a_x} \tag{3.3}$$

$$\mathbf{H_2} = (\frac{A_2^+}{\eta} e^{-j\gamma z} - \frac{A_2^-}{\eta} e^{j\gamma z})\hat{a_y} \tag{3.4}$$

$$\mathbf{E_3} = A_3^+ e^{-j\beta_0(z-d)}\hat{a_x} \tag{3.5}$$

$$\mathbf{H_3} = \frac{A_3^+}{\eta_0} e^{-j\beta_0(z-d)}\hat{a_y} \tag{3.6}$$

where $A_1^-$ is the backward wave amplitude in medium I; $A_2^+$ and $A_2^-$ are forward and backward waves amplitudes in medium II; respectively, and $A_3^+$ is the forward (or transmitted) wave amplitude in medium III. Notice that there is no reflected wave in region III as it is infinite.

In (3.1)-(3.6), $A_1^+$ is known whereas $A_1^-$, $A_2^+$, $A_2^-$, and $A_3^+$ are unknowns. $\beta_0 = \omega\sqrt{\mu_0\epsilon_0}$ and $\eta_0 = \sqrt{\mu_0/\epsilon_0}$ are the propagation constant and characteristic impedance of regions I and III, respectively. $\gamma = \omega\sqrt{\mu\epsilon}$ and $\eta = \sqrt{\mu/\epsilon}$ are the complex propagation constant and characteristic impedance of medium II. $\epsilon = \epsilon_0\epsilon_r$ and $\mu$ is set to $\mu_0$ to limit the analysis to non-magnetic materials only.

By enforcing the boundary conditions on the field components at the interfaces, all the four unknowns can be found. Consequently, the real time-averaged in region III is given by

$$\hat{P}_{out}(f_i, \epsilon_r', \epsilon_r'') = \frac{8\left|A_1^+\eta_0\eta e^{j\gamma d}\right|^2}{\eta_0\left|(\eta_0+\eta)^2 e^{2j\gamma d} - (\eta_0-\eta)^2\right|^2} \tag{3.7}$$

$\hat{P}_{out}$ is the transmitted power at the excitation frequency of $f_i$. The only unknown is the complex dielectric constant of the slab which appears in $\gamma$ and $\eta$. Thus our objective is to determine the real and imaginary parts of the dielectric permittivity by measuring the real power in region III.

The unknowns in (3.7) are $\epsilon_r'$ and $\epsilon_r''$; therefore, at least two equations are needed to solve for the two unknowns. These equations can be generated by evaluating the difference between the real value of the measured transmitted power and the analytically calculated power in region III at different frequencies. This difference, designated as $\delta$ is expressed as

$$\delta(f_i, \epsilon_r', \epsilon_r'') = \left|P_{out}(f_i) - \hat{P}_{out}(f_i, \epsilon_r', \epsilon_r'')\right| \tag{3.8}$$

where $P_{out}(f_i)$ is the measured power. An analytical solution for (3.8) is not available because of its nonlinear and complex nature, particularly for lossy materials [90]. To this end, we employ a root-searching algorithm involving the use of multi-objective functions and the least mean square method (LMS). The process starts with searching for the solution in a three-dimensional rectangular grid space. The first two dimensions include the possible values of $\epsilon_r'$ and $\epsilon_r''$, and the third dimension includes the calculated value of $\delta$ obtained from (3.8) for each pair of ($\epsilon_r'$, $\epsilon_r''$) at the excitation frequency $f_i$. In this paper, $\epsilon_r'$ is discretized with a step of 0.1, whereas $\epsilon_r''$ is discretized with a step of 0.001. The search domain is between 1 and 120 for $\epsilon_r'$ and -10 and 0, for $\epsilon_r''$. If the material under test is highly lossy, its imaginary part may be lower than -10. In such cases, the search region needs to be expanded so that it encompasses the imaginary part of these materials.

Since the dielectric responses of materials as a function of frequency change slowly over a narrow band, except for the cases wherein anomalous dispersion may occur, the method presented here assumes that the material under test has nearly constant dielectric permittivity over the narrow range of frequency at which the measurements are performed. Therefore, by evaluating (3.8) at multiple frequencies, independent equations can be obtained. Consequently, several rectangular grids of $\delta(f_i, \epsilon_r', \epsilon_r'')$ can be created at multiple of frequencies. To find $\epsilon_r'$ and $\epsilon_r''$ at least two grids of $\delta$ at $f_1$ and $f_2$ are required. The locations that return $\delta = 0$ are the possible solutions. However, the condition $\delta = 0$ requires $P_{out}$ to be exactly the same value as the analytical one. Satisfying this condition is difficult because of the errors arising from noise in the measurements. If $\delta \neq 0$, the searching process might return more than one solution. The problem of multiple solutions might happen even if $\delta = 0$ because of the non-linear nature of (3.7).

To overcome the multiple solutions problem, we increase the number of independent equations by evaluating (3.8) at M different frequencies. Notice that the difference between the least frequency, $f_{min}$, and the highest frequency, $f_{max}$ is considered to be small to assure that the complex permittivity is constant within this frequency range.

It is important to emphasize that the use of multiple frequencies is completely different from a curve fitting process. In the curve fitting process, the goal is to find the best possible curve that matches a series of data points. However, here, at each frequency, a new equation is generated that contains new information. Then all the generated equations

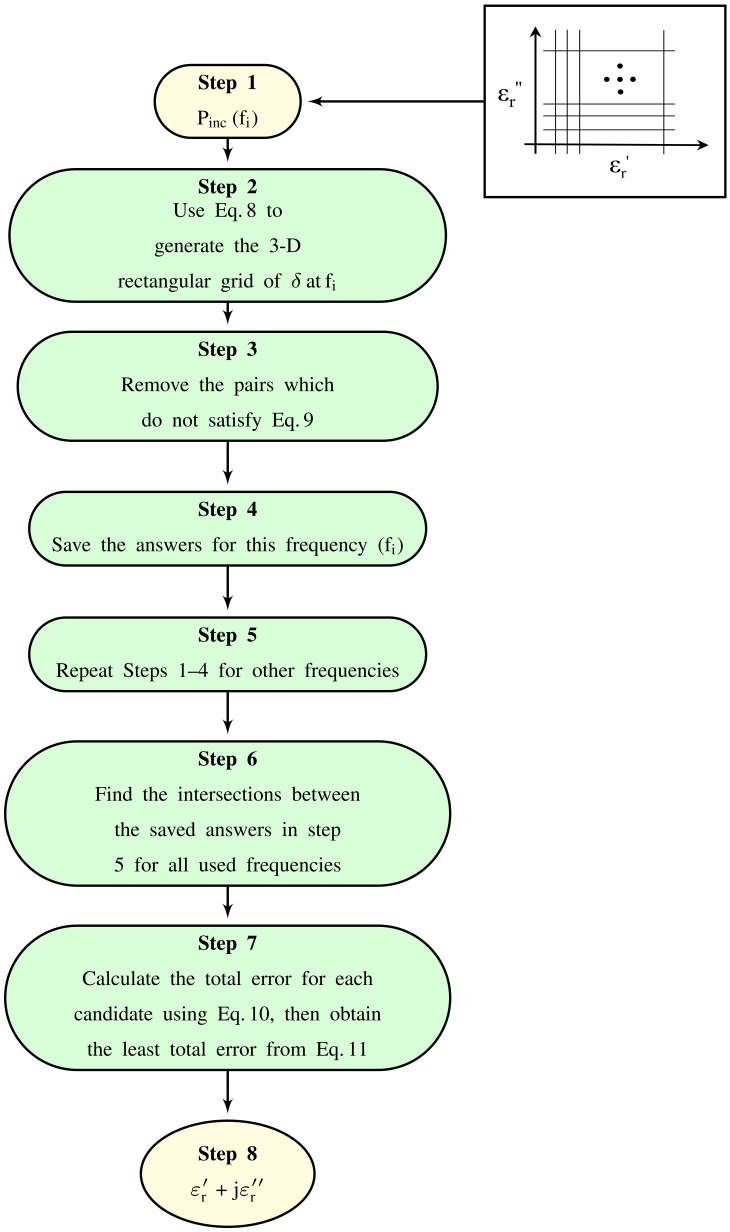


Figure 3.2: Flow chart for the dielectric reconstruction procedure when $E_{input}(f_i)$ is exciting the structure, Fig. 3.1. The rectangular grid of $\epsilon'_r$ and $\epsilon''_r$ shows the search space.

are solved simultaneously to return one solution. This procedure is based on the change in the input impedance of the slab as the frequency varies.

Next, at each frequency (for a total of M frequencies), $\delta$ is calculated using (3.8) for all possible combinations of $\epsilon_r'$ and $\epsilon_r''$ within the defined range. Therefore, M grids are generated. Then, a root-searching algorithm is exploited to find the solution. Since, as mentioned earlier, reaching $\delta = 0$ is very difficult in practice, it is necessary to define a specific margin, $\Delta$. Therefore, instead of $\delta = 0$, we specify that every single possible candidate must satisfy the following inequality:

$$\delta(f_i, \epsilon_r', \epsilon_r'') < \Delta \tag{3.9}$$

Therefore, for each pair of $\epsilon_r'$ and $\epsilon_r''$ at each frequency of $f_i$, if the criterion given by (3.9) is met, this pair remains in the pool of possible solutions, otherwise the pair is removed. This process is done for all possible pairs of $(\epsilon_r', \epsilon_r'')$ at all M frequencies. Then, the intersection between all possible answers represents the final solution.

The algorithm might return N solutions that all satisfy (3.9) at all chosen frequencies. To resolve this problem, the least mean square (LMS) algorithm given by the following equation is used:

$$\delta_{Tn}(\epsilon_r', \epsilon_r'') = \frac{1}{MP_{inc}} \sqrt{\sum_{i=1}^{M} \delta(f_i, \epsilon_r', \epsilon_r'')^2} \tag{3.10}$$

where $\delta_{Tn}$ is the relative total averaged error of each cell with respect to the incident power, $P_{inc}$, which is given by

$$P_{inc} = \frac{\left|A_1^+\right|^2}{2\eta_0}$$

The last step is to search for the candidate which returns the least total error, $\delta_{min}$, which is calculated as follows:

$$\delta_{min} = min(\delta_{T1}, \delta_{T2}, ..., \delta_{TN}) \tag{3.11}$$

The use of multiple samples at different frequencies along with the LMS algorithm, decreases the dependency of final solution on the measurements' accuracy.

The reconstruction process is outlined in the flowchart shown in Fig. 3.2. The process has seven steps as follows:

1. A two-dimensional search space (rectangular grid) is built in which the dimensions represent $\epsilon_r'$ and $\epsilon_r''$. Then, the slab is illuminated by an incident wave with $P_{inc}$ power at a specific frequency $f_i$.

2. The built grid from the first step expanded to three-dimensions by calculating $\delta$ at each pair of ($\epsilon_r'$, $\epsilon_r''$) with the use of (3.8).

3. The root-searching algorithm is applied to find and remove those combinations of ($\epsilon_r'$, $\epsilon_r''$) that return $\delta > \Delta$.

4. The answers, which are the combination of real and imaginary parts that satisfied $\delta < \Delta$ are saved.

5. The steps from 1 to 4 are repeated for all M frequencies.

6. The intersections between all of the solutions is found.

7. The LMS algorithm is applied to the N solutions to find the answer that has the least error.

## 3.3 Simulation Results

To validate the reconstruction technique presented in this paper, two transmission based structures including an infinite dielectric slab and a coaxial line are used. The first one uses the power method (PM) applied to the free space setup, henceforth referred to as PM-FS, and the second one uses the power method applied to a coaxial line, henceforth referred to as PM-CL. An infinitely wide dielectric slab with a thickness of $d = 150$ mm is considered with a lossy dielectric of $\epsilon_r = 5.0 - j0.025$, which is to be measured. The

Table 3.1: Reconstructed Dielectric for different materials using the PM-FS.

| Exact Permittivity | Calculated Permittivity |
|---|---|
| $\epsilon_r = 2 - j0.010$ | $\epsilon_r = 2.0 - j0.010$ |
| $\epsilon_r = 5 - j0.065$ | $\epsilon_r = 5.0 - j0.065$ |
| $\epsilon_r = 9 - j1.130$ | $\epsilon_r = 9.0 - j1.130$ |
| $\epsilon_r = 13 - j5.370$ | $\epsilon_r = 13.0 - j5.370$ |
| $\epsilon_r = 15 - j3.055$ | $\epsilon_r = 15.0 - j3.055$ |
| $\epsilon_r = 20 - j7.040$ | $\epsilon_r = 19.9 - j7.045$ |

model is excited by a plane wave with the electric field amplitude of $A_1^+ = 10$ V/m and a propagation constant in the positive z-direction. The excitation frequency of the plane wave is between 100 MHz and 1 GHz. Fig. 3.1 shows the structure modeled using the numerical simulation package CST MICROWAVE STUDIO [91].

To collect the power, a probe is placed at the interface between regions II and III. Once the simulation is accomplished, twenty samples of recorded power at twenty frequencies from 300 MHz to 490 MHz in 10 MHz steps are chosen. In the next step, to create the three-dimensional error space, $\delta$, discretization is done for $\epsilon_r'$ and $\epsilon_r''$ with the steps and the ranges explained in the prevous section. Then, using (3.7), the $\delta$ value of each cell is calculated by (3.8). The margin value of $\Delta$ is set to 10 here where the input power is 0.27 W. This $\Delta$ value can be bigger or smaller depending on the input power. Finally, the dielectric constant is reconstructed based on the proposed algorithm. In this simulation, the dielectric constant of the slab with $\epsilon_r = 5.0 - j0.025$ is retrieved with an accuracy of 100%. Table 3.1 shows the reconstruction results for the slab made of several other materials with different dielectric constants. It is observed that the reconstructed permittivity values are highly accurate. However, 100% may not be achieved because the slab cannot be infinitely wide in practice.

To visualize the importance of utilizing multiple frequencies, the intensity of relative error, $\delta_T$, for the infinite slab with $\epsilon_r = 5 - j0.025$ and the thickness of 150 mm is shown in Fig. 3.3. The first two dimensions contain $\epsilon_r'$ and $\epsilon_r''$ whereas the third dimension, showing the values of $\delta_T$ (related to each $(\epsilon_r', \epsilon_r'')$) is represented by color.

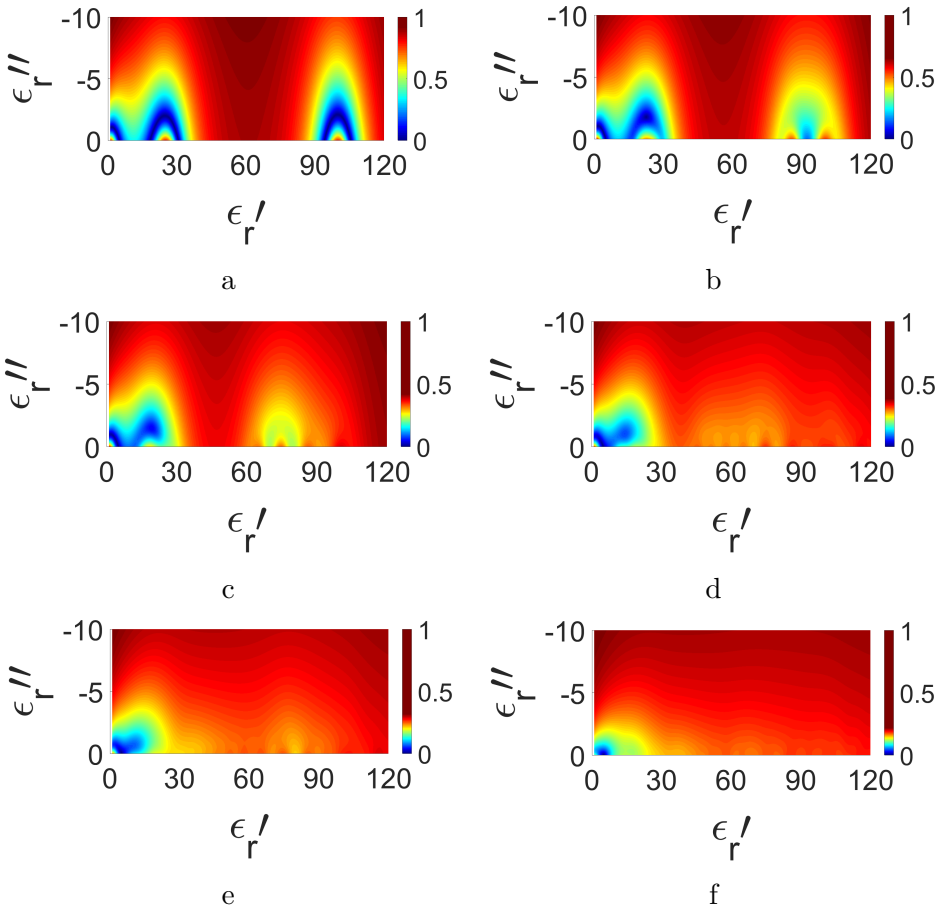


Figure 3.3: The intensity of $\delta_T$ values using the PM-FS over a region of $\epsilon'$ and $\epsilon''$, when a dielectric slab with $\epsilon_r = 5 - j0.025$ and the thickness of 150 mm used for a different number of samples at different frequencies: a. One frequency, 300 MHz b. Two frequencies, 300 and 350 MHz c. Four frequencies, 300, 350, 400 and 450 MHz d. Seven frequencies, 300 to 490 MHz with the step of 30 MHz e. Ten frequencies, 300 to 490 MHz equally divided into 10 steps and f. Twenty frequencies, 300 to 490 MHz equally divided into 20 steps.

Fig. 3.3(a)-(f) show the intensity of $\delta_T$ values when different number of power samples at frequencies ranging from 300 to 490 MHz are used. In Fig. 3.3(a) only one sample of power, at 300 MHz, is used. It can be seen that the number of solution candidates which have lower values of $\delta_T$ and are shown by the blue color spread over a wide region. In the next attempt, when the number of samples is increased to two, at the frequencies of 300 and 350 MHz, the regions of solutions (blue color) decreased, as shown in Fig. 3.3(b). Fig. 3.3(c) shows $\delta_T$ when four samples are used at 300, 350, 400, and 450 MHz. Fig. 3.3(d) is plotted when seven frequencies from 300 to 490 MHz are used with a step of 30 MHz. In Fig. 3.3(e) ten samples are used at frequencies from 300 to 490 MHz, with a step of $21.\bar{1}$ MHz. And Fig. 3.3(f) shows the case when twenty samples are considered at the frequencies from 300 to 490 MHz with a step of 10 MHz. It can be seen from Fig. 3.3(a)-(f) that the region with blue color that represents low $\delta_T$ has shrunk comparatively to a very small area in the bottom corner of the figure, thus indicating more accurate prediction for the complex permittivity of the material. Although the region of possible solutions is significantly decreased, still there are N possible solutions. To find the final answer among these N candidates, the LMS algorithm explained in section II is used and the candidate that returns $\delta_{min}$ is considered as the final answer. In this case, the value for the permittivity of the slab is found precisely, which is $5.0 - j0.025$.

To investigate the effect of different bandwidths, the same slab is excited at different frequencies. Fig. 3.4(a)-(f) show the intensity of $\delta_T$ values when different bandwidths are used to determine the permittivity of the slab with the frequency center of 400 MHz and twenty power samples. The samples are uniformly selected in any given bandwidth. The bandwidths are 10, 30, 50, 100, 190, and 400 MHz for Fig. 3.4(a) to Fig. 3.4(f), respectively. It is seen that increasing the bandwidth reduces the region of solution and ultimately the results converge to the correct solution. Fig. 3.5(a) and (b) show the error percentage as a function of bandwidth for both the real and imaginary parts of this slab.

To investigate the effects of measurements/simulations noise on the retrieved permittivity, a Monte Carlo experiment is conducted on the slab excited with the same plane wave with a power density values of 0.27 W/$m^2$, case I, and 0.4 W/$m^2$, case II. A uniform noise is added to the power density values obtained from simulations, considering that 10 power samples were used to retrieve the permittivity. The noise amplitude changed from 0 to 0.1

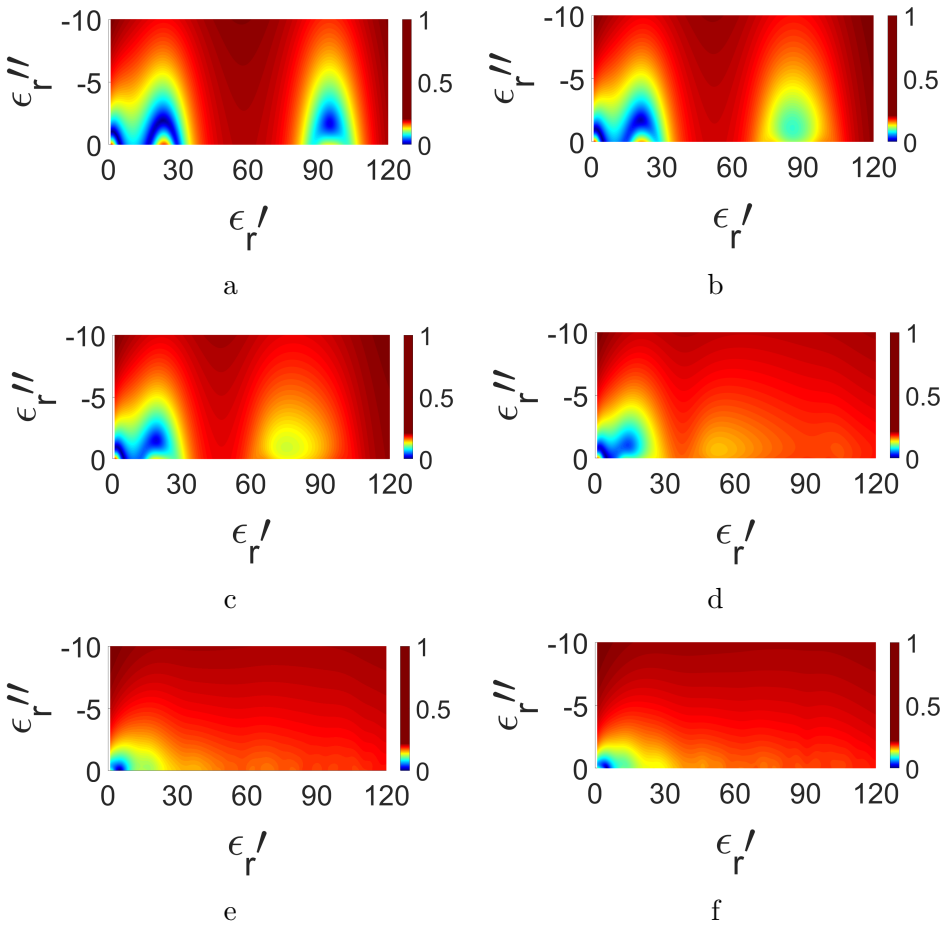


Figure 3.4: The intensity of $\delta_T$ values using the PM-FS over a region of $\epsilon_r'$ and $\epsilon_r''$, where a dielectric slab with $\epsilon_r = 5 - j0.025$ and the thickness of 150 mm is tested at different frequency bands when 20 samples are used linearly: a. (395-405) MHz, b. (385-415) MHz c.(375-425) MHz d. (350-450) MHz and e. (300-490) MHz and f. (200-600) MHz.

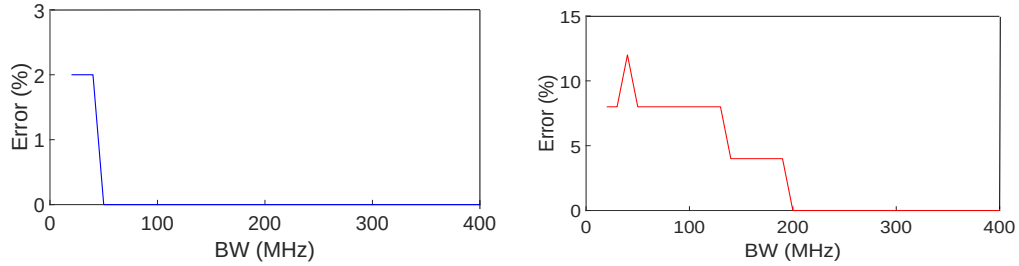


a b

Figure 3.5: Reconstructed permittivity error evaluation as a function of bandwidth for a slab with a length of 150 mm and permittivity of $5 - j0.025$ when the frequency center is 400 MHz: a. real part b. imaginary part

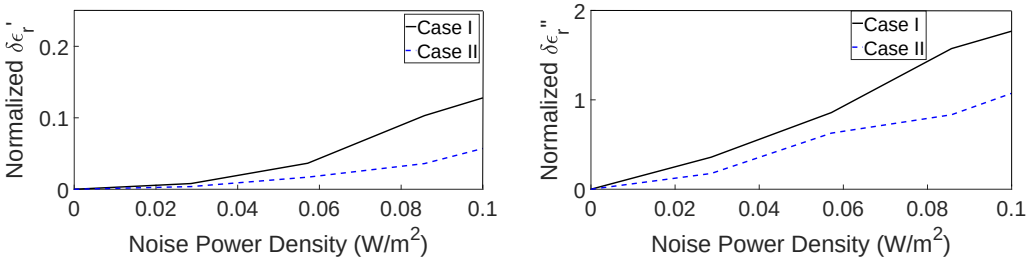


a b

Figure 3.6: Normalized error between the actual permittivity and the one obtained from the noisy measurements. (a) Error in the real part. (b) Error in the imaginary part.

W/$m^2$ for which the retrieved permittivity was averaged over 800. The retrieved permittivity in the presence of noise was then compared with the actual permittivity. Fig. 3.6 shows the normalized error in the real and imaginary parts of the retrieved permittivity as a function of the noise amplitude power density (normalization was carried out with respect to the assumed correct value for the permittivity). These results show that the imaginary part of the permittivity is more sensitive to noise, comparing to the real part. For example, when the excessive noise reaches 10% of the input power density in Case I, the real part reconstructions error becomes %0.35 while the imaginary parts error becomes %16.5. Additionally, the sensitivity decreases as the input power increases.

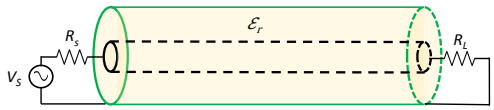


Figure 3.7: The setup configuration for a coaxial line with source impedance and output load. The coaxial cable has the characteristic impedance of Z.

As a second verification for the proposed permittivity reconstruction method, a coaxial line structure is considered, Fig. 3.7, when it is filled with the material that is going to be measured, the PM-CL. According to the transmission line theory, the propagation constant and characteristic impedance of the coaxial line are

$$\gamma = \alpha + j\beta = \sqrt{(R + j\omega L)(G + j\omega C)}$$

$$Z = \sqrt{\frac{R + j\omega L}{G + j\omega C}}$$

where $\omega$ is the angular frequency; R and L are the per unit resistance and the inductance of the line, respectively; G and C are the per unit conductivity and the capacitance of the line, which are functions of $\epsilon_r'$ and $\epsilon_r''$; and Z is the characteristic impedance of the coaxial line. The real power calculated at the load can be expressed as

$$\hat{P}_L(f_i, \epsilon_r', \epsilon_r'') = \frac{1}{2R_L}\left|\frac{V_s Z_{in} e^{-\gamma d}(\Gamma + 1)}{(R_s + Z_{in})(\Gamma e^{-2\gamma d} + 1)}\right|^2 \tag{3.12}$$

where $\Gamma$ is the reflection coefficient from the load. $\gamma$, $R_L$, $R_s$, and $V_s$ are the propagation constant, load resistance, source resistance, and source voltage, respectively. Therefore $Z_{in}$, which is the input impedance of the coaxial line model, including the line and the load resistance, can be expressed as

$$Z_{in} = Z\frac{R_L + Ztanh(\gamma d)}{Z + R_L tanh(\gamma d)} \tag{3.13}$$

Table 3.2: Reconstructed Dielectrics of different materials filling in the coaxial cable shown in Fig. 3.7 using the PM-CL.

| Exact Permittivity | Calculated Permittivity |
|---|---|
| $\epsilon_r = 3 - j0.215$ | $\epsilon_r = 3 - j0.215$ |
| $\epsilon_r = 7 - j0.015$ | $\epsilon_r = 7 - j0.015$ |
| $\epsilon_r = 13 - j0.450$ | $\epsilon_r = 13 - j0.450$ |
| $\epsilon_r = 15 - j0.025$ | $\epsilon_r = 14.9 - j0.020$ |
| $\epsilon_r = 20 - j1.500$ | $\epsilon_r = 19.9 - j1.400$ |

In the reconstruction process using the coaxial line, the $\delta$ expression introduced in (3.8) needs to be modified as the following

$$\delta(f_i, \epsilon_r', \epsilon_r'') = \left| P_L(f_i) - \hat{P}_L(f_i, \epsilon_r', \epsilon_r'') \right| \tag{3.14}$$

where $P_L(f_i)$ is the measured power at $f_i$ and $\hat{P}_L(f_i, \epsilon_r', \epsilon_r'')$ is calculated from (3.12). The reason is that the analytical value of power for an infinite dielectric slab is different from that of a coaxial line.

To implement the reconstruction process explained in the previous section, but with a coaxial model, a 10 mm line shown in Fig. 3.7 is designed in the stimulation environment and filled with the materials presented in Table 3.2. The model is excited using a sinusoidal voltage with an amplitude of $A_1^+ = 1$ V/m. The structure is then simulated at frequencies between 100 and 290 MHz. The real values of power are calculated across a 50 $\Omega$ load impedance. To reconstruct the dielectric constant of the material, twenty samples of power from 100 to 290 MHz with a step of 10 MHz are used. After applying the procedure explained in the previous section, the reconstructed results are shown in Table 3.2. In this case the input power is 0 dBm and the $\Delta$ was set to 1.

## 3.4 Experimental Measurement

A coaxial line structure is designed to experimentally verify the permittivity reconstruction process proposed in this paper. Fig. 3.8 shows this coaxial line setup. The outer radius of the coaxial line is 4.1 mm and the inner is 1.27 mm. The inner conductor is created by inserting one 1.8 cm connector anteriorly and another posteriorly both with 50 Ω impedances, which results in creating a coaxial line with 3.6 cm length. The space between the inner and outer is filled with the material under test. (This setup is more suitable for liquids, however, we have also tested solids such as Polytetrafluoroethylene (PTFE)). Fig. 3.8(b) shows the top-view of the manufactured coaxial line.

Fig. 3.9 shows the measurement setup including a spectrum analyzer, the coaxial line structure, and a signal generator. The signal generator sends a single frequency signal with a power level of 0 dBm. The spectrum analyzer is set to have a residual bandwidth of 1 kHz and a measurement bandwidth of 20 MHz. The measurement was done for frequencies between 100 and 290 MHz, with a step of 10 MHz.

The procedure of filling the structure with different materials is as follows: first, one of the connectors is tightened in place using four screws. Then, the coaxial line is held by a stand shown in Fig. 3.10. Thereafter, the hole is filled with the desired material and the other connector is inserted and tightened into place, sealing the device. The setup is now ready for measurement. Please note that all the measurements are done at room temperature. The output power when the line is filled with ethanol is plotted in Fig. 3.11 for frequencies between 100 and 300 MHz.

The reconstruction method is then applied using (3.14) to find the $(\epsilon_r', \epsilon_r'')$ pair that returns back the power values match to those shown in Fig. 3.11. The number of power samples used to reconstruct the MUTs are twenty at frequencies from 100 to 290 MHz with a step of 10 MHz. Table 3.3 also represents the reconstructed dielectric values for PTFE, pure Ethanol, and other liquids.

Table 3.3 also verfies the permittivity values obtained using the proposed method in this paper and what reported in the literature as well as the open-ended coaxial method. As seen in this table, the reconstructed permittivity values of different liquids obtained

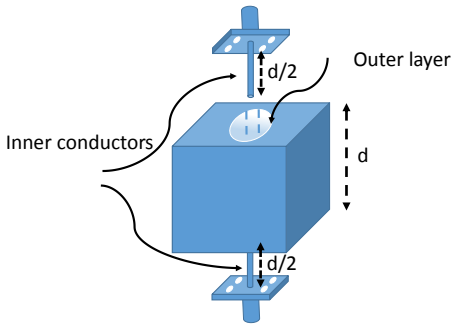


a

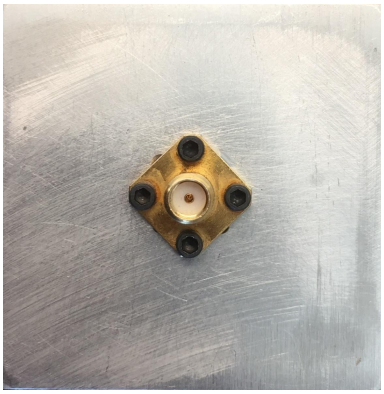

b

Figure 3.8: A coaxial line used to measure the permittivity of liquids. (a) An aluminum cube with a 3.6 cm deep hole as the outer layer with two 50 Ω connectors as the inners, each is 1.8 cm long. (b) Top view of the fabricated coaxial line filled with a MUT.

by the method presented here are in close agreement with the reported values in the literature [92–94]. This implies that the algorithm works efficiently without having any knowledge of the material under test.

As discussed in the introduction, there are a few reports available in the literature on the permittivity retrieval techniques that only use amplitudes of reflection or transmission. Table 3.4 compares some of the most common amplitude-only methods. It can be seen that our method, PM, does not need a VNA for the measurements because only the transmitted power is needed. In addition, our method does not require any prior knowledge about the material under test, which makes it applicable to low-loss, medium-loss, and high-loss

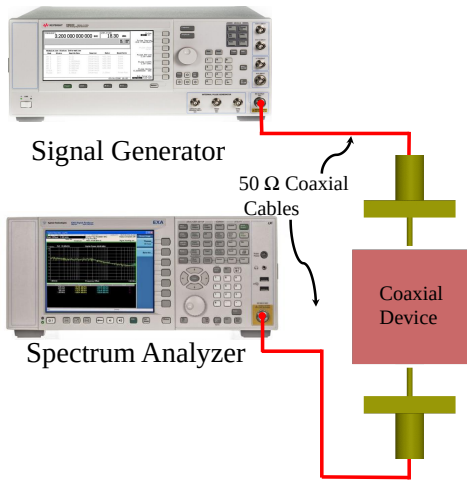


Figure 3.9: The measurement setup includes a coaxial line filled with PTFE, a signal generator and a spectrum analyzer.

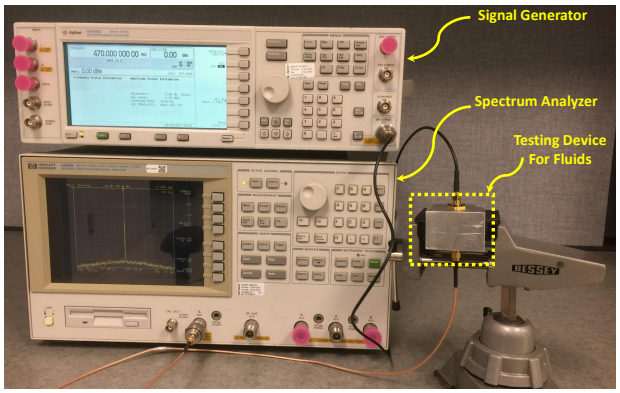


Figure 3.10: The coaxial line structure connected to a signal generator and spectrum analyzer using two 50Ω cables.

materials. However, a limitation of our method is the retrieval of the permittivity for highly dispersive media.

As a further verification, we compared our method with the open-ended coaxial method (OECM) for the liquids reported in Table 3.3. The measurement setup for the OECM is

Table 3.3: Reconstructed Dielectric value of different materials in three cases: first, measuring the liquid-filled coaxial device using the PM-CL (Fig. 3.10); second, literature; third, Open-ended coaxial method. For the frequency centered at 200MHz.

| Material Name | Coaxial Structure | Literature | Open-ended |
|---|---|---|---|
| PTFE | $\epsilon_r = 2.0 - j0.07$ | $\epsilon_r = 2.0 - j0.01$ | N.A. |
| Cyclohexane | $\epsilon_r = 1.9 - j0.06$ | $\epsilon_r = 2.015 - j0.002$ | $\epsilon_r = 2.58 - j0.01$ |
| Chloroform | $\epsilon_r = 4.2 - j0.18$ | $\epsilon_r = 4.7 - j0.12$ | $\epsilon_r = 5.56 - j0.04$ |
| Dichloromethane | $\epsilon_r = 8.1 - j0.10$ | N.A. | $\epsilon_r = 9.70 - j0.12$ |
| Pure Ethanol | $\epsilon_r = 25.2 - j3.67$ | $\epsilon_r = 23.61.85 - j3.97$ | $\epsilon_r = 24.85 - j4.11$ |

Table 3.4: Comparison between permittivity reconstruction methods.

| Method | PM | [83] | [81] | [84] | [80] |
|---|---|---|---|---|---|
| Prior Information | No | Yes | Yes | Yes | Yes |
| S11 | No | Yes | Yes | No | Yes |
| S21 | Yes | Yes | Yes | Yes | Yes |
| VNA Requirenment | No | Yes | Yes | No | Yes |
| Low-loss | ✓ | No | No | No | No |
| Medium-loss | ✓ | ✓ | ✓ | No | ✓ |
| High-loss | ✓ | ✓ | ✓ | ✓ | ✓ |
| Accuracy Level | High | High | Medium | Medium | High |

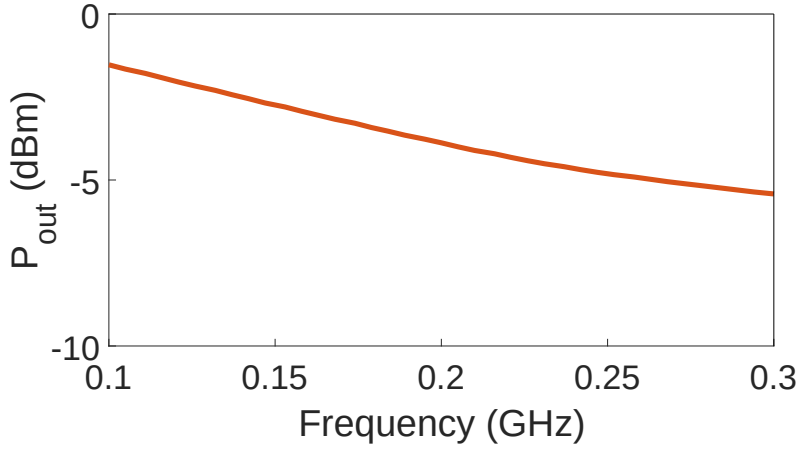


Figure 3.11: The output power for the coaxial cable shown in Fig. 3.10 filled with pure Ethanol. The injected power is $0dBm$ and the frequency range is from 100 and 300MHz.

shown in 3.12. As seen in Table 3.3, the reconstructed permittivity values of different liquids obtained by the method presented here differ from those obtained by the OECM, the details of these differences will be investigated in the discussion section.

## 3.5 Discussion

As seen in Table 3.3, the reconstructed permittivity values for different liquids obtained by the presented method in this paper differ from those obtained by the open-ended coaxial line method. To investigate the accuracy of these two methods, two liquids, Dichloromethane and Chloroform, were studied. The procedure to test the accuracy of the methods is as follows: First, the PM-CL and the OECM methods are used to determine the dielectric constant of the liquid as $\epsilon_r^{(1)}$ and $\epsilon_r^{(2)}$, respectively. Next, the output power is plotted as a function of frequency for $\epsilon_r^{(1)}$ and $\epsilon_r^{(2)}$ using the analytic power formula derived for the coaxial transmission line, (12). Then the power obtained experimentally is plotted on the same figure. Fig. 3.13(a) shows the three curves for Dichloromethane. The agreement between the analytic power obtained using $\epsilon_r^{(1)}$ and the experimental results indicates that the PM-CL provides higher accuracy than the OECM at this measured range

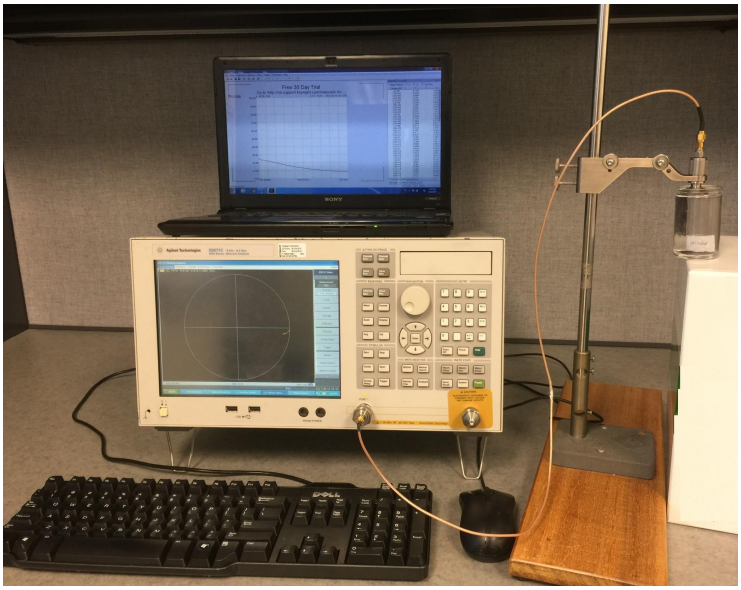

Figure 3.12: Dielectric measurements for different liquids using the OECM.

of frequency. Fig. 3.13(b) which shows the results for Chloroform further indicates the higher accuracy of the PM-CL. The maximum relative deviation from the analytical solution for the OECM is approximately 10.8% whereas the PM-CL yields an error of 0.55% when Dichloromethane liquid is under test. Also, the maximum relative deviation for the OECM is roughly 2% whereas the PM-CL return 0.29% when Chloroform is under test.

It is important to note that when using the OECM, two assumptions are made which compromise the accuracy. First, the method is based on an approximated field distribution in the proximity of the open end of the line. Second, it is assumed that the material under test is infinite, which neglects the reflections coming back from the bottom of the liquid container and surrounding medium. However, in the method presented in this work, there is no need for large liquid sample. In fact, in the measurements provided in this paper, only 1.72 $cm^3$ of liquid was sufficient. In addition, since the coaxial line supports a TEM mode, the fields can be modeled analytically for frequencies lower than the cut-off frequency of the coaxial structure with no approximations. Besides, the reflections from the medium is completely shielded by the coaxial line. Therefore, as presented in Fig. 3.13(a) and (b), the PM shows a higher accuracy at the measured frequencies when a coaxial line (CL) is

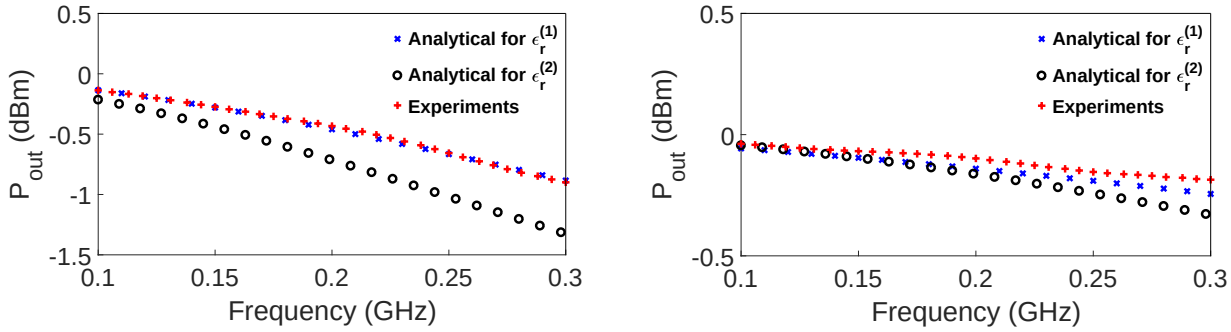


Figure 3.13: Output power results obtained from the analytical formula of the coaxial line and the experiments for (a) Dichloromethane and (b) Chloroform. The lines marked with 'x' show the calculated analytical power versus frequency when $\epsilon_r^{(1)}$s is used in (12). The lines marked with 'o' show the calculated analytical power when $\epsilon_r^{(2)}$s are submitted in (12). The lines marked with '+' show the output power values obtained from the measurement of these liquids.

used than that of the OECM. However, the OECM operates at a wider range of frequency comparing to the coaxial line structure.

## 3.6 Multi-layer Permittivity Reconstruction

In the previous sections, the permittivity reconstruction of one-layer, one-dimension structure was discussed in detail. This section focuses on the permittivity reconstruction of multi-layer structures and also covers the different methods, including optimization algorithms, used to characterize each layer's dielectric constants. It will be shown that optimization algorithms are not the most reliable choices for unique permittivity reconstruction and microwave imaging, especially in medical applications, where results reliability is of paramount importance.

### 3.6.1 Theoretical Formulations

This part focuses on explaining the theoretical foundations of multi-layer structures excited by transverse electromagnetic waves (TEM). Fig. 3.14 shows an N-layer structure which is extended in z-direction. Each layer has uniform permittivity and permeability. The interface locations between layers are determined by $d_i$s, i=1,2, ..., N-1. The structure is excited with a TEM field with a propagation constant in the z-direction. At the interfaces, multiple reflections and transmissions occur. The local reflection and transmission at each interface, which are due to the difference in the permittivities and permeabilities of the two adjacent layers, are defined as follows:

$$R_{i,i+1}^{TE} = \frac{\mu_{i+1}k_i - \mu_i k_{i+1}}{\mu_{i+1}k_i + \mu_i k_{i+1}} \tag{3.15}$$

$$T_{i,i+1}^{TE} = \frac{2\mu_{i+1}k_i}{\mu_{i+1}k_i + \mu_i k_{i+1}} \tag{3.16}$$

$$k_i = \omega\sqrt{\mu_i \epsilon_i}$$

where $R_{i,i+1}^{TE}$ and $T_{i,i+1}^{TE}$ are the local reflection and transmission between layers i and i+1, respectively. $k_i$ is the propagation constant, $\mu_i$ and $\epsilon_i$ are the permeability and permittivity of layer i.

Since the wave travels through other layers and hits different interfaces, multiple local reflections and transmissions occur. Then, these reflected and transmitted waves travel through other layers and reach other interfaces, resulting in a series of reflected and transmitted waves at each interface. Therefore, a total reflection and transmission need to be defined for each interface to contain all the reflections and transmissions. The relations for such an interaction are defined as follows:

$$\hat{R}_{i,i+1} = R_{i,i+1} + \frac{R_{i,i+1} + \hat{R}_{i+1,i+2}e^{2jk_{i+1}(d_{i+1}-d_i)}}{1 + R_{i,i+1}\hat{R}_{i+1,i+2}e^{2jk_{i+1}(d_{i+1}-d_i)}} \tag{3.17}$$

where $\hat{R}_{i,i+1}$ is the total reflection at the interface of layer i and i+1.

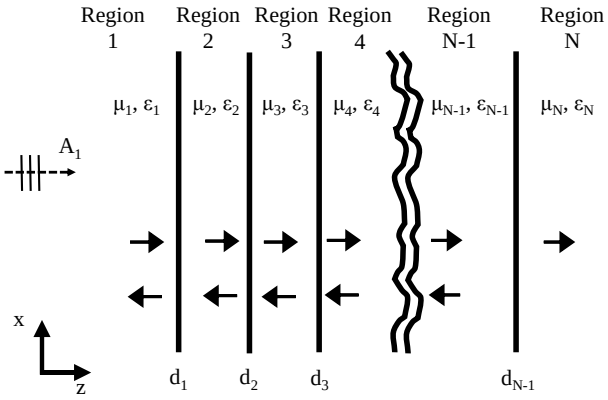


Figure 3.14: Reflections and transmissions in a multi-layer structure with uniform permittivity in each layer.

Equation 3.17 needs to be solved recursively. Considering $\hat{R}_{N,N+1} = 0$, which means no reflection occurs in the last layer, these equations can be solved in reverse by starting from the end and moving to the beginning.

The next step is to find the waves amplitudes, calculated as follows:

$$A_i e^{jk_i d_{i-1}} = A_1 e^{jk_1 d_1} \prod_{m=1}^{i-1} e^{jk_m(d_m - d_{m-1})} S_{m,m+1} \tag{3.18}$$

where $A_i$ is the amplitude of a traveling wave in the direction of propagation.

$$S_{i,i+1} = \frac{T_{i,i+1}}{1 + R_{i,i+1}\hat{R}_{i+1,i+2} e^{2jk_{i+1}(d_{i+1} - d_i)}} \tag{3.19}$$

where $S_{i,i+1}$ is a variable.

A generalized transmission coefficient is defined as

$$\hat{T}_{1,N} = \prod_{m=1}^{N-1} e^{jk_m(d_m - d_{m-1})} S_{m,m+1} \tag{3.20}$$

where it is assumed that $d_0 = d_1$. Therefore,

$$A_N e^{jk_N(d_{N-1})} = \hat{T}_{1,N} A_1 e^{jk_1 d_1} \tag{3.21}$$

Equations 3.17-3.21 need to be solved recursively for $A_i$ values, i=1,2, ...,N. Once the amplitudes are calculated, the output power in region N can be obtained in this manner:

$$P_{out} = \frac{1}{2} Re(\mathbf{E_N} \times \mathbf{H_N^*}) = \frac{\left|A_N^+\right|^2}{2\eta_N} \tag{3.22}$$

where $\eta_N$ is the impedance of layer N, defined as

$$\eta_N = \sqrt{\frac{\mu_N}{\epsilon_N}}$$

In 3.22, $P_{out}$ is the outgoing power in region N, $E_N$ and $H_N$ are the electric and magnetic fields, respectively. Equation 3.22 is a nonlinear frequency dependent relation, in the general form of 3.7.

## 3.7 N-Layer Permittivity Reconstruction

The objective is to solve 3.22 for N unknowns, which are the permittivity values of the layers, considering that the structure is non-magnetic, that is $\mu = \mu_0$. Therefore, at least N independent equations are required to calculate the unique solution, which is a set of permittivities that satisfy 3.22 at every single frequency. In the case of $N = 3$, which is consist of one dielectric layer and two vacuum layers, the procedure needed to find the unknown permittivity was explained in Chapter 2.

### 3.7.1 Three-Layer Permittivity Reconstruction

Without the loss of generality, if the structure is considered to have five layers, the number of unknown permittivities shrinks to three: $\epsilon_2, \epsilon_3, \epsilon_4$. Here, it is assumed that the first and

last layers are free space, $\epsilon_1 = \epsilon_0, \epsilon_5 = \epsilon_0$. Therefore, if a plane wave with an amplitude of $A_1 = 1V/m$ excites the structure, 3.22 becomes

$$P_{out} = \frac{1}{2} Re(\mathbf{E_5} \times \mathbf{H_5^*}) = \frac{\left|A_5^+\right|^2}{2\eta_0} \tag{3.23}$$

where

$$\eta_1 = \eta_5 = \eta_0 = \sqrt{\frac{\mu_0}{\epsilon_0}}$$

The complex nonlinear equation of 3.23 can be solved in several ways for the three unknowns, considering that all permittivities are real for now: optimization algorithms such as particle swarm (PSO), genetic, and non-sorted genetic; Newton-based and gradient methods; and exhaustive searching. According to the reality, the range of each permittivity value is between 1 to 100. Exhaustive searching, PSO, and non-sorted genetic algorithm II are exploited here to solve the problem.

### Exhaustive Searching

In 3.23, $P_{out}$ is the output power in region five, obtained from simulations. The very right side of this equation is the analytical solution for such a structure. Exhaustive searching means evaluating every single possible combination of $(\epsilon_2, \epsilon_3, \epsilon_4)$ in the right side of 3.23 at various frequencies, with the assumption of having non-dispersive materials within a narrow band of frequency. Therefore, the problem is searching for the values of $\epsilon_2$, $\epsilon_3$, $\epsilon_4$ a three-layer structure. Exhaustive searching needs the search space to be discretized, therefore, each dimension is discretized using the steps of 0.01. Thus, the number of points that needs to be evaluated is approximately $10000^3$.

As an example, a three-layer slab of dielectric material was simulated in a CST Microwave Studio, then was excited with a plane wave with the incident amplitude of $A_1 = 1V/m$. The structure's dimensions and represented in Table 3.5, considering that $d_1 = 0$. A total of ten frequencies from 100 to $190MHZ$ were chosen to evaluate 3.22 at each combination of permittivities. The algorithm explained in chapter two is exploited here

Table 3.5: Simulated Model's Information, Permittivities and Thicknesses Values.

| Layer Number | Thickness (cm) | True Permittivity |
|---|---|---|
| 2 | 10 | $\epsilon_2 = 3$ |
| 3 | 20 | $\epsilon_3 = 6$ |
| 4 | 15 | $\epsilon_4 = 10$ |

Table 3.6: Reconstructed Permittivities Using Exhaustive Method for the Three-Layered Medium With Parameters Given in Table 3.5.

| True Permittivity | Reconstructed Permittivity |
|---|---|
| $\epsilon_2 = 3$ | $\epsilon_2 = 3$ |
| $\epsilon_3 = 6$ | $\epsilon_3 = 6$ |
| $\epsilon_4 = 10$ | $\epsilon_4 = 9.99$ |

to search through $10^{12}$ points. After applying LMS, the solutions were obtained and are shown in Table 3.6. The accuracy of these solutions is very high. Other scenarios, from very thin layers to very thick ones and from low permittivity values to high ones, were also tested, and showed the same degree of accuracy.

However, searching all the possibilities, $10^{12}$ for the three unknowns using exhaustive method is not an optimum solution. This situation becomes even more critical when the number of unknowns increases. It is important to note that the permittivities considered here were all real; otherwise, if complex, the number of unknowns is indeed doubled, to six for a three-layer model. A typical number for the unknowns in a practical situation, in which the length of a structure is approximately 15 cm, is at least 50 if the thickness of each layer is considered to be 3 mm. Therefore, if the model is divided into finer segments to increase the resolution, the number of unknowns rises significantly. In conclusion, exhaustive searching is not suitable when large number of unknowns must be characterized. One alternative is to use optimization algorithms.

### Multi-Objective Particle Swarm Optimization

To solve 3.22, various types of optimization algorithms can be used. One of the most powerful tools is particle swarm optimization, which falls into the category of heuristic-based optimizations and was originally inspired by bird migration and navigation. Particle swarm optimization, PSO, was established based on the social behavior of flocks of birds. The algorithm of PSO incorporates the location of each bird, its distance from others, and their velocities. The birds, represented as random points, need to be spread diversely enough throughout a space. Then the objective function, 3.22, is evaluated at each of these points. These birds then communicate their objective function values and decide to change their direction and fly, with a specific speed, follow the birds with the most accurate values. Once they move from their current positions to newer ones, their locations are again evaluated in the objective functions and they again change their directions to follow the bird with the best objective function values. This process continues until all flight lines follow that of the lead bird and they reach their destination. Full details are explained in [95, 96].

However, in the permittivity reconstruction problem discussed earlier in this chapter, there are more than one objective functions; therefore, evaluating one function is not enough. One solution is to apply multi-objective particle swarm optimization (MOPSO), which was introduced by [97, 98]. MOPSO needs to be used to find the unique and global solution that satisfies all the objective functions generated at different frequencies taken from 3.22. Therefore, birds are distributed throughout the space of each of these objective functions. They then communicate with each other continuously until they all align with the global solution. The algorithm is almost the same as PSO, but with a set of objective function values for each bird, which complicates decision making.

To evaluate the efficiency and accuracy of this method, a three-layered model using the parameters given in Table 3.5 is considered. MOPSO is applied to solve ten objective functions, each at a single frequency, ranging from 100 MHz to 190 MHz, with a step of 10 MHz. The best reconstructed results after twenty-five iterations are shown in Table 3.7.

As observed from 3.7, the accuracy level of the reconstructed dielectric constant is not very high, although the search range is confined to [1 100] for each unknown. In addition,

Table 3.7: Reconstructed Permittivities Using MOPSO for the Three-Layer Medium With Parameters Given in Table 3.5.

| True Permittivity | Reconstructed Permittivity |
|---|---|
| $\epsilon_2 = 3$ | $\epsilon_2 = 2.9642$ |
| $\epsilon_3 = 6$ | $\epsilon_3 = 6.4367$ |
| $\epsilon_4 = 10$ | $\epsilon_4 = 9.4019$ |

Table 3.8: Reconstructed Permittivities Using NSGA for the Three-Layer Medium with Parameters Given in 3.5.

| True Permittivity | Reconstructed Permittivity |
|---|---|
| $\epsilon_2 = 3$ | $\epsilon_2 = 2.1063$ |
| $\epsilon_3 = 6$ | $\epsilon_3 = 3.05214$ |
| $\epsilon_4 = 10$ | $\epsilon_4 = 10.1403$ |

it is important to note that the reconstructed results reported here are among the best achieved. Indeed, the chance of getting even this level of accuracy is only 50-60% over an average of twenty-five runs. Therefore, neither the accuracy nor the chance of returning the global solution is sufficient, to be used especially in medical imaging, for which reliability and accuracy are vital. The results worsen when the number of unknowns increases.

### Non-Sorted Genetic Algorithm

Another algorithm that is capable of solving many objective functions at the same time for a global solution is non-sorted genetic algorithm (NSGA). In this research, NSGA-II is applied on the same ten functions produced for MOPSO. Details of this algorithm are explained in [99, 100]. The reconstructed permittivities for the same three-layer structure provided in Table 3.5 are given in Table 3.8.

NSGA-II seems more accurate than MOPSO, at least for the types of functions introduced here. It also has a higher rate of returning the right answers than MOPSO, approximately 60-70 %.

Table 3.9: The Information for a Five-Layer Slab of Dielectric Material, Permittivities and Thicknesses Values.

| Layer Number | Thickness (cm) | True Permittivity |
|---|---|---|
| 2 | 10 | $\epsilon_2 = 5$ |
| 3 | 20 | $\epsilon_3 = 8$ |
| 4 | 15 | $\epsilon_4 = 12$ |
| 5 | 3 | $\epsilon_5 = 13$ |
| 6 | 7 | $\epsilon_6 = 2$ |

### 3.7.2 Five-Layer Permittivity Reconstruction

In the next scenario, a structure consisting of five layers, excluding free space layers, is analyzed for permittivity reconstruction. In total, twenty functions generated from 3.22 at frequencies from 100 MHz to 290 MHz, with a step of 10 MHz, are considered as the objective functions. In all these generated functions, the amplitude of the incident electric field is 1 V/m. The structure dimensions and permittivities are given in Table 3.9.

Exhaustive method, MOPSO, and NSGA-II are all used to find the global solutions. The results are given by Table 3.10. As observed from Table 3.10, exhaustive method returns a solution with a very high accuracy. MOPSO, however, does not have enough accuracy, and the rate of getting this accuracy after many runs is only 40-50%. Although NSGA-II returns more-accurate numbers for the dielectric constants than MOPSO does, its rate of approximately 60% is still not enough.

## 3.8 Conclusion

This chapter proposes a method to determine the dielectric permittivity of materials based on real power measurements. The concept presented in this work relies only on the amplitude of the transmitted signal and does not require phase information. Therefore, the use of vector network analyzers that require expensive setups was eliminated. Multiple samples of power measurement are used at different frequencies within a narrow bandwidth to

Table 3.10: Reconstructed Permittivities Using NSGA for the Three-Layer Medium With Parameters Given in Table3.9.

| True Permittivity | Reconstructed Permittivity | | |
|---|---|---|---|
| | Exhaustive | MOPSO | NSGA-II |
| $\epsilon_2 = 5$ | $\epsilon_2 = 5$ | $\epsilon_2 = 6.4358$ | $\epsilon_2 = 4.8980$ |
| $\epsilon_3 = 8$ | $\epsilon_3 = 8.05$ | $\epsilon_3 = 7.4943$ | $\epsilon_3 = 7.9900$ |
| $\epsilon_4 = 12$ | $\epsilon_4 = 12$ | $\epsilon_4 = 15.3227$ | $\epsilon_4 = 11.9410$ |
| $\epsilon_5 = 13$ | $\epsilon_5 = 13$ | $\epsilon_5 = 13.7830$ | $\epsilon_5 = 13.1110$ |
| $\epsilon_6 = 2$ | $\epsilon_6 = 2$ | $\epsilon_6 = 1.3197$ | $\epsilon_6 = 2.1070$ |

reconstruct the permittivity value of materials. Therefore, our method results in a permittivity reconstruction technique that is less sensitive to errors while removing the ambiguity in the permittivity retrieval. For validation, two different setups using free-space and the coaxial line were employed in simulations. We showed that the algorithm presented in this paper reconstructs the permittivity with high accuracy level.

The method was also experimentally applied to different types of materials ranging from low-loss to high-loss with no prior knowledge about the loss. A full comparison between the method in this work and the open-ended coaxial method showed a higher agreement between our method, on the one hand, and theory on the other. The results obtained were validated with permittivity values reported in the literature, showing that the proposed method provides accurate permittivity reconstruction both in the real and imaginary parts of the dielectric.

Permittivity reconstructions for three-layer and five-layer structures have been also discussed. The reconstructions using exhaustive method, multi-objective particle swarm optimization, and non-sorted genetic algorithm were discussed. It was shown that exhaustive searching is not possible when the search space is very large even though its results are very accurate. Optimization algorithms, although very fast, do not have enough accuracy. They also suffer from a low rate of convergence. In addition, the functions should be very smooth without having deep valleys; otherwise the algorithm become trapped into vallies and cannot escape. Furthermore, the range of the search space needs to be narrow; oth-

erwise, searching a very large space for a single global minimum is cumbersome for these optimization algorithms. Consequently, the chance of satisfying all the objective functions at the same time is very low.

# Chapter 4

# Conclusions and Future Works

## 4.1 Microwave Imaging for Short Range Application

This thesis introduced a novel imaging modality that has never been proposed before. It combines the reconstructive ability of the Radon transform with microwaves thus providing high resolution imaging while using low-power non-ionizing radiation. The ideas presented in this thesis provided a new perspective with wide reaching implications related to the use of low frequencies for providing high resolution images of not only human tissues but also concealed items in a broad range of security applications. This thesis focused on short range applications with a high potential for medical imaging. The outcome of this project was a low-cost non-ionizing imaging technology which has no rival at this time. This technology will potentially make microwave imaging much more practical by reducing the time and removing the simulations need. This accessibility results in significant reduction in healthcare costs.

We showed a novel qualitative imaging technique using highly localized radiators or electrically-small antennas to generate images with high resolution at frequencies close to the lower end of the microwaves spectrum. We showed that electrically-small and localized radiators create an impression at the receiver (i.e., received signal) in such a way that the primary contribution at the receiver is due to the direct path between the transmitter and

receiver, or more precisely, due to the material present in this direct path. Therefore, the waves interaction with the interrogated medium is highly similar to way X rays interact with the medium in the sense that X rays leave an impression on the film (i.e., receiver or receiving point) that is directly dependent on the tissues in the straight path that the X rays traverse. This non-intuitive behavior can potentially make a significant change in the current available microwave imaging system because the reconstruction approach can be analogous to the one used in computerized tomography (CT), which is based on the Radon transform and ray illumination. The antennas were placed very close to the object under test (OUT) to take advantage of the evanescent spectrum of the radiated field. Therefore, the resolution obtained from our preliminary test is significantly high, less than $\lambda/50$ when using the rudimentary scanning system that we developed to obtain preliminary data. To the best of our knowledge no one has proposed such an idea which can remove multiple scattering in low frequencies and build a full imaging system with high resolution.

A key innovation of the introduced imaging system its low-cost and high resolution. Additionally, the introduced system is fast, primarily because we removed the use of simulation models (forward solutions), which decreases the computational cost significantly. In addition, no priori knowledge is required in our system, so, the use of MRI images or CTs is removed. Thus, no optimization is needed to generate images because we create images without searching.

We used the filtered-back projection reconstruction method, which assumes that the OUT is interrogated by rays traveling in straight lines. This assumption is valid when the excitation frequency is very high, as in X rays. In low frequencies, such an assumption has been problematic for researchers because the wavelength is large and thus diffraction and scattering from the OUT constituents are significant. Therefore, the radiated field does not show ray-like behavior. Our method, however, used electrically-small radiators which, most non-intuitively, reduced the effect of diffraction and especially coupling between propagation paths. Consequently, the waves interact with the adjacent OUT slices (paths) minimally, thus contributing primarily to the OUT slice located between the transmitter and the receiver. Hence, the main information collected by the receiver is a reflection of the OUT slice that connects the transmitter to the receiver. We showed a series of simulations and experiments that prove the ray-like behavior of electrically small antennas in

the near field. This was the primary principle and discovery on which our entire imaging system is based. Our group previously showed that when the sensors or receivers are electrically-small and the scanning takes place in the near field of the OUT, the sensing resolution can be very high. However, no 2D or 3D images were created, only the object under test was scanned to detect changes. In addition, such sensing, which is only based on reflections, could not detect changes below few centimeters. Our system provided full 2D (slice) images, based on transmitted signals. In addition, our developed image reconstruction algorithm generated images that showed not only changes but also a descriptive information about the OUT.

## 4.2 Material Characterization

In the second part of the thesis, we introduced a new material characterization approach that removed the use of phase measurement in permittivity measurements, yet maintaining the high accuracy level of the material under test. Our method only uses the power amplitude of transmitted signals collected by a power meter or spectrum analyzer. Multiple frequency samples were used to reconstruct the permittivity with high precision. Our simulations and experimental results proved the accuracy and validity of our proposed method. Various materials were tested and their permittivity were reconstructed. Multilayer structures were also tested using our power method with different optimization algorithms. The results showed that our method is capable of reconstructing the permittivity of such medium assuming that the materials under tests are not dispersive.

## 4.3 Future Work

The presented microwave imaging system that was introduced in this thesis can be potentially useful for microwave breast imaging which is considered as short-range scenario. To extend our work further and apply it to more realistic cases, human phantoms need to be tested and imaged.

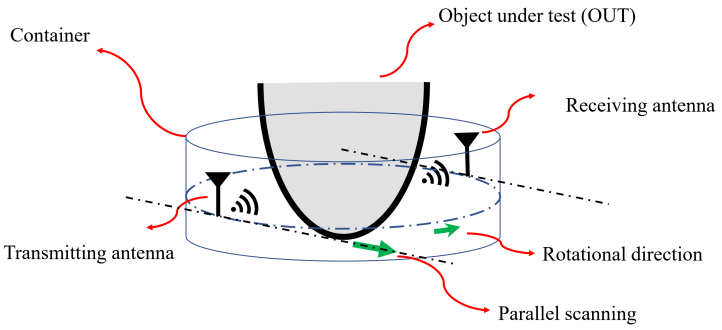


Figure 4.1: Real-world scanning system with the object under test.

### 4.3.1 Consideration for Real-World Implementation

While the introduced microwave imaging system calls for the development of a very general imaging system, the motivation initially is to develop the current system to be well-suited for breast imaging. Fig. 4.1 shows the rotational scanning system we plan to develop. The designed antennas are placed in the opposite side of each other, where the OUT is placed in between. We scan the object under test at angles from 0 to 360. At each angle, the object is scanned along two parallel lines shown in Figure 4.1.

Fig. 4.2 shows a patient under examination in prone position [1]. The operation of the microwave imaging in practical real-world scenarios is as follows: The patient lies in prone position. The antennas scan the breast on two parallel lines shown in Fig. 4.1. The antennas then rotate with an angle $\Delta\theta$ and scan the object along two parallel line. This process continues until completing full scan around the breast. The scanning is automated so that the scanning process time does not exceed a few minutes. Our software then processes the collected data to generate an image. No simulation software is required.

[1] Photo courtesy of https://www.chalmers.se

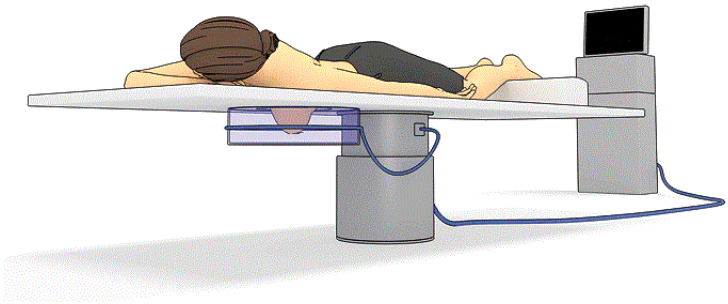

Figure 4.2: Patient under microwave testing.

### 4.3.2 Approach

#### Probe Design to Increase Sensitivity

The antennas/probes that were used in the preliminary results were electrically very small, less than $\lambda/20$ with an ultra-narrow frequency band. Having a narrowband antenna removes the dispersion effect of human tissues, isolating the detection to only the permittivity changes in the OUT at a single frequency. Having an electrically very small antenna reduces the diffraction and scattering within and from the OUT. Therefore, wave behaves like X-rays propagation, in straight lines, thus, we can apply the Radon transform with the filtered-back projection to reconstruct the object under test. The antennas interact with the body under test in the near-zone where the sensitivity to any changes in the body under test is significant. Our future work will shrink the antenna sizes appreciably. This decreases the diffraction effect increases the sensitivity, and consequently enhances the images resolution. Shrinking the antenna size results in constraining its emitted power. Therefore, we need to design integrated amplifiers to compensate the lost power. Such an amplifier should be designed to be matched with our antenna and its matching network. Another amplifier is also used at the receiver side to enhance the received signal. Another approach we will be implementing is to design an active antenna that compensates for the power limitations imposed on electrically-small antenna. We will also be exploring new electrically-small radiation sources based on the concept of metamaterial cells which provides control over the composition of the near field. We will also explore the effect of

field polarization on the sensitivity of the receiver.

### Experiments Using Realistic Breast Phantoms

The past 5 years have witnessed the commercial development of breast phantoms which have realistic resemblance to real human breasts. These phantoms were developed for a variety of purposes such as training of healthcare providers especially those involved in helping women during breast exams. They were also developed for research purposes and for training of medical doctors who perform surgeries or validating MRI/CT/Ultrasound technologies. We plan to incorporate these phantoms in our testing protocols. In fact, some of these phantoms can be tumorous where tumors are positioned at different locations and with different These phantoms were developed based MRI or ultrasound or CT data. We also plan to incorporate into our testing phantoms made of chicken meat or beef to resemble, at least in topology, the shapes of human female breasts. Metallic or dielectric beads will be inserted to mimic the presence of anomalies within the breast.

### Implementation of Fan Beam Scanning

Our current reconstruction algorithm is based on parallel scanning, therefore, we lose precious information that can be captured by placing receivers in the neighborhood of the parallel receiver. To enhance the resolution of our scanning system, we plan to implement fan-beam scanning. Fig. 4.3 shows a schematic illustrating the operation of the fan-beam scanning system where multiple sensors collect data coming from straight paths emanating from a localized source. Again, based on our theory that we discussed above, the signals are expected to reflect the composition of the tissues in their direct paths. Then the antennas rotate and the same process is repeated at other angles to create an image using fan-beam scanning.

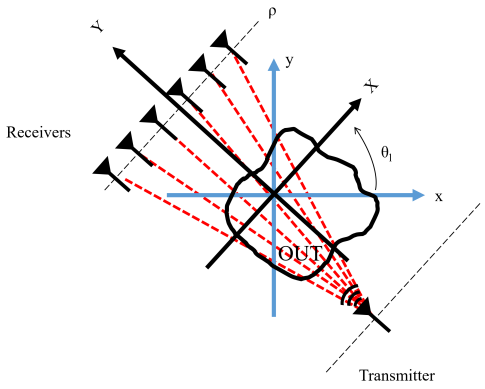


Figure 4.3: Fan-beam scanning system.

**Implementation of Conformal Antenna Array for Fast Scanning and Processing of Data**

To eliminate mechanical scanning, we plan to develop a electronically-static transmitter-receiver system that eliminates the need for both manual or automated mechanical scanning. Our scanning procedure, as discussed, is currently accomplished using single transmitter/receiver in our prototype. This procedure can be carried out using multiple antennas or antenna arrays. The former is time-consuming, and the scanning may take many hours to achieve a desired resolution; however, there will be no significant coupling between radiation sources and receivers. The latter one requires many antennas to be placed around the object under test, yielding significant decrease in scanning time but coupling between antennas may cause image artifacts [35]. Recently the use of multi input multi output antennas was introduced for microwave imaging purposes [36]. The MIMO idea can reduce the number of antennas significantly because the scanning system can transmit and receive the information by the same set of antennas simultaneously. The result of using MIMO array is the same resolution as what conventional arrays offer can be obtained with fewer elements. Additionally, the MIMO array can contain asymmetrical transmitter and receivers that provides more control on the generated fields [36]. We plan to develop the MIMO mechanism in our scanning system using and enhancing our mechanical scanning procedure, making the real life implementation more feasible. Additionally, various

types of radiation sources such as conformal metasurface structures and active transmitters/receivers will be investigated and employed if they achieve higher image resolution.

# References


[1] S. S. Ahmed, A. Schiessl, F. Gumbmann, M. Tiebout, S. Methfessel, and L.-P. Schmidt, "Advanced microwave imaging," *IEEE microwave magazine*, vol. 13, no. 6, pp. 26–43, 2012.

[2] M. Pastorino, *Microwave imaging*, Apr., vol. 208.

[3] V. Zhurbenko, "Challenges in the design of microwave imaging systems for breast cancer detection," *Advances in Electrical and Computer Engineering*, vol. 11, no. 1, pp. 91–96, 2011.

[4] S. Kharkovsky and R. Zoughi, "Microwave and millimeter wave nondestructive testing and evaluation-overview and recent advances," *IEEE Instrumentation & Measurement Magazine*, vol. 10, no. 2, pp. 26–38, 2007.

[5] L.-F. Chen, C. Ong, C. Neo, V. Varadan, and V. K. Varadan, *Microwave electronics: measurement and materials characterization*. John Wiley & Sons, Nov. 2004.

[6] N. K. Nikolova, "Microwave imaging for breast cancer," *IEEE microwave magazine*, vol. 12, no. 7, pp. 78–94, Dec.

[7] R. Chandra, H. Zhou, I. Balasingham, and R. M. Narayanan, "On the opportunities and challenges in microwave medical sensing and imaging," *IEEE transactions on biomedical engineering*, vol. 62, no. 7, pp. 1667–1682, 2015.

[8] D. OLoughlin, M. OHalloran, B. M. Moloney, M. Glavin, E. Jones, and M. A. Elahi, "Microwave breast imaging: Clinical advances and remaining challenges," *IEEE Transactions on Biomedical Engineering*, vol. 65, no. 11, pp. 2580–2590, 2018.

[9] P. Suetens, *Fundamentals of medical imaging*. Cambridge university press, 2017.

[10] A. C. Kak and M. Slaney, *Principles of computerized tomographic imaging*. IEEE press New York, 1988.

[11] S. Semenov, "Microwave tomography: review of the progress towards clinical applications," *Philosophical Transactions of the Royal Society A: Mathematical, Physical and Engineering Sciences*, vol. 367, no. 1900, pp. 3021–3042, 2009.

[12] M. A. Bernstein, K. F. King, and X. J. Zhou, *Handbook of MRI pulse sequences*. Elsevier, 2004.

[13] V. R. Korde, G. T. Bonnema, W. Xu, C. Krishnamurthy, J. Ranger-Moore, K. Saboda, L. D. Slayton, S. J. Salasche, J. A. Warneke, D. S. Alberts *et al.*, "Using optical coherence tomography to evaluate skin sun damage and precancer," *Lasers in Surgery and Medicine: The Official Journal of the American Society for Laser Medicine and Surgery*, vol. 39, no. 9, pp. 687–695, 2007.

[14] E. C. Fear, P. M. Meaney, and M. A. Stuchly, "Microwaves for breast cancer detection?" *IEEE potentials*, vol. 22, no. 1, pp. 12–18, 2003.

[15] P. M. Meaney, "Microwave imaging and emerging applications," *International journal of biomedical imaging*, vol. 2012, 2012.

[16] M. J. Pallone, P. M. Meaney, and K. D. Paulsen, "Surface scanning through a cylindrical tank of coupling fluid for clinical microwave breast imaging exams," *Medical physics*, vol. 39, no. 6Part1, pp. 3102–3111, 2012.

[17] A. H. Golnabi, P. M. Meaney, S. Geimer, and K. D. Paulsen, "Microwave imaging for breast cancer detection and therapy monitoring," in *2011 IEEE Topical Conference on Biomedical Wireless Technologies, Networks, and Sensing Systems*. IEEE, 2011, pp. 59–62.

[18] A. Baran, D. J. Kurrant, A. Zakaria, E. C. Fear, and J. LoVetri, "Breast imaging using microwave tomography with radar-based tissue-regions estimation," *Progress In Electromagnetics Research*, vol. 149, pp. 161–171, 2014.

[19] T. M. Grzegorczyk, P. M. Meaney, P. A. Kaufman, K. D. Paulsen *et al.*, "Fast 3-d tomographic microwave imaging for breast cancer detection," *IEEE Transactions on Medical Imaging*, vol. 31, no. 8, pp. 1584–1592, Aug.

[20] N. Epstein, P. Meaney, and K. Paulsen, "3d parallel-detection microwave tomography for clinical breast imaging," *Review of Scientific Instruments*, vol. 85, no. 12, p. 124704, 2014.

[21] A. Martellosio, M. Pasian, M. Bozzi, L. Perregrini, A. Mazzanti, F. Svelto, P. E. Summers, G. Renne, L. Preda, and M. Bellomi, "Dielectric properties characterization from 0.5 to 50 ghz of breast cancer tissues," *IEEE Transactions on Microwave Theory and Techniques*, vol. 65, no. 3, pp. 998–1011, 2016.

[22] M. Lazebnik, L. McCartney, D. Popovic, C. B. Watkins, M. J. Lindstrom, J. Harter, S. Sewall, A. Magliocco, J. H. Booske, M. Okoniewski *et al.*, "A large-scale study of the ultrawideband microwave dielectric properties of normal breast tissue obtained from reduction surgeries," *Physics in Medicine & Biology*, vol. 52, no. 10, p. 2637, 2007.

[23] M. Lazebnik, D. Popovic, L. McCartney, C. B. Watkins, M. J. Lindstrom, J. Harter, S. Sewall, T. Ogilvie, A. Magliocco, T. M. Breslin *et al.*, "A large-scale study of the ultrawideband microwave dielectric properties of normal, benign and malignant breast tissues obtained from cancer surgeries," *Physics in Medicine & Biology*, vol. 52, no. 20, p. 6093, 2007.

[24] H. Woodard and D. White, "The composition of body tissues," *The British journal of radiology*, vol. 59, no. 708, pp. 1209–1218, 1986.

[25] P. M. Meaney, A. P. Gregory, N. R. Epstein, and K. D. Paulsen, "Microwave open-ended coaxial dielectric probe: interpretation of the sensing volume re-visited," *BMC medical physics*, vol. 14, no. 1, p. 3, 2014.

[26] S. Y. Semenov, A. E. Bulyshev, A. E. Souvorov, R. H. Svenson, Y. E. Sizov, V. Vorisov, V. G. Posukh, I. M. Kozlov, A. G. Nazarov, and G. P. Tatsis, "Microwave tomography: Theoretical and experimental investigation of the iteration reconstruction algorithm," *IEEE transactions on microwave theory and techniques*, vol. 46, no. 2, pp. 133–141, 1998.

[27] P. M. Meaney, A. H. Golnabi, N. R. Epstein, S. D. Geimer, M. W. Fanning, J. B. Weaver, and K. D. Paulsen, "Integration of microwave tomography with magnetic resonance for improved breast imaging," *Medical physics*, vol. 40, no. 10, p. 103101, 2013.

[28] P. M. Meaney, K. D. Paulsen, B. W. Pogue, and M. I. Miga, "Microwave image reconstruction utilizing log-magnitude and unwrapped phase to improve high-contrast object recovery," *IEEE Transactions on Medical Imaging*, vol. 20, no. 2, pp. 104–116, 2001.

[29] M. Bertero, M. Miyakawa, P. Boccacci, F. Conte, K. Orikasa, and M. Furutani, "Image restoration in chirp-pulse microwave ct (cp-mct)," *IEEE transactions on biomedical engineering*, vol. 47, no. 5, pp. 690–699, 2000.

[30] O. P. Franza, "Formal compensation of sensor-related interactions for microwave tomography." 1999.

[31] P. Kosmas and C. M. Rappaport, "Time reversal with the fdtd method for microwave breast cancer detection," *IEEE Transactions on Microwave Theory and Techniques*, vol. 53, no. 7, pp. 2317–2323, 2005.

[32] D. Li, P. M. Meaney, T. Raynolds, S. A. Pendergrass, M. W. Fanning, and K. D. Paulsen, "Parallel-detection microwave spectroscopy system for breast imaging," *Review of Scientific Instruments*, vol. 75, no. 7, pp. 2305–2313, Jul.

[33] W. C. Khor, M. E. Bialkowski, A. Abbosh, N. Seman, and S. Crozier, "An ultra wideband microwave imaging system for breast cancer detection," *IEICE Transactions on Communications*, vol. 90, no. 9, pp. 2376–2381, 2007.

[34] E. C. Fear, X. Li, S. C. Hagness, and M. A. Stuchly, "Confocal microwave imaging for breast cancer detection: Localization of tumors in three dimensions," *IEEE Transactions on Biomedical Engineering*, vol. 49, no. 8, pp. 812–822, Aug.

[35] R. E. Davidsen, J. A. Jensen, and S. W. Smith, "Two-dimensional random arrays for real time volumetric imaging," *Ultrasonic Imaging*, vol. 16, no. 3, pp. 143–163, 1994.

[36] X. Zhuge and A. G. Yarovoy, "Three-dimensional near-field mimo array imaging using range migration techniques," *IEEE Transactions on Image Processing*, vol. 21, no. 6, pp. 3026–3033, 2012.

[37] M. Ravan, R. K. Amineh, and N. K. Nikolova, "Two-dimensional near-field microwave holography," *Inverse Problems*, vol. 26, no. 5, p. 055011, 2010.

[38] R. K. Amineh, M. Ravan, A. Khalatpour, and N. K. Nikolova, "Three-dimensional near-field microwave holography using reflected and transmitted signals," *IEEE Transactions on Antennas and Propagation*, vol. 59, no. 12, pp. 4777–4789, 2011.

[39] D. M. Sheen, D. L. McMakin, and T. E. Hall, "Near field imaging at microwave and millimeter wave frequencies," in *Microwave Symposium, 2007. IEEE/MTT-S International*. IEEE, 2007, pp. 1693–1696.

[40] J. W. Goodman, *Introduction to Fourier optics*. Roberts and Company Publishers, 2005.

[41] D. Slater, *Near-field antenna measurements*. Artech House, 1991.

[42] X. Wu and O. M. Ramahi, "Near-field scanning microwave microscopy for detection of subsurface biological anomalies," in *IEEE Antennas and Propagation Society Symposium, 2004.*, vol. 3. IEEE, 2004, pp. 2444–2447.

[43] O. M. Ramahi and M. H. Kermani, "Transmission line resonators for breast tumor detection," in *2005 IEEE Antennas and Propagation Society International Symposium*, vol. 3. IEEE, 2005, pp. 803–806.

[44] A. H. Golnabi, P. M. Meaney, N. R. Epstein, and K. D. Paulsen, "Three-dimensional microwave imaging with incorporated prior structural information," in *Medical Imaging 2012: Biomedical Applications in Molecular, Structural, and Functional Imaging*, vol. 8317, Apr., p. 83171L.

[45] A. H. Golnabi, P. M. Meaney, S. D. Geimer, and K. D. Paulsen, "Comparison of no-prior and soft-prior regularization in biomedical microwave imaging," *Journal of Medical Physics/Association of Medical Physicists of India*, vol. 36, no. 3, p. 159, 2011.

[46] P. M. Meaney, F. Shubitidze, M. W. Fanning, M. Kmiec, N. R. Epstein, and K. D. Paulsen, "Surface wave multipath signals in near-field microwave imaging," *Journal of Biomedical Imaging*, vol. 2012, p. 8, Jan. 2012.

[47] P. M. Meaney, K. D. Paulsen, and J. T. Chang, "Near-field microwave imaging of biologically-based materials using a monopole transceiver system," *IEEE Transactions on Microwave Theory and Techniques*, vol. 46, no. 1, pp. 31–45, Jan.

[48] S. H. Mirjahanmardi and O. Ramahi, "Computed tomography with microwaves for breast imaging," *US Provincial Patent*, no. 62909218, Oct., 2019.

[49] S. Gabriel, R. Lau, and C. Gabriel, "The dielectric properties of biological tissues: Ii. measurements in the frequency range 10 hz to 20 ghz," *Physics in medicine and biology*, vol. 41, no. 11, p. 2251, Nov. 1996.

[50] S. O. Nelson, W. chuan Guo, S. Trabelsi, and S. J. Kays, "Dielectric spectroscopy of watermelons for quality sensing," *Measurement Science and Technology*, vol. 18, no. 7, p. 1887, May 2007.

[51] S. Nelson and S. Trabelsi, "Dielectric spectroscopy measurements on fruit, meat, and grain," *Transactions of the ASABE*, vol. 51, no. 5, pp. 1829–1834, Sep. 2008.

[52] S. O. Nelson and S. Trabelsi, "Influence of water content on rf and microwave dielectric behavior of foods," *J. Microw. Power Electromagn. Energy*, vol. 43, no. 2, pp. 13–23, Jan. 2009.

[53] C. Dalmay, A. Pothier, P. Blondy, F. Lalloue, and M.-O. Jauberteau, "Label free biosensors for human cell characterization using radio and microwave frequencies," in *Microwave Symposium Digest, 2008 IEEE MTT-S International*, Jun. 2008, pp. 911–914.

[54] J. Kim, A. Babajanyan, A. Hovsepyan, K. Lee, and B. Friedman, "Microwave dielectric resonator biosensor for aqueous glucose solution," *Review of Scientific Instruments*, vol. 79, no. 8, Jul. 2008.

[55] S. H. Mirjahanmardi, P. Dehkhoda, and A. Tavakoli, "Forward scattering from a three dimensional layered media with rough interfaces and buried object (s) by fdtd." *Applied Computational Electromagnetics Society Journal*, vol. 32, no. 11, Nov. 2017.

[56] S. H. Mirjahanmardi, A. Tavakoli, H. Zamani, and P. Dehkhoda, "Electromagnetic scattering from a buried sphere in a two-layered rough ground," in *Antennas and Propagation & USNC/URSI National Radio Science Meeting, 2015 IEEE International Symposium*. IEEE, Jul. 2015, pp. 506–507.

[57] S. O. Nelson, L. E. Stetson, and C. W. Schlaphoff, "A general computer program for precise calculation of dielectric properties from short-circuited waveguide measurements," *IEEE Transactions on Instrumentation and Measurement*, vol. 23, no. 4, pp. 455–460, Dec. 1974.

[58] M. D. Deshpande, C. J. Reddy, P. I. Tiemsin, and R. Cravey, "A new approach to estimate complex permittivity of dielectric materials at microwave frequencies using waveguide measurements," *IEEE Transactions on Microwave Theory and Techniques*, vol. 45, no. 3, pp. 359–366, Mar. 1997.

[59] J. M. Catala-Civera, A. J. Canos, F. L. Penaranda-Foix, and E. de los Reyes Davo, "Accurate determination of the complex permittivity of materials with transmission reflection measurements in partially filled rectangular waveguides," *IEEE Transactions on Microwave Theory and Techniques*, vol. 51, no. 1, pp. 16–24, Jan. 2003.

[60] A. Nicolson and G. Ross, "Measurement of the intrinsic properties of materials by time-domain techniques," *IEEE Transactions on Instrumentation and Measurement*, vol. 19, no. 4, pp. 377–382, Nov. 1970.

[61] M. D. Deshpande, C. J. Reddy, P. I. Tiemsin, and R. Cravey, "A new approach to estimate complex permittivity of dielectric materials at microwave frequencies using waveguide measurements," *IEEE Transactions on Microwave Theory and Techniques*, vol. 45, no. 3, pp. 359–366, Mar. 1997.

[62] G. I. Torgovnikov, "Dielectric properties of wood-based materials," in *Dielectric Properties of Wood and Wood-Based Materials*. Springer, 1993, pp. 135–159.

[63] H. Kim, J. Park, I. Seo, and J. Yoo, "Two-dimensional dielectric collimator design and its experimental verification for microwave beam focusing," *Applied Physics Letters*, vol. 109, no. 15, p. 151902, Oct.

[64] J.-Y. Chung, "Broadband characterization techniques for rf materials and engineered composites," Ph.D. dissertation, The Ohio State University, 2010.

[65] D. Ghodgaonkar, V. Varadan, and V. Varadan, "Free-space measurement of complex permittivity and complex permeability of magnetic materials at microwave frequencies," *IEEE Transactions on Instrumentation and Measurement*, vol. 39, no. 2, pp. 387–394, Apr. 1990.

[66] R. M. . Redhetfer, "The measurement of dielectric constants," *in Techniques of Microwai.e Mea surenien, C. G. Montgomery,*, vol. 2, pp. 591–657, Aug. 1996.

[67] P. K. Kadaba, "Simultaneous measurement of complex permittivity and permeability in the millimeter region by a frequency-domain technique," *IEEE Transactions on Instrumentation and Measurement*, vol. 33, no. 4, pp. 336–340, Dec. 1984.

[68] V. V. Varadan and R. Ro, "Unique retrieval of complex permittivity and permeability of dispersive materials from reflection and transmitted fields by enforcing causality," *IEEE Transactions on Microwave Theory and Techniques*, vol. 55, no. 10, pp. 2224–2230, Oct. 2007.

[69] M. Maurens, A. Priou, P. Brunier, S. Aussudre, M. Lopez, and P. Combes, "Free-space microwave measurement technique for composite minerals," *Progress in Electromagnetics Research (PIER)*, vol. 6, pp. 345–85, 1992.

[70] F. Aurand, "Measurements of transient electromagnetic propagation through concrete and sand," *Sandia Report*, Sep. 1996.

[71] I. S. Seo, W. S. Chin *et al.*, "Characterization of electromagnetic properties of polymeric composite materials with free space method," *Composite Structures*, vol. 66, no. 1, pp. 533–542, Dec. 2004.

[72] J. Baker-Jarvis, E. J. Vanzura, and W. A. Kissick, "Improved technique for determining complex permittivity with the transmission/reflection method," *IEEE Transactions on Microwave Theory and Techniques*, vol. 38, no. 8, pp. 1096–1103, Aug. 1990.

[73] M. Arai, J. Binner, and T. Cross, "Estimating errors due to sample surface roughness in microwave complex permittivity measurements obtained using a coaxial probe," *Electronics Letters*, vol. 31, no. 2, pp. 115–117, Jan. 1995.

[74] D. L. Gershon, J. Calame, Y. Carmel, T. Antonsen, and R. M. Hutcheon, "Open-ended coaxial probe for high-temperature and broad-band dielectric measurements," *IEEE Transactions on Microwave Theory and Techniques*, vol. 47, no. 9, pp. 1640–1648, Sep. 1999.

[75] N. Sheen and I. Woodhead, "An open-ended coaxial probe for broad-band permittivity measurement of agricultural products," *Journal of Agricultural Engineering Research*, vol. 74, no. 2, pp. 193–202, Oct. 1999.

[76] A. Technol., "Basics of measuring the dielectric properties of materials," *Santa Clara, CA, USA, Appl.*, May 2005.

[77] P. O. Risman and N. E. Bengtsson, "Dielectric properties of food at 3 ghz as determined by a cavity perturbation technique." *Journal of Microwave Power*, vol. 6, no. 2, pp. 101–106, Jan. 1971.

[78] F.-C. Chen and W. C. Chew, "Experimental verification of super resolution in nonlinear inverse scattering," *Applied physics letters*, vol. 72, no. 23, pp. 3080–3082, Jun. 1998.

[79] R. G. Carter, "Accuracy of microwave cavity perturbation measurements," *IEEE Transactions on Microwave Theory and Techniques*, vol. 49, no. 5, pp. 918–923, May 2001.

[80] Z. Ma and S. Okamura, "Permittivity determination using amplitudes of transmission and reflection coefficients at microwave frequency," *IEEE Transactions on Microwave Theory and Techniques*, vol. 47, no. 5, pp. 546–550, May 1999.

[81] U. Hasar, O. Simsek, and A. Aydin, "Application of varying-frequency amplitude-only technique for electrical characterization of hardened cement-based materials," *Microwave and Optical Technology Letters*, vol. 52, no. 4, pp. 801–805, Apr. 2010.

[82] U. Hasar, "Two novel amplitude-only methods for complex permittivity determination of medium-and low-loss materials," *Measurement Science and Technology*, vol. 19, no. 5, p. 055706, Apr. 2008.

[83] U. C. Hasar, "A fast and accurate amplitude-only transmission-reflection method for complex permittivity determination of lossy materials," *IEEE Transactions on Microwave Theory and Techniques*, vol. 56, no. 9, pp. 2129–2135, 2008.

[84] U. Hasar, "Elimination of the multiple-solutions ambiguity in permittivity extraction from transmission-only measurements of lossy materials," *Microwave and Optical Technology Letters*, vol. 51, no. 2, pp. 337–341, Feb. 2009.

[85] U. C. Hasar and M. Bute, "Electromagnetic characterization of thin dielectric materials from amplitude-only measurements," *IEEE Sensors Journal*, vol. 17, no. 16, pp. 5093–5103, 2017.

[86] T. Isernia, L. Crocco, and M. D'Urso, "New tools and series for forward and inverse scattering problems in lossy media," *IEEE Geoscience and Remote Sensing Letters*, vol. 1, no. 4, pp. 327–331, Oct.

[87] S. R. Deans, *The Radon transform and some of its applications.* Courier Corporation, 2007.

[88] R. C. Gonzalez, R. E. Woods *et al.*, "Digital image processing," 2002.

[89] P. Kuchment, *The Radon transform and medical imaging.* SIAM, 2013.

[90] K. Jose, V. V. Varadan, R. D. Hollinger, A. R. Tellakula, and V. K. Varadan, "Non-contact broadband microwave material characterization at low and high temperatures," in *International Symposium on Optical Science and Technology.* International Society for Optics and Photonics, Jul. 2000, pp. 324–331.

[91] "CST Microwave Studio version, 2017, https://www.cst.com, last access 10-Jan-2018."

[92] Y. W. Afsar, "Measurement of complex permittivity of liquids using waveguide techniques," *Progress In Electromagnetics Research*, vol. 42, pp. 131–142, 2003.

[93] A. P. Gregory and R. Clarke, *Tables of the complex permittivity of dielectric reference liquids at frequencies up to 5 GHz.* National Physical Laboratory Teddington, 2001.

[94] E. Piuzzi, C. Merla, G. Cannazza, A. Zambotti, F. Apollonio, A. Cataldo, P. D'Atanasio, E. De Benedetto, and M. Liberti, "A comparative analysis between customized and commercial systems for complex permittivity measurements on liquid samples at microwave frequencies," *IEEE Transactions on Instrumentation and Measurement*, vol. 62, no. 5, pp. 1034–1046, 2013.

[95] R. Eberhart and J. Kennedy, "A new optimizer using particle swarm theory," in *Micro Machine and Human Science, 1995. MHS'95., Proceedings of the Sixth International Symposium on.* IEEE, 1995, pp. 39–43.

[96] J. Robinson and Y. Rahmat-Samii, "Particle swarm optimization in electromagnetics," *IEEE transactions on antennas and propagation*, vol. 52, no. 2, pp. 397–407, 2004.

[97] C. A. C. Coello, G. T. Pulido, and M. S. Lechuga, "Handling multiple objectives with particle swarm optimization," *IEEE Transactions on evolutionary computation*, vol. 8, no. 3, pp. 256–279, Jun.

[98] V. Kumar and S. Minz, "Multi-objective particle swarm optimization: An introduction," *SmartCR*, vol. 4, no. 5, pp. 335–353, Oct.

[99] K. Deb, A. Pratap, S. Agarwal, and T. Meyarivan, "A fast and elitist multiobjective genetic algorithm: Nsga-ii," *IEEE transactions on evolutionary computation*, vol. 6, no. 2, pp. 182–197, Sep.

[100] K. Deb, S. Agrawal, A. Pratap, and T. Meyarivan, "A fast elitist non-dominated sorting genetic algorithm for multi-objective optimization: Nsga-ii," in *International Conference on Parallel Problem Solving From Nature*. Springer, 2000, pp. 849–858.

[101] L. Larsen and J. Jacobi, "Microwaves offer promise as imaging modality," *Diagnostic Imag.*, vol. 11, pp. 44–47, Nov. 1982.

[102] L. E. Larsen and J. H. Jacobi, "Microwave scattering parameter imagery of an isolated canine kidney," *Medical physics*, vol. 6, no. 5, pp. 394–403, Sep.

[103] D. Ghodgaonkar, V. Varadan, and V. Varadan, "Free-space measurement of complex permittivity and complex permeability of magnetic materials at microwave frequencies," *IEEE Transactions on Instrumentation and Measurement*, vol. 39, no. 2, pp. 387–394, Apr. 1990.

[104] D. L. Mensa, "High resolution radar cross-section imaging," *Boston, MA, Artech House, 1991, 280 p.*, 1991.

[105] J. L. Davis and A. Annan, "Ground-penetrating radar for high-resolution mapping of soil and rock stratigraphy 1," *Geophysical prospecting*, vol. 37, no. 5, pp. 531–551, Jul. 1989.

[106] J. C. Bolomey, A. Izadnegahdar, L. Jofre Roca, C. Pichot du Mezeray, and G. Peronnet, "Microwave diffraction tomography for biomedical applications," *IEEE Transactions on Microwave Theory and Techniques*, vol. 30, no. 11, pp. 1998–2000, Nov.

[107] E. Abbe, "Beiträge zur theorie des mikroskops und der mikroskopischen wahrnehmung," *Archiv für mikroskopische Anatomie*, vol. 9, no. 1, pp. 413–418, Dec.

[108] X. Zhang and Z. Liu, "Superlenses to overcome the diffraction limit," *Nature materials*, vol. 7, no. 6, p. 435, Jun. 2008.

[109] P. M. Meaney, K. D. Paulsen, and J. T. Chang, "Near-field microwave imaging of biologically-based materials using a monopole transceiver system," *IEEE Transactions on Microwave Theory and Techniques*, vol. 46, no. 1, pp. 31–45, Jan. 1998.

[110] M. Ostadrahimi, A. Zakaria, J. LoVetri, and L. Shafai, "A near-field dual polarized (te–tm) microwave imaging system," *IEEE Transactions on Microwave Theory and Techniques*, vol. 61, no. 3, pp. 1376–1384, Mar. 2013.

[111] C. Pichot, L. Jofre, G. Peronnet, and J. Bolomey, "Active microwave imaging of inhomogeneous bodies," *IEEE Transactions on Antennas and Propagation*, vol. 33, no. 4, pp. 416–425, Apr. 1985.

[112] M. Born and E. Wolf, *Principles of optics: electromagnetic theory of propagation, interference and diffraction of light*, Jun. 2013.

[113] N. Zaiping, Y. Feng, Z. Yanwen, and Z. Yerong, "Variational born iteration method and its applications to hybrid inversion," *IEEE Transactions on Geoscience and Remote Sensing*, vol. 38, no. 4, pp. 1709–1715, Jul.

[114] M. Rabbani, A. Tavakoli, and M. Dehmollaian, "A hybrid quantitative method for inverse scattering of multiple dielectric objects," *IEEE Transactions on Antennas and Propagation*, vol. 64, no. 3, pp. 977–987, Apr. 2016.

[115] A. Roger, "Newton-kantorovitch algorithm applied to an electromagnetic inverse problem," *IEEE Transactions on Antennas and Propagation*, vol. 29, no. 2, pp. 232–238, Mar.

[116] T. Rubæk, P. M. Meaney, P. Meincke, and K. D. Paulsen, "Nonlinear microwave imaging for breast-cancer screening using gauss–newton's method and the cgls inversion algorithm," *IEEE Transactions on Antennas and Propagation*, vol. 55, no. 8, pp. 2320–2331, Aug.

[117] P. Mojabi and J. LoVetri, "Microwave biomedical imaging using the multiplicative regularized gauss–newton inversion," *IEEE Antennas and Wireless Propagation Letters*, vol. 8, pp. 645–648, Jul.

[118] H. W. Engl, M. Hanke, and A. Neubauer, *Regularization of inverse problems*, Jul., vol. 375.

[119] M. N. Kabir and D. Verschuur, "Restoration of missing offsets by parabolic radon transform," *Geophysical Prospecting*, vol. 43, no. 3, pp. 347–368, Apr. 1995.

[120] A. Franchois, A. Joisel, C. Pichot, and J.-C. Bolomey, "Quantitative microwave imaging with a 2.45-ghz planar microwave camera," *IEEE Transactions on Medical Imaging*, vol. 17, no. 4, pp. 550–561, Aug.

[121] W. Guo and T. Guo, "Three-dimensional dielectric imaging by microwave inverse scattering with resolution unlimited by wavelength," in *Electrical Insulation and Dielectric Phenomena, 1989. Annual Report., Conference on.* IEEE, Oct. 1989, pp. 65–74.

[122] P. M. Meaney, M. W. Fanning, D. Li, S. P. Poplack, and K. D. Paulsen, "A clinical prototype for active microwave imaging of the breast," *IEEE Transactions on Microwave Theory and Techniques*, vol. 48, no. 11, pp. 1841–1853, Nov.

[123] C. W. Barnes, "Object restoration in a diffraction-limited imaging system," *JOSA*, vol. 56, no. 5, pp. 575–578, 1966.

[124] A. Schatzberg and A. J. Devaney, "Super-resolution in diffraction tomography," *Inverse Problems*, vol. 8, no. 1, p. 149, 1992.

[125] X. Li, E. J. Bond, B. D. Van Veen, and S. C. Hagness, "An overview of ultra-wideband microwave imaging via space-time beamforming for early-stage breast-cancer detection," *IEEE Antennas and Propagation Magazine*, vol. 47, no. 1, pp. 19–34, 2005.

[126] S. S. S. MARIA A. STUCHLY, "Coaxial line reflection methods for measuring dielectric properties of biological substances at radio and microwave frequencies-a review," *IEEE Transactions on INSTRUMENTATION AND MEASUREMENT*, vol. 29, no. 3, pp. 176–183, Sep. 1980.

[127] J. Krupka, "Frequency domain complex permittivity measurements at microwave frequencies," *Measurement Science and Technology*, vol. 17, no. 6, p. R55, Apr. 2006.

[128] M. Venkatesh and G. Raghavan, "An overview of dielectric properties measuring techniques," *Canadian Biosystems Engineering*, vol. 47, no. 7, pp. 15–30, Jul. 2005.

[129] Z. Akhter and M. J. Akhtar, "Time domain microwave technique for dielectric imaging of multi-layered media," *Journal of Electromagnetic Waves and Applications*, vol. 29, no. 3, pp. 386–401, Feb. 2015.

[130] J. Baker-Jarvis, R. Geyer, J. Grosvenor, M. Janezic, C. Jones, B. Riddle, C. Weil, and J. Krupka, "Dielectric characterization of low-loss materials a comparison of techniques," *IEEE Transactions on Dielectric and Electrical Insulation*, vol. 5, no. 4, Aug. 1998.

[131] L. Yousefi, H. Attia, and O. M. Ramahi, "Broadband experimental characterization of artificial magnetic materials based on a microstrip line method," *Progress In Electromagnetics Research*, vol. 90, pp. 1–13, 2009.

[132] L. Yousefi, M. S. Boybay, and O. M. Ramahi, "Characterization of metamaterials using a strip line fixture," *IEEE Transactions on Antennas and Propagation*, vol. 59, no. 4, pp. 1245–1253, Apr. 2011.

[133] O. Büyüköztürk, T.-Y. Yu, and J. A. Ortega, "A methodology for determining complex permittivity of construction materials based on transmission-only coher-

ent, wide-bandwidth free-space measurements," *Cement and Concrete Composites*, vol. 28, no. 4, pp. 349–359, 2006.

[134] F. T. Ulaby, E. Michielssen, and U. Ravaioli, *Fundamentals of applied electromagnetics 6e*, 2010.

[135] R. Smith-Bindman, P. Chu, D. L. Miglioretti, C. Quale, R. D. Rosenberg, G. Cutter, B. Geller, P. Bacchetti, E. A. Sickles, and K. Kerlikowske, "Physician predictors of mammographic accuracy," *Journal of the National Cancer Institute*, vol. 97, no. 5, pp. 358–367, 2005.

[136] W. C. Chew and Y.-M. Wang, "Reconstruction of two-dimensional permittivity distribution using the distorted born iterative method," *IEEE transactions on medical imaging*, vol. 9, no. 2, pp. 218–225, 1990.